Deformations and Interactions of (Nano-)Fibers

Dissertation

zur Erlangung des akademischen Grades eines

Doktors der Naturwissenschaften

(Dr. rer. nat.)

an der

Bayreuther Graduiertenschule für Mathematik

und Naturwissenschaften der Universität Bayreuth

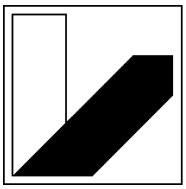

UNIVERSITÄT
BAYREUTH

vorgelegt von

Benedikt Richard Neugirg

geboren in Neustadt an der Waldnaab

September 2016

Die vorliegende Arbeit wurde in der Zeit von Januar 2013 bis September 2016 in Bayreuth am Lehrstuhl Physikalische Chemie II unter Betreuung von Herrn Professor Dr. Andreas Fery angefertigt.

Vollständiger Abdruck der von der Bayreuther Graduiertenschule für Mathematik und Naturwissenschaften (BayNAT) der Universität Bayreuth genehmigten Dissertation zur Erlangung des akademischen Grades eines Doktors der Naturwissenschaften (Dr. rer. nat.).

Dissertation eingereicht am: 23.09.2016
Zulassung durch das Leitungsgremium: 18.10.2016
Wissenschaftliches Kolloquium: 28.04.2017

Amtierender Direktor: Prof. Dr. Stephan Kümmel

Prüfungsausschuss:
Prof. Dr. Andreas Fery (Erstgutachter)
Prof. Dr. Georg Papastavrou (Zweitgutachter)
Prof. Dr. Andreas Greiner (Vorsitz)
Prof. Dr. Josef Breu

Meiner Familie

und

meiner Nicky

Contents

ZUSAMMENFASSUNG XI

SUMMARY XV

LIST OF PUBLICATIONS XIX

I. INTRODUCTION 21

I.1 Motivation 23
Hierarchical Structuring 24
Composite Materials 26

I.2 Objective of the Thesis 27

I.3 References 30

II. STATUS OF THE FIELD 33

II.1 Overview 35

II.2 The Atomic Force Microscope (AFM) – A Tool for Nanoscopic Force Measurements 36
Cantilever Calibration 38
The Force-Distance Curve 40

II.3 Mechanical Testing of (Nano-)Fibers 42
(AFM-based) Tensile Testing 43
AFM-based Three-Point Deformation Testing 45

II.4 Interactions in the Colloidal Domain – The DLVO-Theory 51

II.5 Electrospinning – Shaping Materials into (Nano-)Fibers 56

II.6 Natural and Recombinant Spider Silk 59
Natural Silk 59
Recombinant Silk 61

II.7 Supramolecular Chemistry of 1,3,5-Benzene- and Cyclohexanetricarboxamides 62

II.8 References 66

III. SYNOPSIS 79

III.1 Outline 81

III.2 Tensile versus AFM Testing of Electrospun PVA Nanofibers: Bridging the Gap from Microscale to Nanoscale 81

III.3 Mechanical Testing of Engineered Spider Silk Filaments Provides Insights into Molecular Features on a Mesoscale 84

III.4 Long-Range Interaction Forces between 1,3,5-Cyclohexanetrisamide Fibers in Crossed-Cylinder Geometry 87

III.5 Individual Contributions to Joint Publications 89

IV. PUBLICATIONS 91

IV.1 Tensile versus AFM Testing of Electrospun PVA Nanofibers: Bridging the Gap from Microscale to Nanoscale 93

Abstract 94
Introduction 94
Results and Discussion 96
Conclusion 102
Experimental Section 103
Acknowledgements 105
References 105

IV.2 Mechanical Testing of Engineered Spider Silk Filaments Provides Insights into Molecular Features on a Meso-Scale 109

Abstract 110
Introduction 110
Results and Discussion 110
Conclusion 113
Experimental Section 124
Acknowledgements 126
Supporting Information 127
References 129

IV.3 Long-Range Interaction Forces between 1,3,5-Cyclohexanetrisamide Fibers in Crossed-Cylinder Geometry 133

Abstract 134
Introduction 134
Results and Discussion 136
Conclusion 147

Experimental Section 148
Acknowledgements 150
Supporting Information 151
References 155

PERSPECTIVES 161
References 163

DANKSAGUNG 165

ERKLÄRUNG 167

Zusammenfassung

Mechanisch herausragende, biologische Hochleistungsmaterialien wie Holz, Perlmutt oder Spinnenseide können bedeutend dazu beitragen, die globalen Herausforderungen unserer Zeit zu meistern. Dabei ist ihre jeweils direkte Verwendung als Werkstoff nachrangig. Viel wichtiger ist, dass wir durch sie einen Einblick gewinnen können, nach welchen Konzepten die Natur derartige Materialien aufbaut. Basierend auf einem limitierten Repertoire an (natürlichen) chemischen Bausteinen werden diese Materialien in der Natur bei milden (natürlichen) Prozessbedingungen höchst effizient assembliert und strukturiert. Und trotz dieser (natürlichen) Einschränkungen bleiben sie bezüglich ihres Herstellungsprozesses und vor allem bezüglich ihres Eigenschaftsspektrums für den Menschen mit seinen weitreichenden Fabrikations-Möglichkeiten bis dato tatsächlich „unnachahmlich“. Verantwortlich für die außergewöhnlichen mechanischen Eigenschaften biologischer Hochleistungsmaterialien sind hauptsächlich zwei grundlegende Konzepte: deren hierarchische Strukturierung und ihr Aufbau als Kompositmaterialien (bzw. die Kombination dieser beiden Konzepte).

Beinahe allgegenwärtig findet man beides auf der Basis (nano-)fibrillärer Grundbausteine verwirklicht. Voraussetzung für ein anwendungsrelevantes Verständnis biologischer Hochleistungsmaterialien ist zunächst ein umfassendes Verständnis dieser Grundbausteine. So ist die Entwicklung von Methoden zur umfassenden Charakterisierung von (Nano-)fasern, sowohl mechanisch als auch in Bezug auf deren Wechselwirkungen, das übergeordnete Ziel dieser Arbeit.

Derartige Untersuchungen einzelner Fasern mit mikro- oder nanoskopischem Durchmesser stellen besondere Ansprüche an die Messmethode. Die Rasterkraftmikroskopie (atomic force microscopy, AFM) bildet eine attraktive Möglichkeit über die reine Visualisierung hinaus diesen Ansprüchen gerecht zu werden und die mechanischen Eigenschaften solcher Fasern sensitiv zu untersuchen oder sogar ihre Wechselwirkungen untereinander oder mit anderen Objekten direkt zu messen.

Die mechanischen Untersuchungen in dieser Arbeit wurden mittels AFM-basierter mikroskopischer Dreipunkt-Deformationsversuche durchgeführt. Hierbei werden die betreffenden Fasern zunächst auf einem Glassubstrat, das mit Mikrokanälen vorstrukturiert ist, abgelegt. Die über den Kanälen freistehenden Fasersegmente können mittels eines AFM Cantilevers senkrecht zur Faserachse kontrolliert deformiert werden. Aus den resultierenden Kraft-Deformationskurven lassen sich die mechanischen Eigenschaften der Fasern ableiten. Diese Methode erlaubt es, (Nano-)fasern entlang konsekutiver, kurzer Segmente reversibel und irreversibel (bis zum Bruch) bei kontrollierten Umgebungsbedingungen mechanisch zu charakterisieren.

Elastische, vertikale Deformationen ausgeübt mit spitzenlosen AFM Cantilevern und hoher Kraftauflösung geben beispielsweise zuverlässige Werte für den E-Modul solcher Nanofasern. Dies wird dann besonders deutlich, wenn identisch hergestellte, elektrogesponnene Nanofasern aus Polyvinylalkohol sowohl mit dieser AFM-basierten Methode, als auch mit dem komplementären – da uniaxialen – Zug-Dehnungsversuch getestet werden (***Kapitel III.2***). Letzterer ist die Standardmethode für die mechanische Charakterisierung makroskopischer Fasern und die Dateninterpretation dementsprechend etabliert, steht aber in Bezug auf Nanofasern der AFM-basierten Methode in Kraftauflösung und Probenanforderungen (Mindestlänge und –durchmesser der Fasern) nach. Die erstmalige Verifizierung der Konformität beider Methoden ist Grundlage für die Vergleichbarkeit von Faserstudien. Darüber hinaus gibt diese Studie Einblicke in die molekulare Struktur elektrogesponnener Nanofasern. Wie mit beiden mechanischen Testmethoden unabhängig zu beobachten ist, steigt der E-Modul mit sinkendem Faserdurchmesser signifikant an. Dies ist auf die hohen Scherraten beim Elektrospinning zurückzuführen, welche die Molekülketten an der Faseroberfläche verstrecken und entlang der Faserachse ausrichten. Dieser Effekt dominiert den E-Modul umso stärker je größer das Oberfläche-zu-Volumen-Verhältnis, also je kleiner der Faserdurchmesser wird.

Bei Nanofasern aus (rekombinanten) Spinnenseiden ist vor allem das Bruchverhalten, also die Bruchdehnung und die Zähigkeit, von Interesse. Diese Größen sind über eine Abwandlung der vorangegangenen Dreipunkt-Deformationsversuche zugänglich: die Verwendung eines Cantilevers mit Spitze ermöglicht nunmehr die laterale Deformation eines freistehenden Fasersegments welche instrumentell bedingt größere Faserdeformationen erlaubt. In der Studie in ***Kapitel III.3*** wurde so das gesamte mechanische Spektrum rekombinanter, elekrogesponnener Spinnenseidenproteine untersucht wobei einzelne Einflussparameter isoliert beobachtet werden konnten: das

Elektrospinning bzw. die Fasernachbehandlung im Alkohol-Dampf erlauben es den Anteil von β-Faltblattstrukturen in den Fasern einzustellen. Im Zusammenspiel mit dem Luftfeuchtigkeitsgehalt der Umgebung zeigt sich so, dass nur Fasern mit hohem Quervernetzungsgrad durch β-Faltblätter und hohem Wassergehalt die Zähigkeit natürlicher Spinnenseide erreichen.

Um Wechselwirkungen von Fasern zu detektieren, kann die sogenannte „Colloidal Probe“ Methode, bei der kolloidale Partikel an spitzenlose AFM Cantilever geheftet werden, abgewandelt werden. Das Anbringen eines einzelnen Fasersegments an einen spitzenlosen Cantilever mittels Mikromanipulation ermöglicht ein anschließendes Annähern und Entfernen dieser Faser an eine zweite Faser und zeigt so deren Wechselwirkungen in ihrer Kraft-Abstandskorrelation. 1,3,5-Cyclohexantrisamide (CTAs) eignen sich modellhaft für solche Versuche, da sie zum einen mit verschiedenen peripheren Gruppen (hier Alkyl bzw. perfluoriert) synthetisiert werden können und somit Kontrolle über die Oberflächenchemie bieten. Zum anderen bilden CTAs Supramoleküle aus und können aufgrund ihrer großen intermolekularen Kohäsion zu Fasern schmelz-elektrogesponnen. Diese Fasern sind mit glatten Oberflächen und Durchmessern um etwa 5 µm ideal für Faser-Faser-Wechselwirkungsmessungen. Um Kapillarkräfte zu vermeiden, wurden solche Faser-Faser-Experimente in wässrigen Salzlösungen kontrollierter Ionenstärke durchgeführt und konnten dann gemäß der DLVO-Theorie interpretiert werden (***Kapitel III.4***). Als Ergebnis erhält man bei symmetrischen Versuchen (beide Fasern bestehen aus dem gleichen Material) die effektive Oberflächenladungsdichte, welche wie bei flachen Filmen für das alkylierte System aufgrund asymmetrischer Adsorption von Hydroxidionen größer ist als bei dem perfluorierten System. Auf dieser Basis können Wechselwirkungen von Fasern untereinander sowie weiterführend von Fasern mit Umgebungspartikeln interpretiert werden. Diese Kenntnisse ermöglichen ein prinzipielles Verständnis etwa von Filtrationsprozessen.

Zusammenfassend wurden in dieser Arbeit AFM-basierte, generische Herangehensweisen weiterentwickelt, welche es erlauben, (Nano-)Fasern umfangreich zu charakterisieren. Diese methodischen Grundlagen wurden beispielhaft auf Vertreter eines breiten Materialspektrums (Polymer, Protein, Surpramoleküle) angewendet und vertiefen dabei das Verständnis des Faserspinnprozesses beim Elektrospinnen, rekombinanter Spinnenseidenproteine bei unterschiedlichen Umwelteinflüssen sowie von niedermolekularen Supramolekülen.

Summary

Wood, nacre and spider silk are examples for mechanically exceptional biological high-performance materials. These materials are most valuable because they provide insights into nature's principal concepts of material design and, therefore, might play a significant role in facing the global challenges of our time. It is amazing, how nature starts out from a very limited (the natural) repertoire of chemical compounds and assembles/structures these materials at benign (natural) conditions at highest efficiency to grow these outstanding materials. Despite the limitations involved in the natural process and modern industry overcoming all of those limitations separately, biological high-performance materials still cannot be recreated artificially. Intense research on structural biomaterials revealed two principal concepts, which are held liable for the exceptional mechanical properties: hierarchical structuring over several length scales and the use of composite materials (and the combination of both concepts, respectively).

Both concepts can be found for many examples throughout nature and very often (nano-)fibers form the basic building unit on the lowest hierarchical level. Transferring these concepts to synthetic materials first requires full comprehension of the natural process, starting from the basic structural component, i.e. the (nano-)fiber. This thesis contributes to that understanding by further developing methods to fully characterize (nano-)fibers in terms of their mechanical behavior as well as with regard to their interactions.

Investigations of individual fibers with micro- or nanoscopic diameters impose special requirements on the measurement technique. Atomic force microscopy (AFM) is an attractive platform to go beyond fiber imaging and sensitively deform such fibers mechanically or even directly measure their interactions among each other or with further objects.

In this thesis, mechanical characterization of nanofibers is accomplished by AFM-based microscopic three-point deformation testing. This method involves depositing fiber specimen on a glass

substrate, which is pre-structured with microchannels. Fiber segments that are suspended over the microchannels (i.e. free-standing segments) are accessible for controlled deformations perpendicular to their long axis by an AFM cantilever. The resulting force-deformation curves allow to derive the mechanical properties of the fibers. This approach facilitates mechanical characterization of consecutive short segments along a single (nano-)fiber. It is receptive for testing reversibly or irreversibly (until rupture) and at controlled environmental conditions.

The Young's modulus of nanofibers, for instance, can be determined very precisely using a tipless AFM cantilever and applying small, elastic deformations. The standard method for mechanical testing of macroscopic fibers is the uniaxial tensile tester, which benefits from the simple setup and straightforward data evaluation. However, when testing nanofibers, tensile testing suffers from inherent specimen limitations and the coarse force resolution. To ensure comparability of mechanical fiber studies based on either of the two methods (tensile testing or AFM three-point deformation), identically prepared, electrospun polyvinyl alcohol nanofibers have been tested using both approaches (***chapter III.2***). The elucidated conformity and the mutual validation of methods is a crucial step for advanced nanofiber design. Furthermore, this study provides insights into the molecular structure of electrospun nanofibers. Both testing methods independently agree on significantly increasing Young's moduli when fiber diameters decrease. This can be explained by the extraordinary shear rates during electrospinning, which stretch and align the polymer chains close to the fiber surface. This effect dominates the Young's modulus more and more as the fiber diameter decreases because the surface-to-volume ratio increases accordingly.

The special interest in spider dragline silk arises from its outstanding rupture properties, e.g. extensibility and toughness. Those parameters can be determined for nanofibers as well, when the aforementioned AFM-based three-point deformation testing is modified: using a cantilever with a sharp tip allows for lateral deformations of the free-standing fiber segment and hence, instrumentally, for larger deformations. In ***chapter III.3***, this approach was employed to determine the complete mechanical spectrum of electrospun, recombinant spider silk protein nanofibers while explicitly investigating the influence of β-sheet content in the protein and environmental humidity. As the main result, it became evident that spider silk can only reach the natural thread's toughness at high physical cross-linking (high β-sheet content) and high hydration.

The "colloidal probe technique" utilizes colloidal particles attached to tipless AFM cantilevers to directly determine their interaction with other surfaces. This technique can be modified with regard

to fiber-fiber interactions when a fiber segment is immobilized at the cantilever and approached to or retracted from a second fiber in crossed-cylinder geometry. An exemplary system for such measurements are 1,3,5-cyclohexanetrisamides (CTAs), which are studied in ***chapter III.4***. CTAs can be synthesized with different peripheral groups (alkyl and perfluorinated in this work), which largely allows to control the respective surface chemistry. Furthermore, these molecules exhibit strong cohesion forces making them capable of supramolecular self-assembly. The strong cohesion also facilitates CTAs to be melt-electrospun to smooth fibers of diameters around 5 µm. To avoid capillary forces, the AFM-based fiber-fiber interaction measurements have been conducted in aqueous salt solutions of controlled ionic strength and for symmetric systems, i.e. both fibers are made of the same material, respectively. Evaluation according to the DLVO theory yields an effective surface charge density, which is higher for the alkyl system compared to the perfluorinated one. This result is in accordance with studies on self-assembled monolayer films with similar terminating groups and can be attributed to the asymmetric adsorption of hydroxide ions from the aqueous solution. The surface properties of such fibers are the basis to understand fiber interactions and also the interactions of fibers with other particles, e.g. as relevant for filtration.

In summary, this thesis demonstrates generic AFM-based approaches to comprehensively characterize (nano-)fibers. The methodical principles have been exemplarily shown with respect to a broad material spectrum (polymer, protein, supramolecule). The individual studies provide insights into the fiber formation process in electrospinng, the molecular picture of spider silk mechanics at different environmental conditions and low molecular weight supramolecules.

List of Publications

[1] “Top-Down Meets Bottom-Up: A Comparison of the Mechanical Properties of Melt Electrospun and Self-Assembled 1,3,5-Benzenetrisamide Fibers”, D. Kluge, J.C. Singer, B.R. Neugirg, J.W. Neubauer, H.-W. Schmidt, A. Fery, *Polymer*, **2012**, *53* (25), 5754-5759

[2] “Long-Range Interaction Forces Between 1,3,5-Cyclohexanetrisamide Fibers in Crossed-Cylinder Geometry”, B.R. Neugirg, N. Helfricht, S. Czich, H.-W. Schmidt, G. Papastavrou, A. Fery, *Polymer*, **2016**, *102*, 363-371

[3] “AFM-Based Mechanical Characterization of Single Nanofibres”, B.R. Neugirg, S.R. Koebley, H.C. Schniepp, A. Fery, *Nanoscale*, **2016**, *8* (16), 8414-8426

[4] “Tensile versus AFM Testing of Electrospun PVA Nanofibers: Bridging the Gap from Microscale to Nanoscale”, B.R. Neugirg, M. Burgard, A. Greiner, A. Fery, *Journal of Polymer Science Part B: Polymer Physics*, **2016**, *54* (23), 2418-2424

[5] “Mechanical Testing of Engineered Spider Silk Filaments Provides Insights into Molecular Features on a Mesoscale”, G. Lang, B.R. Neugirg, D. Kluge, A. Fery, T. Scheibel, *ACS Applied Materials and Interfaces,* **2017**, *9* (1), 892-900

This thesis is based on the publications [2], [4] and [5], which are adapted as chapters III.4, III.2, and III.3, respectively. The review article [3] was adapted and partially included in chapter II.3.

I. Introduction

“Das Schicksal ist zu ernst,
als dass man es dem
Zufall überlassen kann”

Sir Peter Ustinov

I.1 Motivation

Only the hierarchical structuring of composite materials renders the outstanding properties of nature's high-performance materials possible. This thesis contributes to the fundamental understanding of (nano-)fibers, a ubiquitous building block in such materials.

Nature's high-performance biomaterials have fascinated mankind for thousands of years – from ancient cavemen to modern material scientists. Cavemen showed their fascination mostly in a practical manner by the extensive use of e.g. wood and bone in their everyday life. Those two materials, for instance, combine high toughness and low weight making them appealing for all kinds of practical applications. Today's material scientists in contrast are primarily trying to understand the principles rendering these properties possible – and always aim at eventually designing similar materials themselves.[1] Especially structural biological materials as wood[2, 3] and bone,[3-6] but also nacre,[4, 5, 7] teeth,[8, 9] bamboo,[4, 5, 10] or spider silk[11-13] amaze not only because of their superior mechanical properties (e.g. bamboo's strength or the silk's outstandingly high toughness each at relatively low density). Those materials also amaze due to their formation process: they all emerge from a very limited set of chemical compounds (e.g. biopolymers, some minerals and ions) that are assembled at ambient temperatures and pressures[3-5] and, of course, will finally undergo complete biodegradation. In the light of these critical limitations imposed on the formation process, the following questions arise: how can organisms grow biomaterials that compete with or even outperform modern synthetic materials despite their comparatively small construction kit to start with? How can trees, for instance, grow to such large and robust structures, how can spiders spin such strong yet extensible threads, both using nothing but sugars or amino acids and water at benign process conditions? And ultimately, how can we imitate such systems?

The answer is "simple": complex ***hierarchical structuring*** of ***composite materials***.[3, 4, 14]

Hierarchical Structuring

The concept and benefits of hierarchical structuring can be illustrated best when examining two very different yet related examples: the man-made Eiffel Tower and naturally grown bamboo culms (Figure 1).*

In 1889, the Eiffel Tower surpassed the Washington Monument (an unstructured obelisk) as the tallest man-made structure in the world almost doubling this former height record.[15] The Eiffel Tower's height of 324 m was made possible by the approach of hierarchical engineering, i.e. the tower is precisely structured in ever smaller building components over almost 7 decimal powers (Figure 1, yellow parts). The tower's four main pillars (that fuse at the top) each consist of a multitude of crossbars that in turn are made from individual struts. These struts are clenched by rivets, which finally were manufactured at sub-mm accuracy.[16] This principle has made the Eiffel Tower mechanically and aesthetically extremely successful as evidenced by the record-setting height and the vast number of visitors every day. Additionally, this principle facilitated the construction of the tower within only approximately 26 months. Of course, the tower owes its final stability not only to its engineered structure but also to the use of robust puddle iron for all the building components. Iron is stiff and strong and therefore it was the material of choice in such a project. However, its robustness comes at the price of high density. This determines a total weight of 7 300 tons for the Eiffel Tower's metal structure.[15] Yet, this may seem heavy only at first glance. Due to the macroscopic structuring, the tower's overall relative density is as small as approximately one per mille as compared to bulk iron.[16] So, the radical new design has made the tower comparatively light-weight, stable, and high. But still, there is plenty of room at the bottom[17] to further exploit the principles of hierarchical structuring.

The consequent continuation of the Eiffel Tower's macroscopic design principles on the meso- and nanoscale can be found in many biological high-performance materials. Nature's "architects" master the task of multiscale hierarchical structuring and hence fuel human interest in understanding such biomaterials. One example is bamboo (Figure 1, blue parts), which combines high strength with low density. On the macroscopic scale, a bamboo's stem (or culm) can be divided into the denser nodes and the hollow internode section. The culm's wall in the internode section is an axially oriented fiber

* Additionally, in chapter II.6, the hierarchical structure of spider silk threads will be discussed as a further example of the concept.

composite with a surrounding foam-like matrix.[10] This composite gradually densifies with distance from the culm's center. Therefore, the culm also becomes stiffer and stronger from inside to the outside. Finally, at the lowest level of hierarchy, the cells forming the composite themselves are a lamellar fiber composite of cellulose microfibrils embedded in lignin and hemicellulose, similar to wood.[3, 10] With continuous structuring throughout almost 12 orders (!) of magnitude in length, bamboo is highly optimized for its environmental needs within its given natural limitations (i.e. growth at benign temperature and pressure, limitation of chemical compounds available).

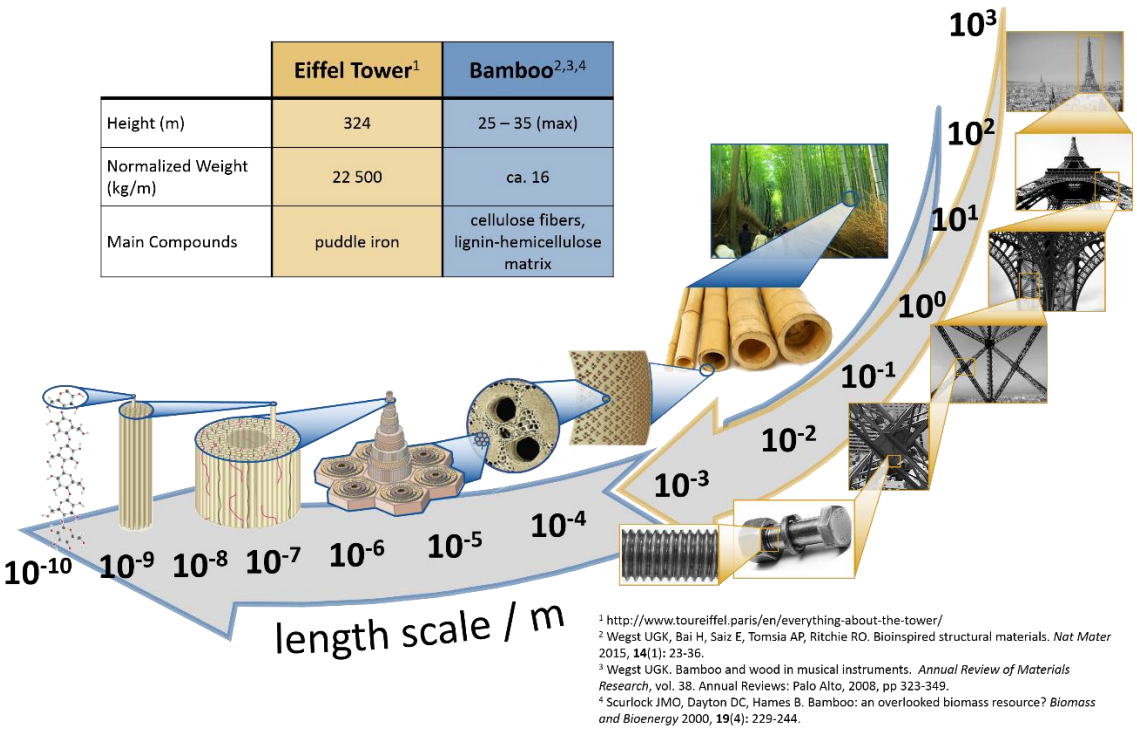

Figure 1| The Eiffel tower is a masterpiece of human engineering and hierarchically structured over almost 7 orders of magnitude in length – from its total height down to the sub-mm scale.* Many of nature's materials, for instance bamboo, are further structured on the meso- and down to the nanoscale giving rise to their outstanding (mechanical) properties at simultaneous low weight.†

* Iron's crystal structure is not considered as it is arguably not intentionally arranged by the manufacturer.
† Individual images are taken from: (access date 23.08.2016 for all)
http://www.budgettraveltalk.com/2015/03/19/budget-arashiyama-bamboo-forest/
http://bamboohabitat.com/bamboo-poles/
http://cheapvacationholiday.com/eiffel-tower/#prettyPhoto[gallery]/2/
http://www.thousandwonders.net/Eiffel+Tower
http://b.saaraa.com/?p=73
http://weheartit.com/entry/group/39989215

When comparing the structures of both, the Eiffel Tower and bamboo, one can find predominantly high-aspect ratio structural building components on several hierarchical levels. Similar to the tower's pillars, crossbars, struts, and rivets, bamboo exhibits aligned macroscopic fibers that consist of ever smaller fibrils. These almost one-dimensional components are mostly oriented to face stresses along their axis. Furthermore, placing building components only where load-bearing is necessary allows for omitting large amounts of material, which in turn reduces the overall weight. This is one reason, why one-dimensional objects are found in many man-made structures and throughout nature's materials. Notably, the Eiffel Tower's iron struts are also designed for bending rigidity while bamboo's fibers can be easily bent perpendicular to their long axis. Therefore, bamboo attains its flexibility and adjusts its resistance to bending by the density variation in the wall of the culm.

Composite Materials

Apart from hierarchical structuring, the second fundamental concept found in nature's high-performance materials is the combination of two (mechanically) dissimilar materials in a composite. Virtually every biomaterial is a composite of some kind.[5] This is the case for bamboo within each hierarchical level (fiber reinforced matrices) and even more apparent for mineralized materials such as bone or nacre. In the latter, calcium carbonate platelets are glued together by a protein matrix in a brick and mortar structure.[4, 5, 7] The specific deformation mechanisms that facilitate e.g. high toughness and fracture resistance are as diverse as the materials themselves. Yet, the basic components in those composites or the principle, respectively, are conserved throughout the materials: stiffer reinforcements are surrounded by a softer matrix at perfectly matched interphases. Together, the components in such systems synergize to yield a toughness far beyond the ones of the individual components.[4]

This concept can also be found in human engineering already, however not in the Eiffel Tower. Instead, examples are fiber reinforced concrete and polymers[18] or carbon nanotube composite materials.[19] Still there is much to learn from nature, especially with respect to interfacial design and

---

http://www.uncommongoods.com/product/eiffel-tower-bolt-puzzle
http://www.befestigungsfuchs.de/blog/die-wichtigsten-gewindearten-im-ueberblick/

the buildup of gradient materials. Only composites with interfaces designed for sufficient interaction can yield synergistic mechanical effects.[8, 20]

Focusing on nature's prototype biomaterials, it is noticeable that basic building blocks almost always have at least one dimension in the nanoscale (e.g. nanofibers or nanoplatelets). There seem to be two dominating reasons for that:

(1) Small objects maximize internal interfaces. The interface in a biological composite must be considered an integral part of the material just as the matrix or the reinforcement filler themselves. If matched poorly, interfaces will weaken the material as stresses concentrate and eventually cracks form right there. However, if matched well, these interfaces can serve to trap or deflect cracks (especially interfaces between components with different Young's moduli), which yields enhanced material properties.[8, 21-23] Consequently, a maximized internal interfacial area is desired and can be achieved by maximizing the aspect ratio of the filler component, i.e. by decreasing at least one dimension to the nanoscale.

(2) Nanoscale objects have properties different from bulk. Single sheets of graphene[24] or individual metal nanowires[25] are examples that show certain mechanical properties (Young's modulus, strength) substantially surpassing the respective properties of the bulk material. The vastly increased surface-to-volume ratio and the decreased probability for defects are held liable for these observations.[20] This trend of beneficial mechanical properties of nanoscale morphologies holds for many examples (graphene and carbon nanotubes, nanowires, electrospun nanofibers and others). The consequence again is to incorporate preferably these nanoscale components as fillers in a composite, as demonstrated by nature.

I.2 Objective of the Thesis

One key objective in material science in general is to achieve a fundamental understanding of nature's principle to use ***hierarchical structures*** and ***composite materials***. Eventually, human engineers are by far less limited than organisms, e.g. bamboo plants, in terms of material choice or processing parameters. So, if we fully comprehend nature's design principles and the physical

phenomena involved in nature's nano- and mesoscale structuring, we might be able to rationalize visionary new materials that might aid to face the global challenges of our time. To achieve a thorough understanding of any hierarchical or composite material, first, an understanding of the principal building component is indispensable. Ubiquitous building components in many natural materials are nanofibers, which are found for instance as the cellulose fibers in wood or bamboo, as the mineralized collagen fibrils in bone, or the silk filaments in the spider's dragline thread. The focus of this work is to contribute to that fundamental understanding of hierarchically structured materials by elucidating deformations and interactions of (nano-)fibers based on direct force measurements using the atomic force microscope (AFM).

This thesis emphasizes the ***methodical development*** of the AFM as a tool to comprehensively characterize fibrillar systems (the "fertile ground" in Figure 2). Based on this ground, the thesis contributes to an advanced understanding of the most important cornerstones when dealing with fibrillar systems: fiber structure and formation, fiber mechanics, and fiber surface properties. Exemplary for those points, the ***electrospinning*** process, structural transitions in single ***spider silk*** nanofilaments and surface phenomena of supramolecular ***1,3,5-cyclohexanetrisamide*** microfibers (the "flowers" in Figure 2) are investigated in further detail.

Methodical Development. The AFM is still predominantly used as an imaging tool for surface topographies at nanoscopic resolution. Yet, it has also evolved employing its force sensing capabilities to directly probe a multitude of interaction forces in a wide variety of systems. With respect to fibrillar systems, one essential aspect is the mechanical behavior of individual (nano-)fibers, which can conveniently and reproducibly be studied by sophisticated AFM approaches. One goal of this thesis is to demonstrate AFM-based three-point deformation tests as a reliable method to mechanically characterize single fibers. Free-standing fiber segments can be loaded vertically or laterally to precisely determine elastic and/or rupture properties. The three-point procedure is benchmarked here against single fiber tensile testing and the conformity of both methods is verified.

Beyond fiber mechanics, especially fiber surface properties dominate the interactions of fibers among each other as well as of fibers with their respective surrounding – key properties in e.g. composite materials but also in filtration applications. Accessing these properties is almost exclusively possible by an advancement of the well-known colloidal probe technique in AFM. In this

thesis, fiber segments have been immobilized on tipless AFM cantilevers and their interactions with other fibers have been measured directly.

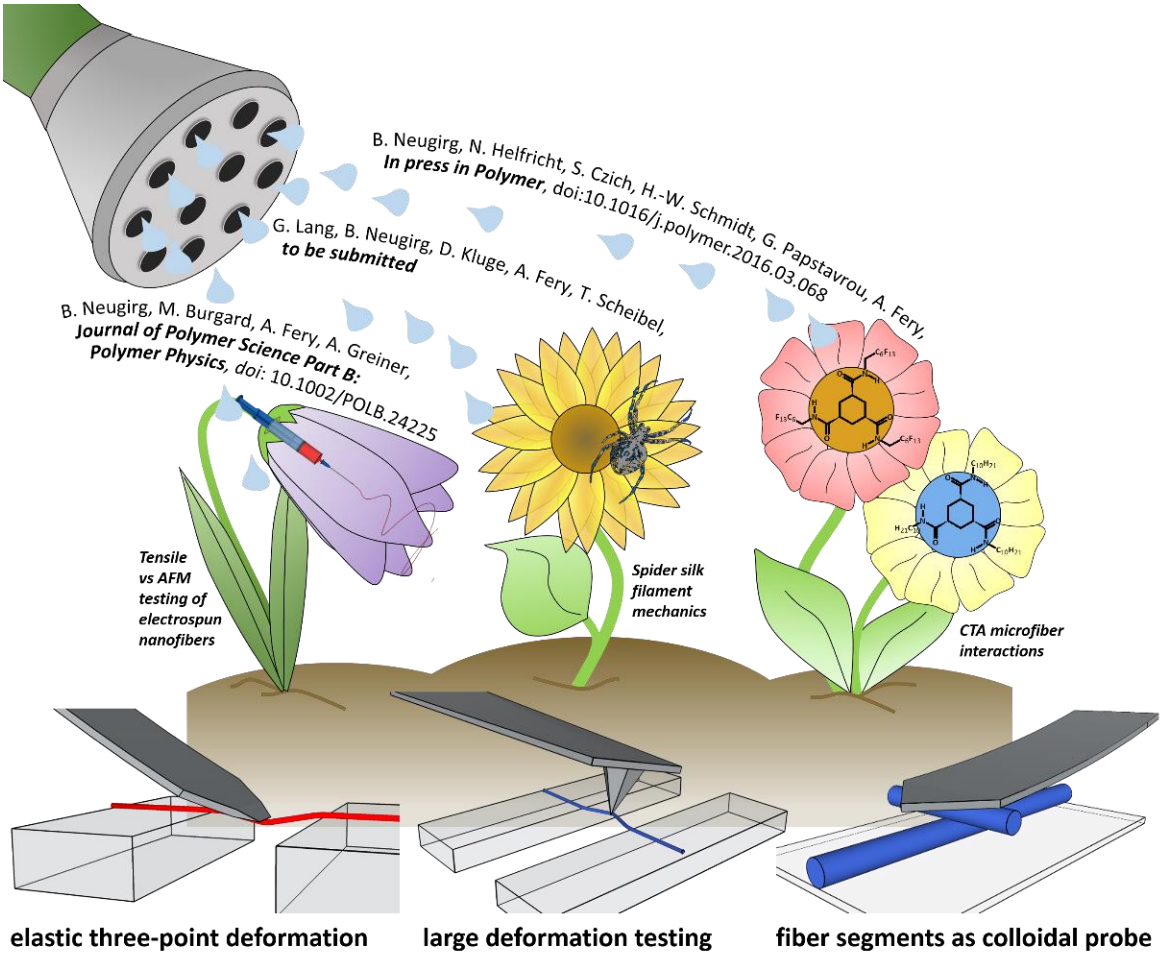

Figure 2| Pictorial overview over the objectives of this thesis. Advanced AFM-based techniques fertilize the ground for a fundamental understanding of fibrillar systems. This understanding distinctly flourishes for fiber formation by electrospinning, for recombinant spider silk and inferences for the natural blueprint, and for the self-assembling 1,3,5-cyclohexanetrisamides with different peripheral groups.

Electrospinning. Electrospinning is capable of shaping a multitude of materials (here: polyvinyl alcohol) to micro- and nanofibers. Thereby, it strongly influences the molecular conformation of the respective material as it tends to stretch and align e.g. polymer chains on the fiber surface. This effect is directly reflected in the fiber stiffness as studied here by AFM single fiber three-point testing. Furthermore, the huge velocity of the spinning process influences crystallization within the

fibers as demonstrated using spider silk as an example. Again, this is studied here mechanically on the single fiber level.

Spider Silk. The single silk protein fiber measurements presented in this thesis allow for the first time to investigate the mesoscale properties of dragline silk threads. The strongly pronounced influence of crystal content and hydration from environmental humidity has a marked influence on the nanofilaments' extensibility and therefore also on their toughness.

1,3,5-cyclohexanetrisamides (CTAs). The strong supramolecular cohesion of this molecular class facilitates to shape them into smooth, homogeneous fibers via melt-electrospinning. AFM-based direct fiber-fiber interaction measurements elucidate the distinct behavior of alkyl-terminated and perfluorinated CTA fibers in aqueous solutions. This way, asymmetric adsorption of hydroxide ions to the fibers surface can be identified as predominant process of surface charging.

In summary, this work demonstrates the ***methodical development*** of sophisticated AFM approaches that enable a comprehensive view on fibrillar systems. All of the approaches presented here are generic and applicable to almost any fiber material. This versatility is illustrated by the medley of elastic deformations of electrospun classical polymer fibers, rupture properties of bioinspired protein fibers, or fiber interactions of fibers from small organic molecules.

I.3 References

1. Aizenberg J, Fratzl P. Biological and Biomimetic Materials. *Adv Mater* 2009, **21**(4)**:** 387-388.

2. Keckes J, Burgert I, Fruhmann K, Muller M, Kolln K, Hamilton M*, et al.* Cell-wall recovery after irreversible deformation of wood. *Nat Mater* 2003, **2**(12)**:** 810-814.

3. Fratzl P, Weinkamer R. Nature's hierarchical materials. *Prog Mater Sci* 2007, **52**(8)**:** 1263-1334.

4. Wegst UGK, Bai H, Saiz E, Tomsia AP, Ritchie RO. Bioinspired structural materials. *Nat Mater* 2015, **14**(1)**:** 23-36.

5. Dunlop JWC, Fratzl P. Biological Composites. In: Clarke DR, Ruhle M, Zok F (eds). *Annual Review of Materials Research*, vol. 40, 2010, pp 1-24.

6. Weiner S, Wagner HD. The material bone: Structure mechanical function relations. *Annu Rev of Mater Sci* 1998, **28:** 271-298.

7. Espinosa HD, Rim JE, Barthelat F, Buehler MJ. Merger of structure and material in nacre and bone - Perspectives on de novo biomimetic materials. *Prog Mater Sci* 2009, **54**(8)**:** 1059-1100.

8. Dunlop JWC, Weinkamer R, Fratzl P. Artful interfaces within biological materials. *Mater Today* 2011, **14**(3)**:** 70-78.

9. Zaslansky P, Friesem AA, Weiner S. Structure and mechanical properties of the soft zone separating bulk dentin and enamel in crowns of human teeth: Insight into tooth function. *J Struct Biol* 2006, **153**(2)**:** 188-199.

10. Wegst UGK. Bamboo and wood in musical instruments. *Annual Review of Materials Research*, vol. 38. Annual Reviews: Palo Alto, 2008, pp 323-349.

11. Gosline JM, Guerette PA, Ortlepp CS, Savage KN. The mechanical design of spider silks: From fibroin sequence to mechanical function. *J Exp Biol* 1999, **202**(23)**:** 3295-3303.

12. Heidebrecht A, Scheibel T. Recombinant Production of Spider Silk Proteins. In: Sariaslani S, Gadd GM (eds). *Advances in Applied Microbiology*, vol. 82. Elsevier Academic Press Inc: San Diego, 2013, pp 115-153.

13. Humenik M, Scheibel T, Smith A. Spider Silk: Understanding the Structure–Function Relationship of a Natural Fiber. In: Stefan H (ed). *Progress in Molecular Biology and Translational Science*, vol. 103. Academic Press, 2011, pp 131-185.

14. Buehler MJ. Tu(r)ning weakness to strength. *Nano Today* 2010, **5**(5)**:** 379-383.

15. All you need to know about the Eiffel Tower. 2016 [cited June 2016]Available from: http://www.toureiffel.paris/images/PDF/all_you_need_to_know_about_the_eiffel_tower.pdf

16. Lakes R. Materials with structural hierarchy. *Nature* 1993, **361**(6412)**:** 511-515.

17. Feynman RP. There's Plenty of Room at the Bottom. *Engineering and Science* 1960, **23**(5)**:** 22-36.

18. Zucchelli A, Focarete ML, Gualandi C, Ramakrishna S. Electrospun nanofibers for enhancing structural performance of composite materials. *Polym Advan Technol* 2011, **22**(3)**:** 339-349.

19. De Volder MFL, Tawfick SH, Baughman RH, Hart AJ. Carbon Nanotubes: Present and Future Commercial Applications. *Science* 2013, **339**(6119)**:** 535-539.

20. Gao H, Ji B, Jäger IL, Arzt E, Fratzl P. Materials become insensitive to flaws at nanoscale: Lessons from nature. *P Natl Acad Sci* 2003, **100**(10)**:** 5597-5600.

21. Clegg WJ, Kendall K, Alford NM, Button TW, Birchall JD. A simple way to make tough ceramics. *Nature* 1990, **347**(6292)**:** 455-457.

22. Fratzl P, Gupta HS, Fischer FD, Kolednik O. Hindered Crack Propagation in Materials with Periodically Varying Young's Modulus—Lessons from Biological Materials. *Adv Mater* 2007, **19**(18)**:** 2657-2661.

23. Smith BL, Schaffer TE, Viani M, Thompson JB, Frederick NA, Kindt J*, et al.* Molecular mechanistic origin of the toughness of natural adhesives, fibres and composites. *Nature* 1999, **399**(6738)**:** 761-763.

24. Lee C, Wei XD, Kysar JW, Hone J. Measurement of the elastic properties and intrinsic strength of monolayer graphene. *Science* 2008, **321**(5887)**:** 385-388.

25. Wu B, Heidelberg A, Boland JJ. Mechanical properties of ultrahigh-strength gold nanowires. *Nat Mater* 2005, **4**(7)**:** 525-529.

II. Status of the Field

“Es ist schon alles gesagt,
nur noch nicht von allen”

Karl Valentin

II.1 Overview

As indicated in the previous chapter, this thesis aims at a deeper understanding of (nano-)fibers, as they are omnipresent structural building components in natural high-performance materials. To face this task on a single fiber level, the development of AFM-based approaches specialized to investigate such fibrillar systems represents the methodical basis (Figure 3). The bedrock is the AFM (introduced in chapter II.2), which enables direct measurements of single fiber deformations (chapter II.3) and their (colloidal) interactions (chapter II.4).

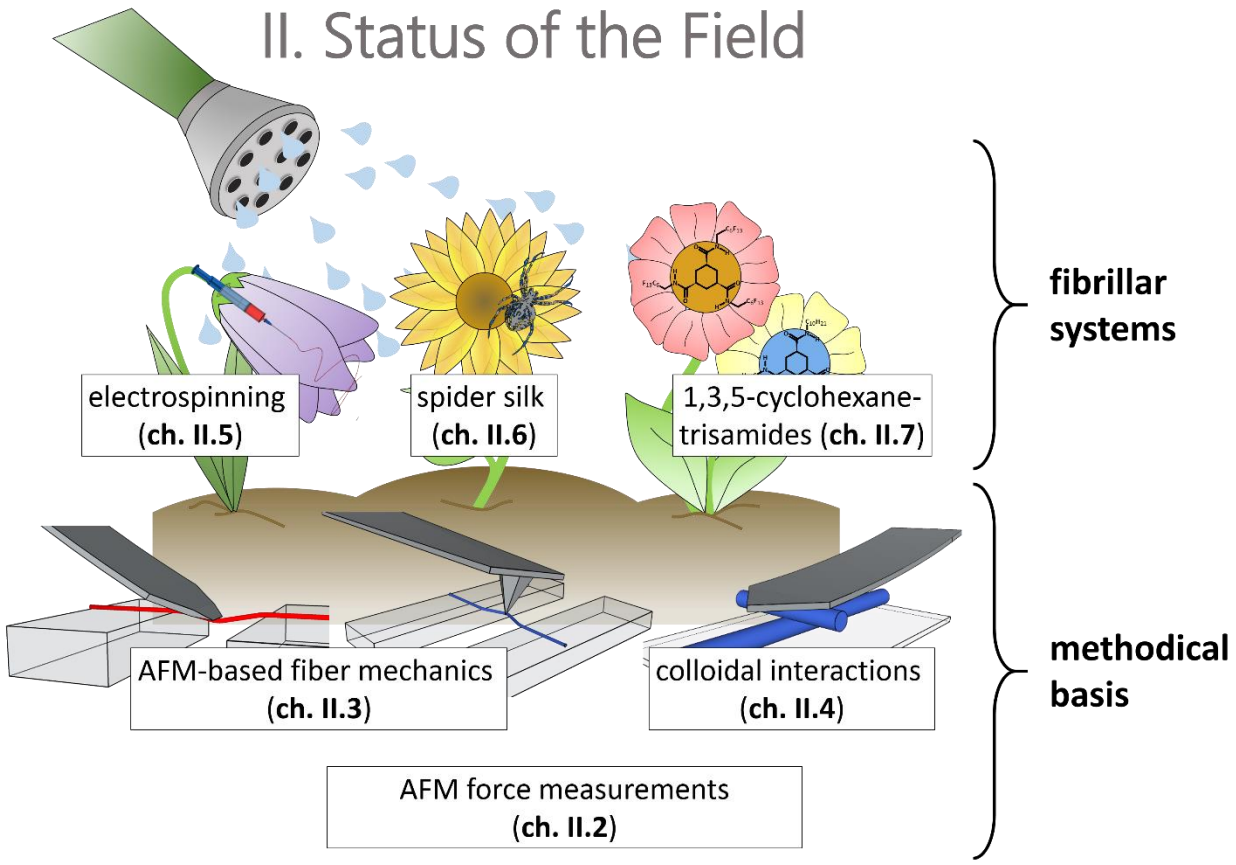

Figure 3| Schematic outline of part II. Status of the Field. The methodical basis is centered around the atomic force microscope (AFM) (chapter II.2), which facilitates the direct measurement of fiber mechanics (chapter II.3) and colloidal interactions (chapter II.4). The specific fibrillar systems investigated on that basis are electrospun PVA (chapter II.5), natural and recombinant spider silk (chapter II.6) and 1,3,5-cyclohexanetrisamides (chapter II.7).

Once this basis is developed, it directly facilitates the "growth" of knowledge about almost every fibrillar system. In the present case, these systems were all prepared by electrospinning (chapter II.5) and cover classical polymers, biomimetic spider silk proteins and melt-electrospun 1,3,5-cyclohexanetriamides. An introduction to natural and recombinant spider silk is given in chapter II.6, supramolecular principles are illustrated using the examples of 1,3,5-benzene- and cyclohexanetrisamides in chapter II.7.

II.2 The Atomic Force Microscope (AFM) – A Tool for Nanoscopic Force Measurements*

> Like no other technique, the AFM has evolved beyond "passive" imaging to active manipulation and surface probing on a local, a nanoscopic scale. The basis for these capabilities are precise piezo-actuated movements combined with an unmatched force sensing capability of the AFM cantilever.

One way to overcome the diffraction limit of light and resolve surface structures as small as individual atoms[1, 2] is realized in the setup of an atomic force microscope (AFM) (Figure 4 a).[3] The pivotal element of an AFM is a microscopic cantilever whose vertical deflections (in z-direction, normal to the sample plane) can be monitored with utmost precision. Key to that precision is the optical lever technique where a laser beam is focused on the cantilever's back and reflected onto a quartered photodiode (as illustrated in Figure 4 a).[4] Every deflection of the cantilever will now be immediately transferred to the photodiode as an amplified positional shift of the laser's reflection. This mechanism facilitates even minute cantilever deflections (< 1 nm) to be traced if the optical path of the laser is sufficiently long. The cantilever deflections can be detected as the light intensity difference between upper and lower half of the photodiode (analogous for torsions and the ratio

* This chapter is partly adapted from "AFM-Based Mechanical Characterization of Single Nanofibres", B.R. Neugirg, S.R. Koebley, H.C. Schniepp, A. Fery, Nanoscale, 2016, 8 (16), 8414-8426 by permission of The Royal Society of Chemistry

left to right half on the photodiode). The photodiode then directly converts the differences in light intensity to a voltage output signal. Combining such a detection system with an accurate x, y, z-piezoelectric-positioner controlling the relative spatial arrangement of cantilever with respect to the surface is the principle of most AFMs. The z-piezo-element adjusts the vertical distance between cantilever and surface and might use the deflection voltage to feedback.

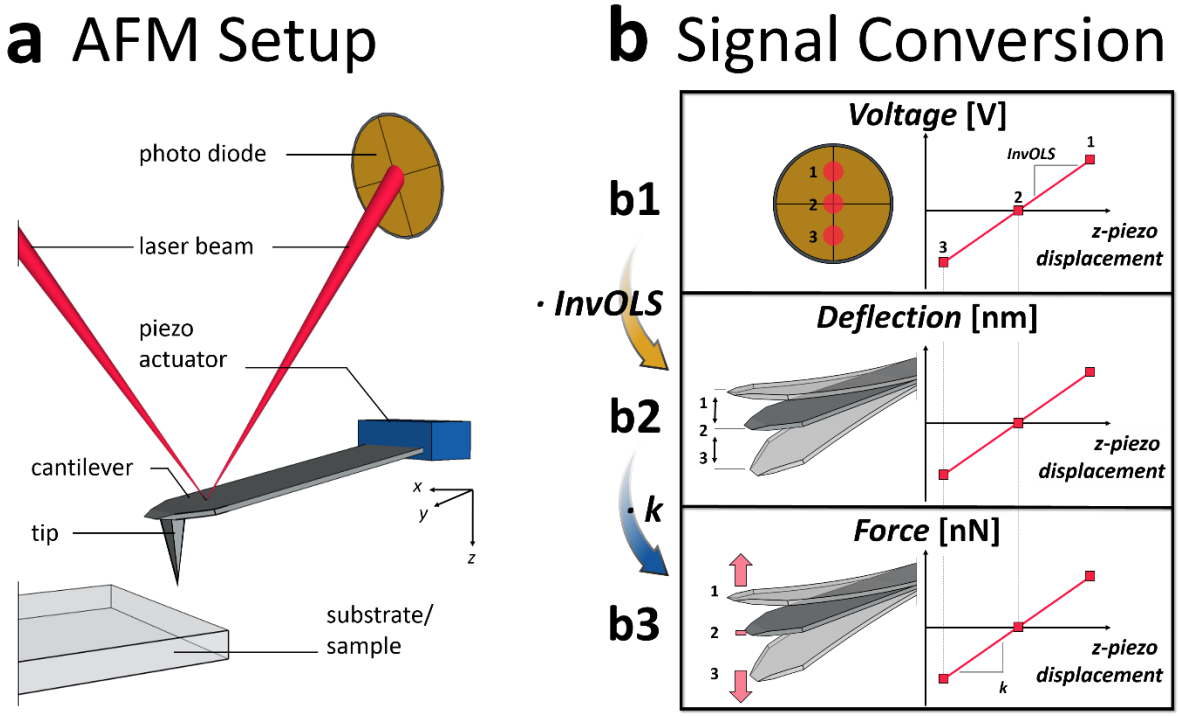

Figure 4| Principal components comprising an AFM setup (**a**) and signal conversion from raw data voltage on the quartered photodiode via cantilever deflection to acting forces (**b**).

The easiest way to generate a topographical image of a surface with such a setup is to scan a sufficiently soft cantilever in consecutive adjacent lines across that surface at immediate contact. The cantilever deflections during each of those scan lines will directly follow the surface topography and translate it to relative light intensities on the photodiode segments. From the resulting voltage output and the corresponding motions of the x, y, z-piezo-positioner, the topography itself can be reconstructed. To maximize in-plane (= x, y) resolution, each scan line should be as thin as possible. Therefore, typical imaging cantilevers are equipped with a sharp tip of typical apex radii around 10 nm. Advancing over the last decades, further (dynamic) modes of imaging have been developed

to either reduce cantilever-surface interactions,[5, 6] or to extract a variety of additional surface properties during scanning.[7, 8]

Cantilever Calibration

The AFM principle also bears the potential to directly quantify the interactions a cantilever experiences with a surface on its nanoscopic, local scale. To achieve quantification, a calibration of the system is mandatory and eventually links the obtained output voltage (Figure 4 b1) of the photodiode with the actual forces acting on the cantilever upon z-piezo displacement (Figure 4 b3). Usually the calibration is subdivided into two steps: 1) determination of the inverse optical lever sensitivity ($InvOLS$) [m/V],[9] which relates the photo voltage signal to the cantilever deflection distance (Figure 4 b2), and 2) calibrating the cantilever's spring constant k [N/m],[10-12] which allows conversion of cantilever deflection into force F. These two steps and selected ways to obtain the two proportionality constants - $InvOLS$ and k - are summarized in Table 1 and an in-depth discussion can be found in ref.[13]

In general, $InvOLS$ and k depend on the direction of the acting force, i.e. when the cantilever is deflected vertically (in z-direction), the vertical $InvOLS$ and k_z have to be determined and contrarily, when the cantilever is bent in x-direction, the respective torsional or lateral quantities are required. In both cases, the $InvOLS$ can be derived from a regime, where the cantilever is in direct contact with an approximately infinitely hard substrate (Table 1). There, the known piezo-displacement is directly proportional to the monitored photodiode output, hence, the $InvOLS$ is found as the proportionality constant.

Table 1| Selection of vertical and lateral calibration methods for rectangular AFM cantilevers.

	vertical (z-direction)	lateral (x-direction)
InvOLS	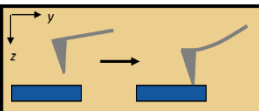 vertical force curve vs. hard substrate	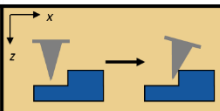 lateral force curve vs. hard vertical step
spring constant vertical k_z lateral k_x torsional k_ϕ	beam mechanics:[1] $k_z = \frac{Ewt^3}{4L^3}$	beam mechanics:[1] $k_x = \frac{Gwt^3}{3LH^2}$
	thermal noise method:[2] $k_z = \frac{k_b T}{P}$	-
	normal Sader method:[3] $k_z = 0.1906\rho w^2 L Q_z \omega_z^2 \Gamma_i^z(\omega_z)$	torsional Sader method:[4] $k_\phi = 0.1592\rho w^4 L Q_\phi \omega_\phi^2 \Gamma_i^\phi(\omega_\phi)$
$k_x = \frac{k_\phi}{H^2}$	relationship:[1] $k_x = \frac{4G}{3E}\left(\frac{L}{H}\right)^2 \cdot k_z$	

Definition of physical quantities: Young's modulus E, shear modulus G, cantilever length L, width w, and thickness t, lever arm H, Boltzmann's constant k_b, power P, temperature T, density of surrounding fluid ρ, quality factor Q_z and Q_ϕ, resonant frequency ω_z and ω_ϕ, imaginary component of hydrodynamic function Γ_i^z or Γ_i^ϕ

[1] Munz M. Force calibration in lateral force microscopy: a review of the experimental methods. *J Phys D-Appl Phys* 2010, **43**(6).
[2] Hutter JL, Bechhoefer J. Calibration of atomic-force microscope tips. *Rev Sci Instrum* 1993, **64**(7): 1868-1873.
[3] Sader JE, Chon JWM, Mulvaney P. Calibration of rectangular atomic force microscope cantilevers. *Rev Sci Instrum* 1999, **70**(10): 3967-3969.
[4] Green CP, Lioe H, Cleveland JP, Proksch R, Mulvaney P, Sader JE. Normal and torsional spring constants of atomic force microscope cantilevers. *Rev Sci Instrum* 2004, **75**(6): 1988-1996.

With respect to cantilever spring constants, a plethora of approaches has been suggested.[13] A selection of fast, convenient and widely accepted ones (which were also used in this thesis) are summarized in Table 1. In principle, the spring constants can be calculated based on beam mechanics,[13] derived via the equipartition theorem in thermal equilibrium ("thermal noise method"),[11] or deduced from the cantilevers vibrations in a surrounding medium ("Sader method").[12, 14] Notably, the cantilever spring constant in an AFM-based nanomechanical experiment must closely match the effective sample spring constant in order to achieve the appropriate force sensitivity; otherwise, deflection may either exceed the range of the photodiode (if the cantilever is too soft) or be so weak as to be indistinguishable from systemic noise (if the cantilever is too stiff).[15, 16]

With long range forces acting, or when the cantilever is in contact with a deformable substrate, the z-piezo displacement is not equal to the distance travelled by the cantilever tip. Rather, it is convoluted with the contribution of the cantilever deflection itself. Therefore, it is necessary to subtract the cantilever's deflection from the raw z-piezo displacement data[4] to obtain the distance d, i.e. the probe tip's true distance from the surface or, if the tip and sample are in contact, the deformation of the sample.

The Force-Distance Curve

In this work, predominantly quasi-static force measurements have been employed. Such measurements always result in an $F - d$ plot, the so-called ***force-distance curve***.[17]

A force-distance curve is the graphical representation of one approach-retraction cycle of the cantilever with respect to the surface or the sample, respectively (Figure 5). Once the cantilever is calibrated, one obtains the precise separation of cantilever and sample or deformation of the sample, i.e. the respective d and the accordingly acting forces, F.[17]

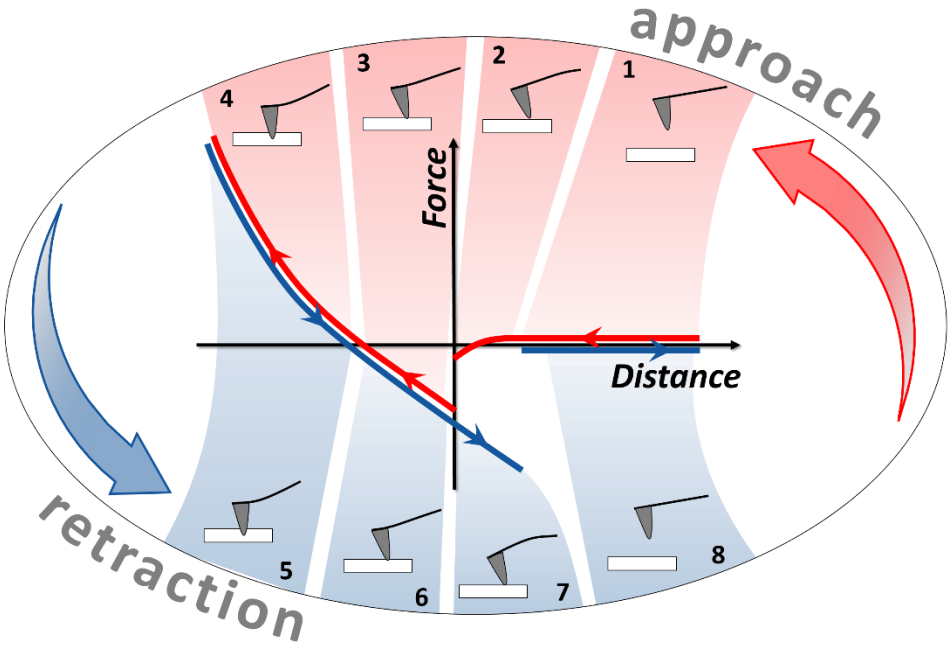

Figure 5| Schematic representation of the force-distance characteristics during an approach-retraction cycle of a cantilever to a surface. Steps 1-4 represent the approach, steps 5-8 the retraction part.

A typical force-distance curve can be subdivided in an approach and a retraction part (Figure 5):

Approach: Far away from any surface, the cantilever is unperturbed and in its equilibrium position, which is defined as zero force (= the baseline) (step 1 in Figure 5). Upon approach, long-range forces may start acting on the cantilever causing a deflection towards (attractive, negative forces, step 2) or away (repulsive, positive forces) from the sample. At close distance, the (attractive) forces might surpass the cantilever's spring constant and cause a sudden snap into contact (end of step 2).

Pushing the cantilever further downwards, will make it pass through its equilibrium position (= zero force after step 3) and eventually deflect it upwards (step 4). Thereby, the cantilever applies a pre-defined load and possibly deforms the sample, which may result in a (non-)linear regime of constant compliance.

Retraction: The pre-defined force set-point is the lower positional turning point of the cantilever and the maximum force in a force-distance curve. Given that all deformations are elastic, the retraction motion reverses all deformations and returns the cantilever to its initial position far away from the surface (steps 5 through 8). Yet, most often approach and retraction curve will not coincide, especially in the non-equilibrium region where the cantilever snaps off contact (end of step 7). There, adhesive surface forces will hold on to the cantilever beyond the previous point of snap into contact thus causing this hysteresis. The force minimum is called adhesion peak.

It is important to keep in mind that the force-distance curve is a convolution of the Hookean force of the cantilever and the true cantilever-surface interaction.[18] Therefore, for instance, the positions of the instabilities jump-to- and jump-off-contact largely depend on the chosen cantilever spring constant.

The principle of a force-distance curve can be employed to study long-range (see chapter IV.3) or adhesion forces as well as mechanical deformations of different kinds of specimen (for nanofiber deformations see chapters II.3, IV.1, and IV.2).

II.3 Mechanical Testing of (Nano-)Fibers*

Nanoscale fiber testing imposes several requirements on the testing method that cannot be met by conventional techniques. AFM-based three-point deformation tests represent a facile and actively used approach.

Quasi one-dimensional objects of nanoscale diameter (i.e. fibers, wires, tubes, whiskers, etc., collectively termed "fibers" henceforth) form the fundamental building blocks of numerous mechanically superior natural and synthetic materials (see chapter I).[19, 20] The nanoscale diameters are believed to both decrease the probability of flaws or defects and increase the fiber's surface area-to-volume ratio, hence causing physical properties distinct from bulk.[21-25] Characterizing and understanding the fibers' mechanical properties are important with respect to implementation in any possible application. However, most conventional testing techniques fail when fiber diameters and lengths undercut approximately one micron and several mm, respectively. The force sensing capabilities and spatial resolution of the atomic force microscope (AFM) allow one to overcome these challenges, and several AFM-based mechanical nanofiber testing approaches have emerged. The most common of these approaches are: ***(AFM-based) tensile testing***, ***three-point deformation testing***, and quasi-static nanoindentation (Figure 6) where only the former two probe the fiber along its longitudinal axis and are reviewed in the following.

* This chapter is adapted from "AFM-Based Mechanical Characterization of Single Nanofibres", B.R. Neugirg, S.R. Koebley, H.C. Schniepp, A. Fery, Nanoscale, 2016, 8 (16), 8414-8426 by permission of The Royal Society of Chemistry

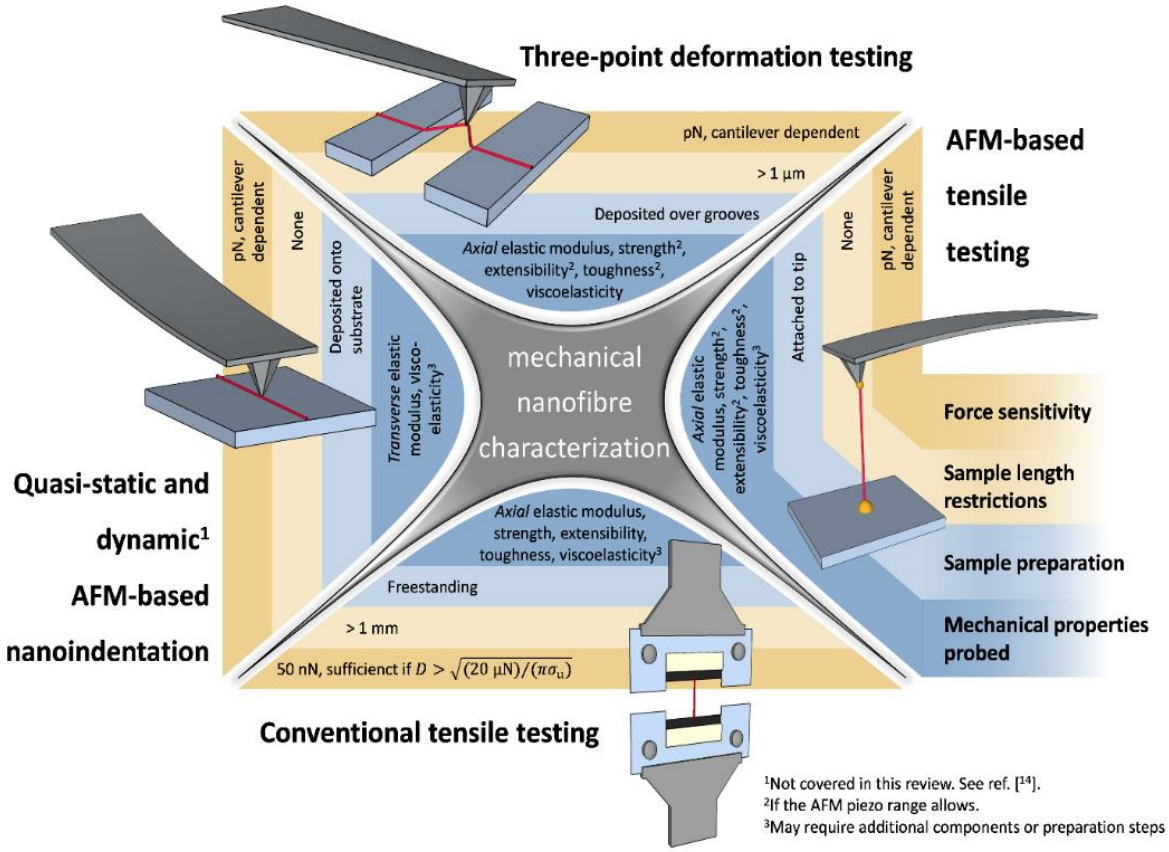

Figure 6| Schematic overview of the major conventional and AFM-based techniques for measuring the mechanical properties of nanofibers. Each technique is characterized by its force sensitivity, restrictions on the sample length, sample preparation requirements, and mechanical properties probed. Reproduced from "AFM-Based Mechanical Characterization of Single Nanofibres", B.R. Neugirg, S.R. Koebley, H.C. Schniepp, A. Fery, Nanoscale, 2016, 8 (16), 8414-8426 by permission of The Royal Society of Chemistry.

(AFM-based) Tensile Testing

The standard technique for acquiring a fiber's mechanical properties is tensile testing, which involves extending the fiber ends in opposite directions at a controlled rate while monitoring the force using a capacitor load cell. This method is well-established, accurate, and involves a simple attachment of the fiber ends via clamping. However, conventional tensile testing is not applicable in many nanoscale systems. The tensile tester most specialized for the characterization of nanofibers has a claimed force sensitivity of 50 nN and extension resolution of 35 nm.[26, 27] For a rough estimate of the thinnest, weakest fiber that can be tested with the claimed 50 nN sensitivity, we assume that

at least 100 discrete force delineations in the resulting stress–strain curve are desired. With this requirement, tested fibers must approximately satisfy $5\ \mu\mathrm{N} < A\sigma_\mathrm{u} = \pi(D/2)^2\sigma_\mathrm{u}$, where σ_u is the fiber's ultimate strength, A is the cross-sectional area, and D is the cylindrical fiber diameter. The mechanical properties of a fiber can therefore be probed with a tensile tester if $D > \sqrt{\frac{20\ \mu\mathrm{N}}{\pi\sigma_\mathrm{u}}}$. Another, potentially more serious challenge to nanoscale tensile testing is sample preparation, which demands that the fiber be suspended between the two arms of the tensile tester. The fiber must therefore be at least ≈1 mm in length (5 mm is typical) and freestanding—conditions that are often attainable by microscale fibers such as spider silks,[28-30] but only rarely met by nanoscale fibers, e.g. in some studies of electrospun polymers.[31-35]

AFM-based tensile testing is a similar approach to conventional tensile testing that is in principle not limited by fiber length or force sensitivity, yet employs the same deformation geometry of uniaxial stretching along the fiber axis. In this method, which is a form of force spectroscopy, a nanofibrillar sample—e.g. carbon nanotube,[36] WS_2 nanotube,[37] gold nanowire,[38, 39] polymer fiber,[40-42] or collagen fibril[40, 43-47]—is grown or attached to both the AFM probe tip and the substrate, and the force on the tip is determined as the probe is retracted. Similarly, material can be attached to an AFM tip, manipulated into a fibrillar, dogbone-shaped structure using a focused ion beam (FIB), and force spectroscopy can be conducted to yield the material's stress–strain response.[48]

Nanoscale tensile testing conducted both with the AFM and with specialized microelectromechanical systems (MEMS)[49-55] has produced reliable results for nanofibers. However, attachment of the fiber in these arrangements is tedious and may be prohibitive in many cases: the fiber must be grown between tip and sample[38, 39] or attached via elaborate micromanipulation[41-43, 45-47] that often requires the use of a combination SEM–AFM system.[36, 37, 40, 44, 48] If imaging and treatment in an SEM is involved, the sample usually becomes dehydrated, and in some cases metallic coatings are applied to the sample to provide electrical conductivity, which may further alter its mechanical properties. Similarly, ion bombardment in a FIB must be executed with particular caution, as it has been shown to mechanically strengthen the sample.[56, 57] In light of these preparation complexities, alternative techniques with fewer sample manipulation and attachment demands are often desirable.

AFM-based Three-Point Deformation Testing

In most AFM-based three-point deformation tests, sample preparation is as simple as depositing fibers onto a hard substrate that is prestructured with grooves. Fibers will statistically span these grooves, leaving segments suspended. The suspended portions of the fibers can then be probed by an AFM cantilever tip to perform a three-point deformation test. This approach achieves nanoscale force and spatial resolution, allowing for specimens with nanometer-sized diameters and lengths below 1 µm, e.g. individual single-walled carbon nanotubes.[58] In most cases, the three-point deformation test primarily aims to determine the axial Young's modulus of fibers, the modulus also probed by tensile testing. By adjusting the suspended length and deformation range, one can further determine the bending and shear moduli,[59] yield point,[60] viscoelasticity,[61] toughness and strength,[62] and even rupture properties such as a fiber's extensibility.[63] Beyond probing mechanical parameters under standard conditions, the AFM's general tolerance for different ambient conditions enables a widespread range of samples and facilitates testing of the fibers' performance in different media[64, 65] or at different temperatures,[66] as well as their in-situ responsiveness to pH changes.[67] Furthermore, the testing setup can be combined with conductivity measurements to directly monitor the strain dependence of current flow across the fiber.[58, 68, 69]

Vertical and Lateral Deformation Experiments

Experimentally, three-point deformation tests can be distinguished by their loading direction relative to the substrate and deformation range: the test involves either vertical loading and a relatively small deformation (Figure 7a) or lateral loading and a large deformation (Figure 7b). In the former approach, the cantilever moves vertically (in the z-direction), pressing the suspended fiber segment downwards while being deflected upwards. For vertical cantilever deflections, calibration is more straightforward; however, the limited displacement of the z-piezo (typically ≈10 µm) confines the range of fiber deformation. Hence, vertical three-point bending is sometimes limited to small deflections of relaxed fibers in the linear elastic regime, and is thus ideally suited to determining the fiber's axial Young's modulus or its bending and shear moduli.[59, 64, 70]

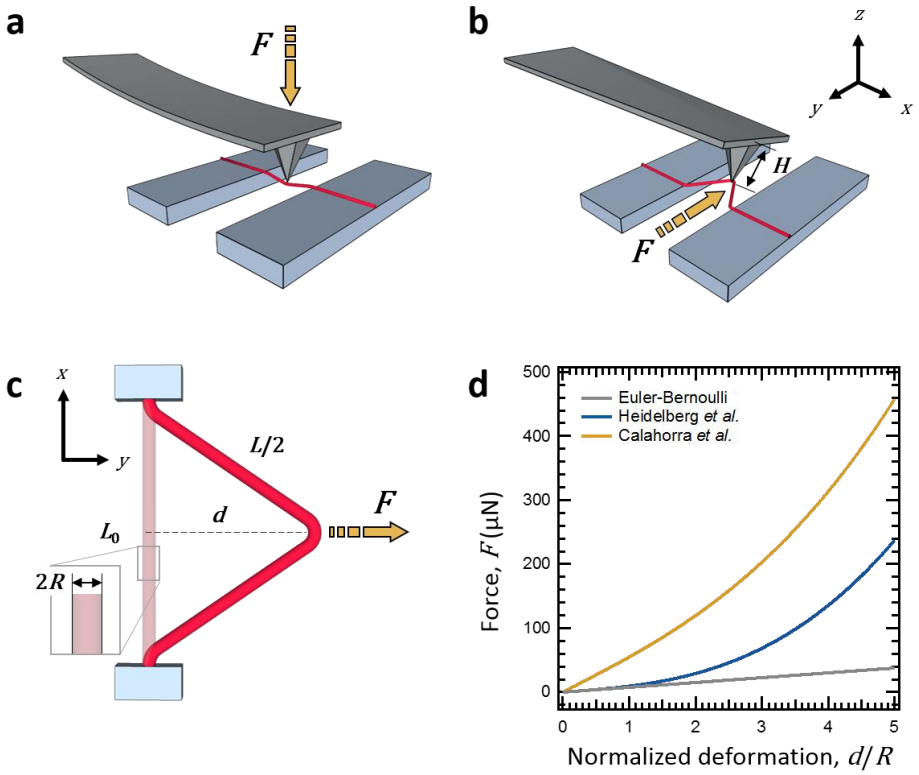

Figure 7| Schematics of vertical (**a**) and lateral (**b**) three-point deformation testing. In both approaches a (usually clamped) fiber segment is subjected to a load $\boldsymbol{F}$. Denominations of the physical values are given in (**c**). Exemplary force vs. deformation (normalized to the fiber radius) dependencies according to the models of Euler–Bernoulli (pure bending), Heidelberg et al.[71] (bending and stretching) and Calahorra et al.[72] (bending and stretching of a pre-strained fiber) are given in (**d**). Adapted from "AFM-Based Mechanical Characterization of Single Nanofibres", B.R. Neugirg, S.R. Koebley, H.C. Schniepp, A. Fery, Nanoscale, 2016, 8 (16), 8414-8426 by permission of The Royal Society of Chemistry.

In the second approach, lateral loading, the cantilever tip travels in the x, y-plane and intersects the suspended fiber segment perpendicularly at its midpoint (Figure 7b). The fiber experiences both bending and stretching, imposing torsion on the cantilever at a certain lever arm H (Figure 7b), which is defined as the distance from the cantilever long axis to the tip's contact point with the fiber. This torsion renders the data conversion to forces more intricate, as the lateral optical lever sensitivity and the lateral spring constant need to be known precisely. To date, no experimental method to obtain these two parameters has emerged as general standard, yet, various approaches exist: the lateral spring constant for instance can be derived using the torsional Sader method[14] or

by calculation from cantilever dimensions. The reader is referred to chapter II.2 and a recent comprehensive review on this topic by Munz.[13] Nevertheless, exploiting the generally larger x, y-piezo reach by lateral loading facilitates larger fiber deformations, enabling a complete mechanical characterization—from the elastic regime to rupture.

Pure Bending Regime

Regardless of loading direction, both testing techniques deform the fiber perpendicular to its long axis, causing similar strains in a radially symmetric specimen. Deformations of less than one fiber radius predominantly cause bending: at the bending points (the edges of the grooves and the tip–fiber contact), the convex side experiences tensile strain, while the concave side experiences compressive strain. Additionally, these strains increase radially from the neutral plane to the fiber surface, resulting in an inhomogeneous stress distribution with local stress peaks. These bending deformations can be well described by the classical Euler–Bernoulli beam model, which takes into account the fiber's boundary conditions, i.e. whether it is simply supported by or firmly attached to the substrate.[73]

An advantage of the vertical loading approach is the relative ease of using Force–Volume plots[65, 70, 74-76] or advanced force imaging techniques,[77, 78] which allow one to map the fiber response as a function of position and thereby directly determine the present boundary conditions. If F is the force applied at the position x along the fiber axis, causing a deformation d, the ratio of $F(x)/d$ can be interpreted as the fiber's stiffness at the respective position (Figure 7c). A measured stiffness profile along the suspended segment can then be compared to models for different boundary conditions. For a simply supported beam, the model suggests:

$$\frac{F(x)}{d} = \frac{3L_0 EI}{(L_0 - x)^2 x^2} \qquad \textit{Equation 1}$$

In the case of a double-clamped beam one finds:

$$\frac{F(x)}{d} = \frac{3L_0^3 EI}{(L_0 - x)^3 x^3} \qquad \textit{Equation 2}$$

In both cases, L_0 is the initial length of the suspended segment and $0 \leq x \leq L_0$, E is the axial Young's modulus, and I is the area moment of inertia, where $I = \pi R^4/4$ for cylindrical fibers with radius R (Figure 7c).

Kluge et al. compared the rigidities and Young's moduli derived from such stiffness profiles of three different 1,3,5-benzenetrisamides that each self-assemble into supramolecular nanofibers.[70] They focused on results where the boundary conditions were unambiguously found to be double-clamped and measured Young's moduli in the lower GPa range. In contrast, Ling et al. found self-supporting particle bridges cohered by a supramolecular glue to follow the model of a simply supported beam.[79] This shows that clamping of the fiber to the supports is not absolutely necessary as long as clamping conditions are determined in each situation, especially since data interpretation in the framework of the wrong boundary conditions would lead to a Young's modulus off by a factor of 4 (as approximated using $x = L_0/2$ and comparing *Equation 1* and *Equation 2*). In other studies, both boundary conditions and, occasionally, a mixed case (one side clamped, one simply supported) were observed within one respective fiber–substrate system.[76, 77, 80] For instance, Chen et al. probed the stiffness profiles of silver nanowires with diameters between 66 and 141 nm using digital pulsed force mode.[77] They pointed out the importance of the boundary conditions, as thinner nanowires resembled a double clamped beam whereas thicker ones were simply supported. Both cases yielded moduli close to the bulk value of silver.

In the majority of three-point bending studies, however, fibers are assumed to be double clamped due to sufficient fiber–substrate adhesion[81, 82] or double clamped conditions are enforced by additional experimental measures.[60, 83] Probing with a force F_c at the segment midpoint ($x = L_0/2$) reduces *Equation 2* to:

$$F(L_0/2) = F_c = \frac{192EI}{L_0^3} \cdot d \qquad \textit{Equation 3}$$

(gray line, Figure 7d). Due to the shape of the stiffness profile (*Equation 2*), the force response is relatively insensitive to small positioning deviations from the midpoint, increasing the robustness of the method.[84, 85] In the case of sufficient fiber–substrate adhesion, the midpoint probing approach allows for relatively low expenditure of experimental time, hence facilitating larger sample numbers. For example, Stachewicz et al. provided a thorough experimental basis demonstrating a modulus increase with decreasing diameter for electrospun polyvinyl-alcohol fibers.[82] They attributed this trend to the fibers' core–shell structure caused by the high shear in electrospinning.

The Superposition of Bending and Stretching

Lateral three-point deformation tests mostly deform fibers beyond the bending regime (deformation d exceeding the fiber radius R), and often aim to break or rupture the fiber. As the

fiber is increasingly stretched, tensile stresses in the straight specimen portions are superimposed with tensile and compressive stresses at the bending points (as mentioned above). For large yet elastic deformations, Heidelberg et al. introduced a factor $f(\alpha) > 1$ to account for this resulting rigidity enhancement in double clamped beams (blue line, Figure 7d).[71]

$$F_c = \frac{192EI}{L_0^3} \cdot f(\alpha) \cdot d \qquad \textit{Equation 4}$$

Where

$$f(\alpha) = \frac{\alpha}{48 - \frac{192 \cdot \tanh(\sqrt{\alpha}/4)}{\sqrt{\alpha}}}, \qquad \textit{Equation 5}$$

$$\alpha = \frac{6\varepsilon(140 + \varepsilon)}{350 + 3\varepsilon} \qquad \textit{Equation 6}$$

and

$$\varepsilon = d^2(A/I) \qquad \textit{Equation 7}$$

Here, A is the fiber's cross-sectional area. This model succeeds in describing the full elastic response of a fiber, e.g. high modulus inorganic nanowires,[68, 71, 86-89] therefore allowing the transition from elastic to plastic deformation to be determined. Wen et al. applied this model to demonstrate that the Young's modulus of ZnO nanowires resembles the bulk value and can be regarded essentially diameter-independent in the range from 18 to 304 nm.[88] Recently, McCarthy et al. used *Equation 4* - *Equation 7* to calculate the Young's modulus of nickel and silver nanowires and to verify the elasticity of the applied deformations, a prerequisite for their determination of the Poisson's ratio of these wires from strain-dependent four-point resistance measurements.[68] Furthermore, since this model extends to higher deformations than classical bending (*Equation 3*), it is more sensitive to experimental inconsistencies. For instance, pre-strained fibers can be identified since their deformation data would not fit the model, and modulus overestimation can hence be prevented (see Figure 7 d).

The Role of Pre-Tension

Despite its applicability over the full elastic regime, the Heidelberg model was not employed for soft matter fibers at all, probably because of significant residual tension in these systems. With decreasing material modulus, pre-tension inherent in a fiber (from the preparation or clamping procedure) increasingly dominates its force response. This is manifested in a steeper slope of the

initial linear bending regime (where $d < R$) in force–deformation curves (yellow line, Figure 7 d). Pre-tension was first investigated in spider mite silk, in which tension was naturally introduced as the mites drew silk from their spinning glands and deposited it onto the test substrate.[84] Hudson et al. implemented the effect of pre-tension in a numerical model by expanding the factor $f(\alpha)$ in *Equation 4*.[84] Calahorra et al., who also recently observed such residual stresses in hard silicon nanowires, approximated the full solution for the expanded $f(\alpha)$ by an analytical expression[72, 90] for the ease of application:

$$f_{\mathrm{approx}}(\alpha_{\mathrm{approx}}) = 1 + 2.412 \cdot 10^{-2}\alpha_{\mathrm{approx}} - 1.407 \cdot 10^{-6}\alpha_{\mathrm{approx}}^2 \qquad \textit{Equation 8}$$

Where α_{approx} includes the initial pre-tension force T_0:

$$\alpha_{\mathrm{approx}} = \frac{L_0^2 T_0}{EI} + \frac{6\varepsilon(140 + \varepsilon)}{350 + 3\varepsilon} \qquad \textit{Equation 9}$$

The Heidelberg model, now expanded for pre-tension, enables a comprehensive data interpretation of elastic deformations in double clamped three-point deformation tests. Beyond the limit of one fiber radius of deformation, the tensile contribution increasingly dominates the fiber's force response. In that regime, the linear dependence of force on deformation passes into a cubic dependence, rendering the bending contributions gradually negligible. In the work of Schniepp et al., thin ribbons of nanometer thickness were deformed several µm to derive the Young's modulus based on a purely tensile model, as the bending component is negligible for thin ribbons.[91] Presuming only stretching of the fiber, one can easily convert the measured force and deformation to (axial) stress and strain.[62, 92] This approach yields lower estimates for fiber failure properties, such as maximum strength, extensibility and toughness.[58, 61, 62, 91, 92] Biopolymer fibers were mechanically characterized using this same approach, revealing the extraordinary extensibility of fibrin[63, 93] and viscoelastic properties of collagen fibers.[94]

Conclusion

The advancing miniaturization of devices and progressing concentration of different functionalities within a material increasingly demand more sophisticated nanofibrillar building units. The characterization of these building units and the detailed examination of highly evolved natural systems that might serve as models for biomimicry both require high–resolution, reliable testing techniques to assess their respective mechanical spectra. The AFM provides a highly sensitive and thus highly attractive platform for this task. As reviewed here, the intense research conducted in the

field of nanofiber mechanical testing in the past decades and the strong trend to implement mechanical mapping techniques in AFM instrumentations illustrate two key points. First, due to its simple sample preparation requirements and universal applicability, AFM-based mechanical fiber characterization is the method of choice for a vast majority of systems. Second, as indicated by the diversity of data interpretation efforts, AFM-based three-point deformation testing and indentation of nanoscale fibers are still not standardized to the degree of conventional macroscale mechanical testing. However, with further efforts to disentangle the many challenges that are present at the nanoscale, the AFM's capabilities of nanoscale manipulation and in-situ force-monitoring make it a uniquely powerful tool in the discovery of single fiber mechanics.

II.4 Interactions in the Colloidal Domain – The DLVO-Theory

Objects with colloidal dimensions (including micro- and nanofibers) mostly interact based on electromagnetic interactions. Especially the dominance of electrostatic and van der Waals interactions is accurately modeled by the DLVO-theory.

On a universal length scale, that ranges from subatomic particles to the expanse of the universe, distinct fundamental forces prevail in different size regimes. At the lower end of this universal scale, the strong and the weak force govern the interactions between elementary particles. At the upper end, gravity determines the interactions of galaxies and eventually the expansion of the universe itself. On a molecular and also on a colloidal scale (nm - µm), neither of those forces predominate, which leaves room for the supremacy of electromagnetic interactions. The electromagnetic forces encompass Coulomb forces between permanent charges, polarization forces between (induced) dipoles, and quantum mechanical forces (chemical bonds, repulsions).[95] The diminished impact of the other fundamental forces on that size scale opens up manifold opportunities to influence each of these three electromagnetic subdivisions, a possibility that provides the basis for chemistry and controls colloidal interactions.

Colloidal interactions and foremost colloidal stability are crucial for a plethora of industrial processes[96] and biological phenomena such as microbial adhesion.[97] Therefore, it is important to ***measure***, ***understand***, and ***control*** these interactions.

From an experimental point of view, ***measuring*** such small scale surface forces has been made possible by the surface force apparatus[98, 99] and the colloidal probe technique,[100] which is based on atomic force microscopy (AFM) (the AFM is discussed in chapter II.2).[101] Especially the latter is attractive due to its versatility. Virtually every colloidal particle can be attached to a tipless AFM cantilever and maneuvered at precise distance control to approach another surface within an immersion medium of choice (Figure 8 a). Simultaneously, the acting forces can be monitored from the cantilever deflection and their distance dependence can be recorded in a force-distance curve $F(d)$ (see chapter II.2).

In such a measurement, the respective forces strongly depend on the particle shape.[95] Especially short-ranged forces are vastly convoluted with surface topography. Thus, to transfer force results $F(d)$ to the universal property of interaction energy $W(d)$, a geometrical normalization is necessary. If the interaction range is small compared to the particles' radii of curvature, the Derjaguin approximation provides such a geometrical normalization with respect to certain shape configurations.[99] Most commonly, forces between a sphere and a plane, two spheres or two crossed cylinders are transferred using the Derjaguin approximation:

$$W(d) = \frac{F(d)}{2\pi R_{eff}} \qquad \textit{Equation 10}$$

Here, R_{eff} is the effective radius, which is equal to the sphere radius R in the case of the sphere-plane interaction and correspondingly $\frac{R_1 R_2}{R_1+R_2}$ for two spheres of radii R_1 and R_2, and $\frac{\sqrt{R_1 R_2}}{\sin\theta}$ for two cylinders of radii R_1 and R_2 oriented at an angle θ.[95, 99]

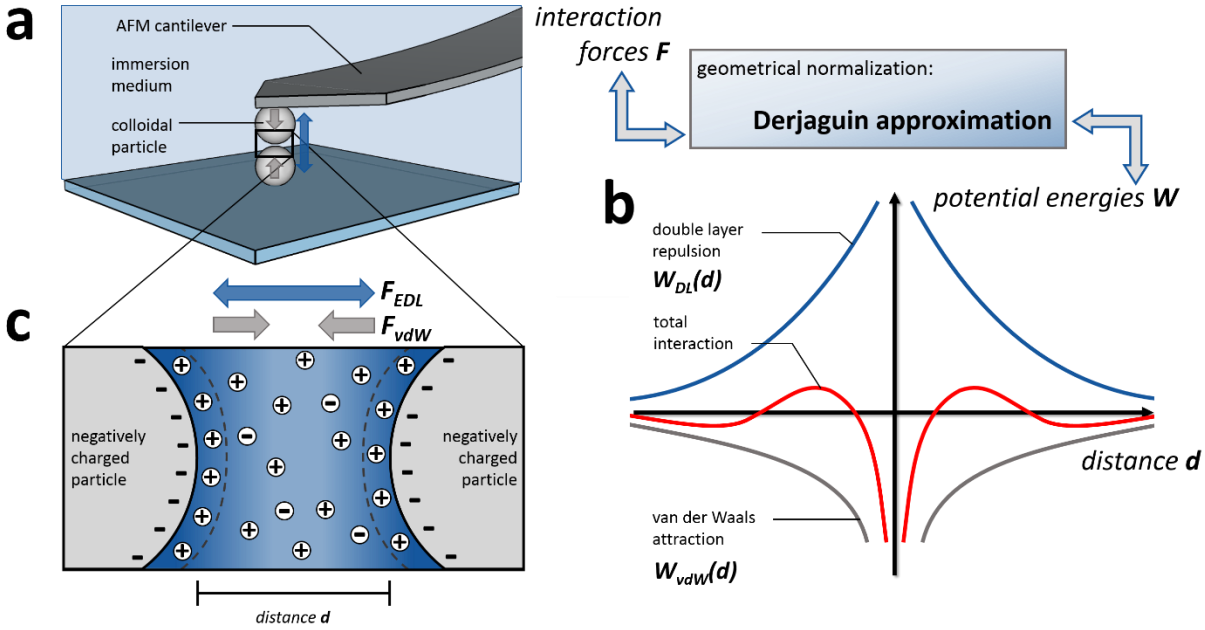

Figure 8| Measurement, interaction energies, and schematic situation between two colloidal particles in a liquid electrolyte solution. (**a**) A colloidal particle attached to an AFM cantilever can be used to directly measure interaction forces with another particle or surface. (**b**) Using the Derjaguin approximation, the acting forces can be normalized with respect to the interaction geometry to potential energies. The sum of repulsive and attractive interactions yields the total interaction energy, which governs colloidal stability. (**c**) Interaction forces between two charged surfaces in a liquid are dominated by the electrostatic repulsion and van der Waals attraction. The former can be influenced by the kind of medium between the surfaces as well as the dissolved electrolyte concentration and the respective ionic valences.

To ***understand*** these interactions, theoretical considerations need to be established that succeed in modelling the interaction-distance $W(d)$ behavior and also allow for reliable predictions. Derjaguin, Landau, Verwey, and Overbeek derived such a theory, which is named after them "DLVO-theory". It describes the interactions of e.g. two planes in-between the two extreme situations of both not interacting at all at "infinite" separation ($d = \infty$) and the barrier of quantum mechanical repulsion upon intimate contact ($d = 0$). Thereby, the DLVO-theory limits itself to the most significant contributions to describe the essential physics of colloidal stability.[102] These contributions are the polarization-based (and usually attractive) van der Waals interaction W_{vdW} (gray line in Figure 8 b) and the Coulomb-based (and usually repulsive) interaction due to the electric double layer W_{DL}

(blue line in Figure 8 b).[99] W_{vdW} for two interacting planar surfaces can be derived from the pair-wise addition of the dipole contributions from all the individual partaking atoms in the two interacting bodies to be:

$$W_{vdW}(d) = -\frac{H}{12\pi d^2} \qquad \textit{Equation 11}$$

where H is the Hamaker constant.[95]

In contrast, for W_{DL} the situation is more complex and demands for certain assumptions. The starting point in considerations of the electric double layer is the Poisson-Boltzmann equation. This is the combination of the Poisson equation, which describes the charge density at each point at any distance d from a surface that bears a potential ψ, and the Boltzmann equation. The latter balances the charge density found at any position within reach of the surface potential ψ with the thermal energy $k_B T$. The combination gives the Poisson-Boltzmann equation that can only be solved numerically unless certain assumptions are employed. In the exemplary case of *Equation 12*, an approximate weak overlap and large surface separations are assumed.[95]

$$W_{DL}(d) = 64 k_B T c_0 \kappa^{-1} \cdot \tanh^2\left(\frac{ze\psi_0}{4k_B T}\right) \cdot \exp(-\kappa d) \qquad \textit{Equation 12}$$

In *Equation 12*, κ^{-1} is a measure for the thickness of the electric double layer, the so-called Debye length, which is defined as:

$$\kappa = \left(\frac{2e^2 c_0}{\varepsilon \varepsilon_0 k_B T}\right)^{1/2} \qquad \textit{Equation 13}$$

The above *Equations 11 - 13* describe the distance dependence of the respective interaction energies between the two planar surfaces. The physical quantities included are the salt concentration c_0 far away from the surface (in bulk), the ion valence *z*, the elementary charge *e*, the potential directly at the surface ψ_0, and the absolute ε and the vacuum permittivity ε_0. The additivity of those two interactions (W_{vdW} and W_{DL}) allows to model and predict e.g. colloidal stability against aggregation for a wide range of systems and yields the DLVO description of interaction energies (red line in Figure 8 c). The transfer of these theoretical interactions to the respective forces can be done using the Derjaguin approximation as mentioned above and of course vice versa.

Prediction of interactions directly relates to the identification of influencing parameters and hence ideally in their ***control***. Van der Waals interactions only depend on the atomic number density and the Hamaker constant, which in turn only depend on the types of materials for the interacting colloids and the immersion medium. Therefore, W_{vdW} is fixed for a given system.
In contrast, W_{DL} depends on a multitude of parameters. The repulsive forces between two similarly charged surfaces arise from the osmotically driven disjoining pressure due to the increased ion concentration as the double layers overlap (Figure 8 c). This situation can be influenced by variations in the surface charge density or potential (e.g. dissociation of surface groups by adjustment of pH), the valence and concentration of the employed salt, the temperature and thermal energy in the system, and the dielectric properties of the surrounding medium. Overall, tuning of W_{DL} allows for stabilization or controlled coagulation of a colloidal system.

Altogether, when dealing with structural components of micro- or nanoscopic (colloidal) size, knowledge about their surface properties is indispensable as these surface forces govern the interactions of the structures with their surroundings. The DLVO-theory has emerged as an extremely successful tool to quantitatively describe these interactions and can be employed to investigate surface charge densities or surface potentials as well as related phenomena.

II.5 Electrospinning – Shaping Materials into (Nano-)Fibers

Exploitation of beneficial nanofiber properties foremost requires a versatile technique to shape materials in that morphology. Yet, the versatility of electrospinning does not stop at materials' choice: like no other, this spinning process opens perspectives to modify the material by the spinning itself.

The versatility of electrospinning arises from its fundamentally different approach towards structure formation. In contrast to conventional techniques, which mostly rely on mechanical forces to draw fibers, electrospinning utilizes strong electrical fields.[103-106] The principal setup is illustrated schematically in Figure 9. A syringe contains a reservoir of the liquid feedstock, which is usually a polymer solution but can also be an emulsion, a suspension or a melt,[104] even of small molecules.[107] The fiber forming process itself takes place between a high voltage electrode connected to the cannula of the syringe and a grounded collector. When the liquid is pumped through the cannula, it forms a pendant droplet at the cannula's tip. The applied high voltage charges the droplet and causes its distortion in the electrical field to the so-called Taylor cone.[108] This distortion is the result of balancing repulsive electrostatic forces of the charges on the droplet's periphery and the surface tension, which tries to minimize the droplet-air interface. If the charging surpasses a threshold value, a thin jet is ejected to stabilize the situation transporting charges to the ground electrode. On the initial straight part of the jet, repulsive forces still dominate and lead to further straining the jet. This straining stabilizes the jet's trajectory but decays with distance from the cone. Eventually, foremost the bending instability will take effect and cause the jet to whip in loops with growing amplitudes and at ever smaller, self-similar scales until the jet hits the collector.[109, 110] During the travel from Taylor cone to collector, solid fibers with nanoscale diameters are formed as the solvent can evaporate rapidly and the fibers' straining and stretching is accompanied by a significant decrease in diameter.

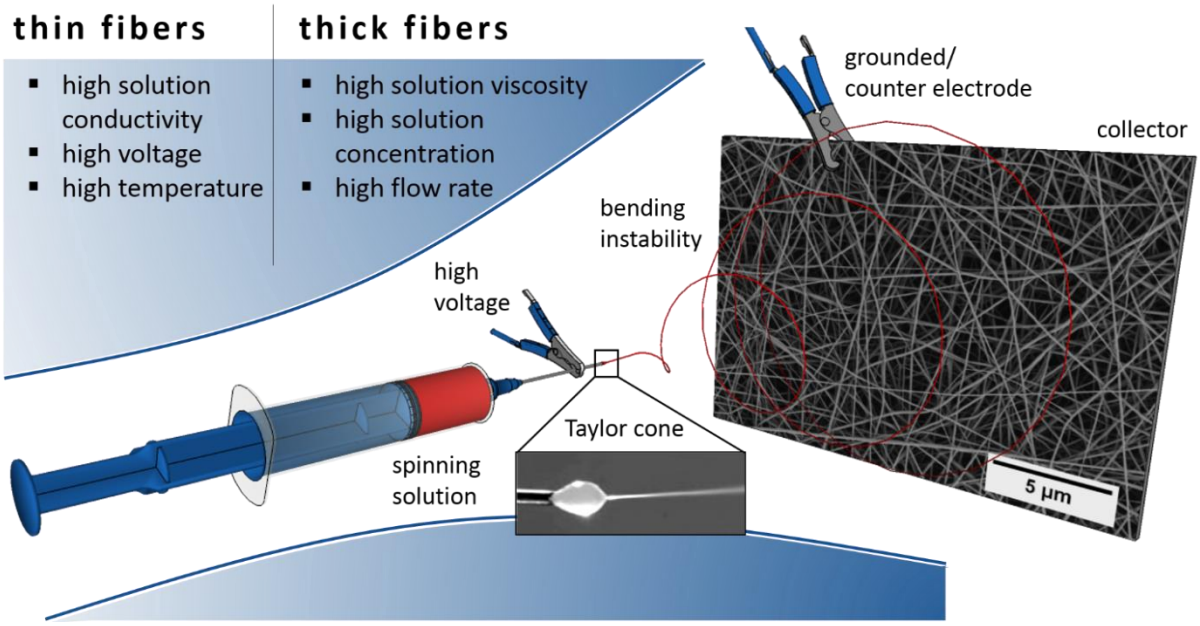

Figure 9| Schematic electrospinning setup with optical image of a Taylor cone during fiber spinning (adapted with permission from reference [104]) and an SEM micrograph of a collected polyamide fiber mat (courtesy of Matthias Burgard). A selection of spinning parameters that influence the fiber diameter are given on the top left.

In this elementary form, the electrospinning process is a low-tech hence low-cost but exceptionally versatile way to shape a wide variety of materials into continuous nanofibers. The process is susceptible to a multitude of parameters that allow for control of fiber shape and diameter (in the range of several nm to a few µm). Those parameters can be roughly grouped to solution parameters (solution concentration, surface tension, conductivity and viscosity), process parameters (applied voltage at cannula – collector distance and feeding rate), and environmental parameters (mostly temperature and humidity).[105] The upper part of Figure 9 gives a selection of the main parameters influencing the fiber diameter. Beyond solid and smooth fibers, tuning the aforementioned parameters, modifying the nozzle geometry, blending materials or post-treating fiber mats facilitates the production of a wide variety of other related yet more complex morphologies. Hybrid, side-by-side and core-shell fibers, hollow tubes or highly porous structures are just a few examples.[104, 111-113] Obviously, the attractiveness of such morphologies comes from the compartmentalization that facilitates additional functionality or the vastly increased surface areas.

Apart from the diverse functionality of complex morphologies, plain solid nanofibers and their respective assemblies in nonwovens are highly attractive for many applications. First, there are biomedical applications that aim to use nonwovens or nanofiber scaffolds for tissue engineering, wound covering or drug delivery. These applications benefit from electrospun fiber mats closely mimicking the extracellular matrix with suitable mat porosity and surface area, mechanical properties, biodegradability and degradation time, and the ease of further biofunctionalization.[114, 115] Secondly, metallic, ceramic or composite nanofibers can be used due to their confined quasi-one-dimensional structure in technical applications exploiting their specific photonic, magnetic and electronic properties.[103] Third, nanofibers and fiber mats thereof are employed in filtration,[116] as catalyst carriers[111] and as reinforcements[117] due to their exceptional mechanical properties and their high surface-to-volume ratios.[104] The generally observed improvement of the mechanical properties with decreasing fiber diameters can be attributed to the molecular alignment during spinning as well as the reduced concentration of defects.[117, 118]

Despite the dissimilarity of those three groups of applications, in all of them a thorough understanding of single fiber mechanics as well as the surface properties of the fibers are crucial. The concerted fiber mechanics and their interactions amongst each other (or with an embedding matrix) determines the success or failure of a material or device in virtually every field of application. A detailed discussion of individual fiber mechanical testing is given in chapter II.3, an overview over colloidal interaction forces dominating that size domain can be found in chapter II.4.

II.6 Natural and Recombinant Spider Silk

The lessons spider silk teaches are as manifold as its astonishing properties. To understand a hierarchical material adapted for various environmental conditions, probing the material on the different hierarchal levels while varying these environmental conditions is pivotal.

An orb-weaving spider's dragline silk is a biomaterial, which is exemplary for highest efficiency achieved by controlled hierarchical structuring. Highest efficiency in this case means on the one hand that the dragline thread can absorb more energy per weight than most other biological or man-made materials including Kevlar and steel.[119, 120] On the other hand, silk is spun extremely efficiently at benign conditions from an aqueous solution within fractions of seconds.[121, 122] Besides the mechanical strength and the astonishing spinning process, spider silk is also biocompatible, bacteriostatic and of course biodegradable, features that open up various medical applications.[123] And even beyond that, dragline silk amazes with self-reconstitution via supercontraction[124] and a shape memory behavior.[125]

Natural Silk

The very basis of all material properties is the primary structure of the proteins that form spider silk, the so-called spidroins.[126, 127] The dragline thread of the European garden spider (*Araneus Diadematus*) contains two large spidroins that resemble a primary structure as schematically shown in Figure 10 a.[122] A central domain, which is composed of frequently repeated and alternating motifs of alanine-rich and glycine-rich units, is capped on both ends with a non-repetitive C- or N-terminus, respectively.[119]

The spidroins are secreted and stored in the tail and the ampulla of a specialized spinning gland within the spider's abdomen (Figure 10 b yellow region), in the case of dragline silk the gland is called the major ampullate gland. Particularly spidroin storage is a critical aspect, as the spinning solution has to be highly concentrated (up to 50 % w/v)[121] for abundant availability when needed, yet, unspecific protein aggregation has to be strictly avoided.[122] To face this issue, the non-repetitive termini, which were found to be highly conserved throughout different species, play a decisive role: upon interlocking of two distinct C-terminal domains, spidroins form amphiphilic dimers. These

dimers assemble in a liquid crystalline micellar-like structure, which remains stable even at the high concentrations that are typically found within the ampulla.[120, 121]

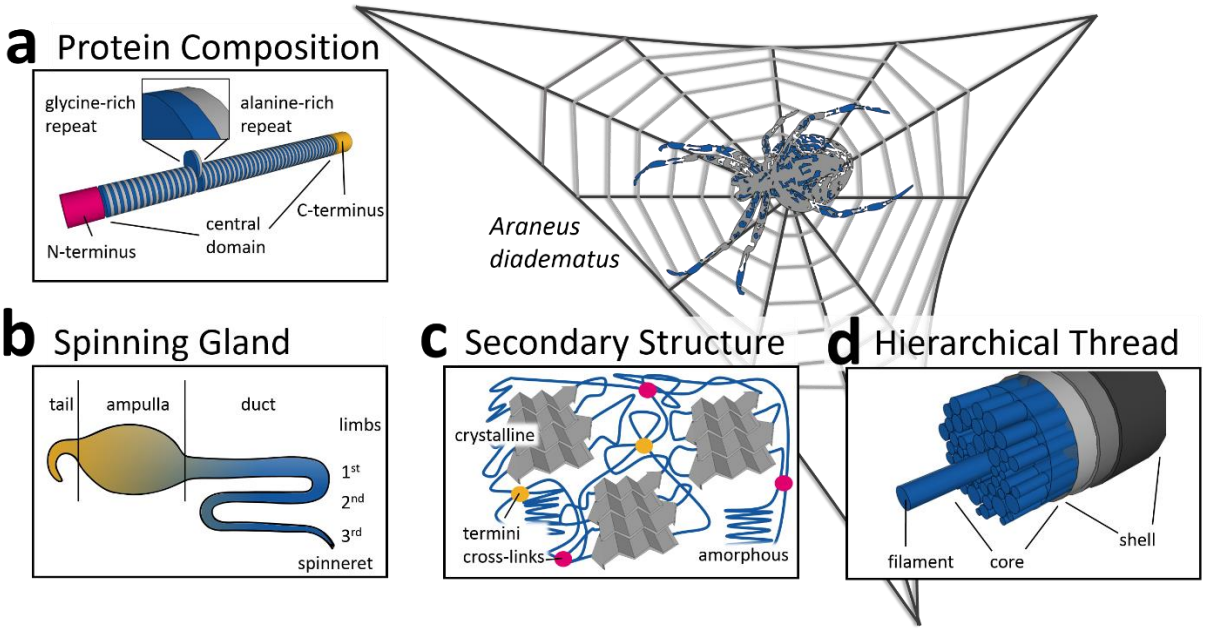

Figure 10| The modular spidroin (**a**) is secreted and spun in the gland (**b**). The spidroin forms a hard/soft composite of secondary structures (**c**) that build up individual filaments, which are the main component comprising the dragline thread (**d**).

Apart from assuring the long-term stability of the spinning solution, the termini also guide protein aggregation during fiber formation.[127] This fiber formation takes place on demand in the spinning duct (Figure 10 b blue region of the gland). Approaching the spinneret and traveling along the duct, the consecutive limbs become increasingly acidic (roughly from pH 7 to 5), water and chaotropic salts are removed from the spinning solution and kosmotropic salts (potassium and phosphate) are added.[120-122] Those conditions induce conformational switches in the C- and N-terminal domains and facilitate spidroin multimerization. As the spinning process is furthermore accompanied by increasing shear stress (especially in the third limb) from the narrowing taper and the spider pulling the thread, molecular alignment and partial crystallization is achieved. Especially the alanine-rich units of the repetitive central domain intertwine to form β-sheet crystallites.

Overall, this process yields the strong (~ 1.1 GPa) yet extensible (~ 27 %) dragline thread from a viscous spinning solution. The main features of the solid spidroin structure in such a thread held

liable for its magnificent mechanical properties are illustrated in Figure 10 c. The terminal domains have guided the formation of a spidroin network, which is cross-linked by hard β-sheet crystallites. Those crystallites are embedded in a soft and rather amorphous matrix, which consists of the glycine-rich units of the central spidroin domain. While the β-sheets mediate the strength, the amorphous matrix contributes elasticity hence forming a tough composite.[119] Overall, the dragline thread exhibits an unmet toughness, which arises from this remarkable balance of strength and extensibility. Even more pronounced than in other materials, water content dictates the mechanical properties of the thread rendering the material stiff in dry conditions and conversely rubber-like in a moist environment.[128, 129]

The thread itself is built up not only from the spidroins but also from further components and in a hierarchical manner. First, the spidroins shape individual filaments of a few hundred nanometers in diameter,[130] all of which are summarized as the thread's core. The core is encased by a shell that mostly fulfills regulatory tasks but also counterbalances pre-stresses present in the structure to additionally improve the mechanical properties.[131, 132]

Recombinant Silk

Unfortunately, spiders cannot be farmed at large scales as is the case for silkworms (silk from *Bombyx mori*) mostly due to the their cannibalistic behavior. An alternative approach is the recombinant production,[133, 134] i.e. the transfer of the genetic blueprint for silk into another host and consecutive spidroin expression.[135] Besides other organisms, *Escherichia Coli* bacteria are especially promising as host as they are easy to ferment and the spidroin can be purified with reasonable effort.[134] The difference in codon usage between eucariotic spiders and procariotic bacteria necessitates reverse protein transcription, which in turn offers the possibility to design customized spidroin sequences.[133, 134] Thus, intentional structural mutations allow for application-specific protein design[136] as well as for fundamental studies on simplified model systems[137] (see also chapter IV.2). Recombinant routes furthermore bear the advantage of silk production ensuring reproducible properties, that – in contrast to reconstituted or forcibly silked silk - do not depend on e.g. spider individual, reeling speed, diet, and other factors. And, beyond the obvious fibrillar morphology, spidroins can also be shaped in other morphologies as films, particles, gels, or foams to exploit the full range of beneficial silk characteristics (e.g. the biocompatibility as mentioned above).[138, 139]

Spider silk is one of nature's most remarkable high-performance materials and more than just its chemical compounds. It is the synergy of spidroins structured by the delicate spinning process into environmentally sensitive fibers. To fully comprehend and eventually mimick silk, we need to gather a thorough understanding on all levels of spider silk, the spidroins themselves, the spinning process, and the role of water in the structure.

II.7 Supramolecular Chemistry of 1,3,5-Benzene- and Cyclohexane-tricarboxamides

Supramolecular chemistry bears the potential to combine its inherent reversibility with hierarchical self-assembly. Prospective smart design on a molecular basis requires a thorough understanding of structure-property relations and is key to tap the full supramolecular potential.

Supramolecular chemistry is chemistry beyond the covalent bond.[140-142] That means structure formation takes place based on reversible, secondary interactions such as hydrogen bonding, metal coordination, van der Waals interactions, and others. If the interaction motifs (e.g. a donor-acceptor sequence of H-bonds) have evolved or are designed sufficiently specific, the way how molecules assemble is predetermined or can be programmed, respectively. This content of information in the molecular structure governs self-organization towards complex matter and is, therefore, ultimately the basis of life.[142] Despite their complexity, biological supramolecular assemblies, for instance the microtubules in cells, can illustrate the advantages of the supramolecular approach such as formation on demand (i.e. in non-equilibrium conditions), mechanical robustness at simultaneous reversibility, and the capability of self-healing.[143, 144]

A first step towards synthetic self-organization are supramolecular polymers.[145] Here, the monomeric building blocks are equipped with complementary and directional secondary interaction moieties. Upon cooling or increase of concentration in a suitable solution medium, the monomers

will interconnect via their non-covalent interactions to form a polymer chain.[146] A well-studied example is the class of 1,3,5-tricarboxamides, namely 1,3,5-benzene- and 1,3,5-cyclohexanetrisamides (BTAs and CTAs) (Figure 11). These molecules commonly consist of a core (benzene or cyclohexane) that is linked via three amide entities (in 1, 3, and 5 position) to peripheral groups of almost arbitrary composition (as evidenced by the multitude of existing compounds[147-149]) (Figure 11 center). One important aspect with respect to practical applications of supramolecules is a reasonably simple synthesis of the monomers. Figure 11a shows the widely employed reaction of the carboxylic acid chloride with the amine carrying the peripheral group to yield the respective 1,3,5-tricarboxamide. This synthesis of one or maximum two steps is sufficiently facile and has proven to be tolerant for a multitude of peripheral groups.[149]

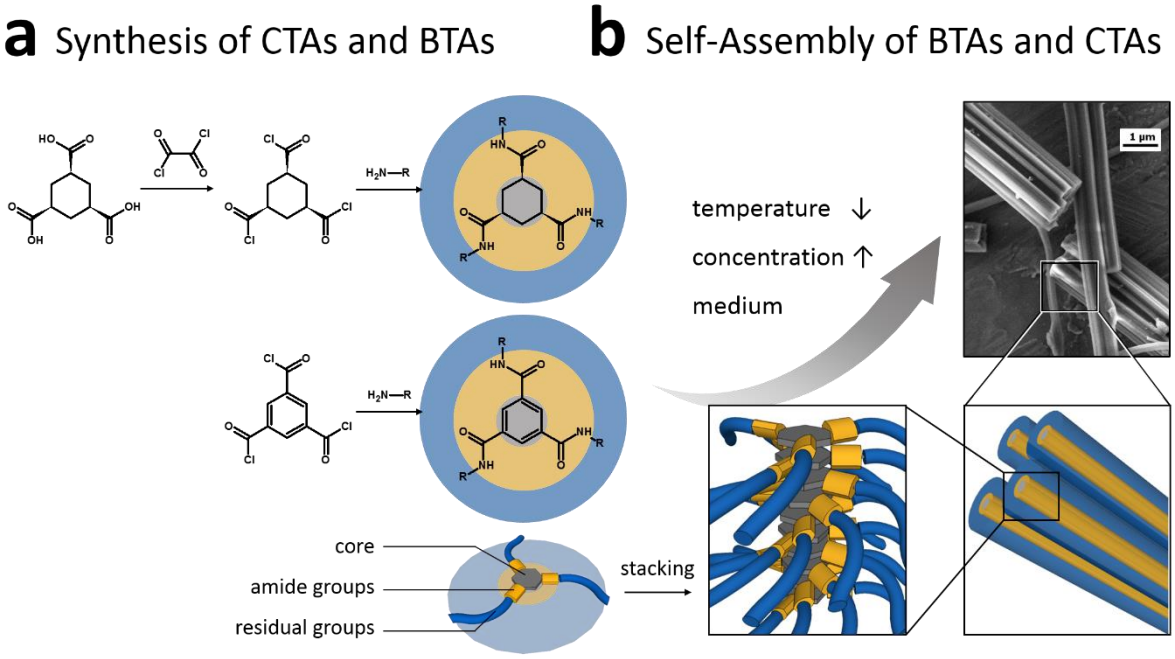

Figure 11| Synthesis and self-assembly of 1,3,5-tricarboxamides. (**a**) Widely used synthesis route of amide bond formation by the reaction of the carboxylic acid chloride and a respective amine. The 1,3,5-tricarboxamides consist of a core (benzene or cyclohexane) enclosed by three amide entities that connect the core to peripheral groups. (**b**) Intermolecular interactions dominated by hydrogen bonding trigger stacking of the discotic BTA and CTA molecules upon cooling or concentration increase. The resulting columns aggregate further to form microscopic fibrillar assemblies.

BTAs and CTAs share the generic capability to form self-complementary building blocks, which facilitate stacking into rod-like assemblies. Of course, the nature of the residual group and the amide connectivity as well as the surrounding solvent have a large influence on the case-specific aggregation and may change the particular assembly pattern. However, a general and representative mechanism is shown in Figure 11b. Initially, in an isolated molecule, the amide entities and the core may assume a co-planar shape. When interacting with a second molecule, the amide entities can rotate out of the plane of the core to adapt the self-complementary configuration that allows 3-fold inter-molecular hydrogen bonding.[150] The angle of rotation is mainly influenced by the core: in BTAs, conjugation with the benzene ring competes with the hydrogen bond formation to yield somewhat tilted amide groups (Figure 11b). In CTAs, contrarily, the rotation is not hindered and the amide groups can adopt an almost perpendicular configuration with the ring plane.[150] In both cases, a net dipole moment emerges within a stack as all hydrogen bonds point towards the same direction, along the stack's long axis.[151-153] As the dipole-dipole interaction is long-ranged, the next docking molecule will experience a higher attraction from a pre-existing stack as compared to another single molecule. Hence, the polymerization happens presumably in a cooperative manner.[146] Furthermore, the macrodipole within one stack needs to be compensated by an antiparallel neighboring stack. This process leads to the formation of the observed liquid crystalline phases and eventually to rod-like nanofibers. These nanofibers have been found to form reversibly upon cooling or evaporation (concentration increase and temperature drop) of their solution.[154] Despite the monomers are only linked by "weak" secondary interactions such as the dominant hydrogen bonding but also π-π-stacking, the cooperativity of those interactions renders the nanofibers surprisingly mechanical stable. In fact, these nanofibers have been found to exhibit a Young's modulus comparable to that of classical covalent polymers.[70, 74] Inclusion of these nanorods in suitable matrices is a promising path towards complex hierarchical composites/copolymers.[155]

With that in mind, the two major reasons fueling the interest in the class of 1,3,5-tricarboxamides become obvious:

(1) BTAs and CTAs combine a simple molecular structure and chemical versatility ideally suited to study the principles of supramolecular assemblies in depth. Systematic synthesis of a multitude of derivatives and the investigation of their respective phase behavior[149] as well as theoretical considerations[153] have shed light on stack formation and properties.

(2) BTAs and CTAs can be readily used for a wide variety of applications illustrating the unique features of supramolecular systems. One example is the fast and well-defined aggregation in nanoscopic crystallites that form upon cooling and aid polymer nucleation.[148] Furthermore, the assembly process to nanofibers in a solution can be used to interweave a carrier nonwoven at unprecedented ease. Such microfiber/nanofiber composites show high potential in filtration applications.[154, 156]

Additionally, BTAs and CTAs have recently been found to provide sufficient intramolecular cohesion to facilitate melt-electrospinning to beads or fibers with µm-diameters.[156, 157] This complementary approach to fiber formation allows for bilateral studying of the supramolecular aggregate formation as well as the spinning process itself.[75]

Overall, detailed understanding of self-assembly in general and the self-assembly of BTAs and CTAs as a model system in particular represents one important step towards realization of structural hierarchy in materials. Where tedious lithographic approaches fail when facing scale-up, self-assembly and self-organization provide a promising pathway. Only when truly comprehending the structure-property relationships, tailored material design can become accomplishable.

II.8 References

1. Gross L. Recent advances in submolecular resolution with scanning probe microscopy. *Nat Chem* 2011, **3**(4)**:** 273-278.

2. de Oteyza DG, Gorman P, Chen YC, Wickenburg S, Riss A, Mowbray DJ*, et al.* Direct Imaging of Covalent Bond Structure in Single-Molecule Chemical Reactions. *Science* 2013, **340**(6139)**:** 1434-1437.

3. Binnig G, Quate CF, Gerber C. Atomic force microscope. *Phys Rev Lett* 1986, **56**(9)**:** 930-933.

4. Eaton P, West P. *Atomic Force Microscopy*. Oxford University Press: New York, 2010.

5. Giessibl FJ. Advances in atomic force microscopy. *Rev Mod Phys* 2003, **75**(3)**:** 949-983.

6. Garcia R, Perez R. Dynamic atomic force microscopy methods. *Surf Sci Rep* 2002, **47**(6-8)**:** 197-301.

7. Zhong J, Yan J. Seeing is believing: atomic force microscopy imaging for nanomaterial research. *Rsc Advances* 2016, **6**(2)**:** 1103-1121.

8. Berger R, Butt HJ, Retschke MB, Weber SAL. Electrical Modes in Scanning Probe Microscopy. *Macromol Rapid Commun* 2009, **30**(14)**:** 1167-1178.

9. Proksch R, Schaffer TE, Cleveland JP, Callahan RC, Viani MB. Finite optical spot size and position corrections in thermal spring constant calibration. *Nanotechnology* 2004, **15**(9)**:** 1344-1350.

10. Cleveland JP, Manne S, Bocek D, Hansma PK. A Nondestructive Method for Determining the Spring Constant of Cantilevers for Scanning Force Microscopy. *Rev Sci Instrum* 1993, **64**(2)**:** 403-405.

11. Hutter JL, Bechhoefer J. Calibration of atomic-force microscope tips. *Rev Sci Instrum* 1993, **64**(7)**:** 1868-1873.

12. Sader JE, Chon JWM, Mulvaney P. Calibration of rectangular atomic force microscope cantilevers. *Rev Sci Instrum* 1999, **70**(10)**:** 3967-3969.

13. Munz M. Force calibration in lateral force microscopy: a review of the experimental methods. *J Phys D-Appl Phys* 2010, **43**(6)**:** 063001.

14. Green CP, Lioe H, Cleveland JP, Proksch R, Mulvaney P, Sader JE. Normal and torsional spring constants of atomic force microscope cantilevers. *Rev Sci Instrum* 2004, **75**(6)**:** 1988-1996.

15. Quantitative mechanical property mapping at the nanoscale with PeakForce QNM. [cited March 2016]Available from: https://www.bruker.com/fileadmin/user_upload/8-PDF-Docs/SurfaceAnalysis/AFM/ApplicationNotes/AN128-RevB0-Quantitative_Mechanical_Property_Mapping_at_the_Nanoscale_with_PeakForceQNMAppNote.pdf

16. Sweers K, van der Werf K, Bennink M, Subramaniam V. Nanomechanical properties of alpha-synuclein amyloid fibrils: a comparative study by nanoindentation, harmonic force microscopy, and Peakforce QNM. *Nanoscale Res Lett* 2011, **6:** 10.

17. Butt HJ, Cappella B, Kappl M. Force measurements with the atomic force microscope: Technique, interpretation and applications. *Surf Sci Rep* 2005, **59**(1-6)**:** 1-152.

18. Cappella B, Dietler G. Force-distance curves by atomic force microscopy. *Surf Sci Rep* 1999, **34**(1-3)**:** 1-104.

19. Dunlop JWC, Fratzl P. Biological Composites. In: Clarke DR, Ruhle M, Zok F (eds). *Annual Review of Materials Research*, vol. 40, 2010, pp 1-24.

20. De Volder MFL, Tawfick SH, Baughman RH, Hart AJ. Carbon Nanotubes: Present and Future Commercial Applications. *Science* 2013, **339**(6119)**:** 535-539.

21. Arinstein A, Zussman E. Electrospun Polymer Nanofibers: Mechanical and Thermodynamic Perspectives. *J Polym Sci Pt B-Polym Phys* 2011, **49**(10)**:** 691-707.

22. Sun CQ. Thermo-mechanical behavior of low-dimensional systems: The local bond average approach. *Prog Mater Sci* 2009, **54**(2)**:** 179-307.

23. Zheng XP, Cao YP, Li B, Feng XQ, Wang GF. Surface effects in various bending-based test methods for measuring the elastic property of nanowires. *Nanotechnology* 2010, **21**(20)**:** 6.

24. Chew SY, Hufnagel TC, Lim CT, Leong KW. Mechanical properties of single electrospun drug-encapsulated nanofibres. *Nanotechnology* 2006, **17**(15)**:** 3880-3891.

25. Vasiliev VV, Morozov E. *Advanced Mechanics of Composite Materials*, 3rd edn, vol. 3, 2013.

26. Continuous Dynamic Analysis and Quasi-Static Measurement of Spider Silks. [cited March 2016]Available from: http://cp.literature.agilent.com/litweb/pdf/5990-4325EN.pdf

27. Keysight T150 UTM Universal Testing Machine. [cited March 2016]Available from: http://literature.cdn.keysight.com/litweb/pdf/5990-4206EN.pdf

28. Madsen B, Shao ZZ, Vollrath F. Variability in the mechanical properties of spider silks on three levels: interspecific, intraspecific and intraindividual. *Int J Biol Macromol* 1999, **24**(2–3)**:** 301-306.

29. Swanson BO, Blackledge TA, Beltran J, Hayashi CY. Variation in the material properties of spider dragline silk across species. *Appl Phys A-Mater Sci Process* 2006, **82**(2)**:** 213-218.

30. Work RW. Dimensions, Birefringences, and Force-Elongation Behavior of Major and Minor Ampullate Silk Fibers from Orb-Web-Spinning Spiders - Effects of Wetting on These Properties. *Text Res J* 1977, **47**(10)**:** 650-662.

31. Bazbouz MB, Stylios GK. The Tensile Properties of Electrospun Nylon 6 Single Nanofibers. *J Polym Sci Pt B-Polym Phys* 2010, **48**(15)**:** 1719-1731.

32. Brown TD, Slotosch A, Thibaudeau L, Taubenberger A, Loessner D, Vaquette C*, et al.* Design and Fabrication of Tubular Scaffolds via Direct Writing in a Melt Electrospinning Mode. *Biointerphases* 2012, **7**(1-4)**:** 16.

33. Chen F, Peng XW, Li TT, Chen SL, Wu XF, Reneker DH*, et al.* Mechanical characterization of single high-strength electrospun polyimide nanofibres. *J Phys D-Appl Phys* 2008, **41**(2)**:** 025308.

34. Ryuji I, Masaya K, Seeram R. Structure and properties of electrospun PLLA single nanofibres. *Nanotechnology* 2005, **16**(2)**:** 208.

35. Park SJ, Chase GG, Jeong KU, Kim HY. Mechanical properties of titania nanofiber mats fabricated by electrospinning of sol-gel precursor. *J Sol-Gel Sci Techn* 2010, **54**(2)**:** 188-194.

36. Yu MF, Lourie O, Dyer MJ, Moloni K, Kelly TF, Ruoff RS. Strength and breaking mechanism of multiwalled carbon nanotubes under tensile load. *Science* 2000, **287**(5453)**:** 637-640.

37. Kaplan-Ashiri I, Cohen SR, Gartsman K, Rosentsveig R, Seifert G, Tenne R. Mechanical behavior of individual WS2 nanotubes. *J Mater Res* 2004, **19**(2)**:** 454-459.

38. Marszalek PE, Greenleaf WJ, Li HB, Oberhauser AF, Fernandez JM. Atomic force microscopy captures quantized plastic deformation in gold nanowires. *Proc Natl Acad Sci U S A* 2000, **97**(12)**:** 6282-6286.

39. Rubio-Bollinger G, Bahn SR, Agrait N, Jacobsen KW, Vieira S. Mechanical properties and formation mechanisms of a wire of single gold atoms. *Phys Rev Lett* 2001, **87**(2)**:** 4.

40. Hang F, Lu D, Bailey RJ, Jimenez-Palomar I, Stachewicz U, Cortes-Ballesteros B*, et al.* In situ tensile testing of nanofibers by combining atomic force microscopy and scanning electron microscopy. *Nanotechnology* 2011, **22**(36)**:** 365708.

41. Tan EPS, Goh CN, Sow CH, Lim CT. Tensile test of a single nanofiber using an atomic force microscope tip. *Appl Phys Lett* 2005, **86**(7)**:** 073115.

42. Tan EPS, Lim CT. Novel approach to tensile testing of micro- and nanoscale fibers. *Rev Sci Instrum* 2004, **75**(8)**:** 2581-2585.

43. Graham JS, Vomund AN, Phillips CL, Grandbois M. Structural changes in human type I collagen fibrils investigated by force spectroscopy. *Exp Cell Res* 2004, **299**(2)**:** 335-342.

44. Hang F, Barber AH. Nano-mechanical properties of individual mineralized collagen fibrils from bone tissue. *J R Soc Interface* 2011, **8**(57)**:** 500-505.

45. van der Rijt JAJ, van der Werf KO, Bennink ML, Dijkstra PJ, Feijen J. Micromechanical testing of individual collagen fibrils. *Macromol Biosci* 2006, **6**(9)**:** 697-702.

46. Svensson RB, Hassenkam T, Hansen P, Magnusson SP. Viscoelastic behavior of discrete human collagen fibrils. *J Mech Behav Biomed* 2010, **3**(1)**:** 112-115.

47. Svensson RB, Mulder H, Kovanen V, Magnusson SP. Fracture Mechanics of Collagen Fibrils: Influence of Natural Cross-Links. *Biophys J* 2013, **104**(11)**:** 2476-2484.

48. Barber AH, Lu D, Pugno NM. Extreme strength observed in limpet teeth. *J R Soc Interface* 2015, **12**(105)**:** 6.

49. Demczyk BG, Wang YM, Cumings J, Hetman M, Han W, Zettl A*, et al.* Direct mechanical measurement of the tensile strength and elastic modulus of multiwalled carbon nanotubes. *Mater Sci Eng A-Struct Mater Prop Microstruct Process* 2002, **334**(1-2)**:** 173-178.

50. Eppell SJ, Smith BN, Kahn H, Ballarini R. Nano measurements with micro-devices: mechanical properties of hydrated collagen fibrils. *J R Soc Interface* 2006, **3**(6)**:** 117-121.

51. Haque MA, Saif MTA. A review of MEMS-based microscale and nanoscale tensile and bending testing. *Exp Mech* 2003, **43**(3)**:** 248-255.

52. Jaeger D, Schischka J, Bagdahn J, Jaeger R. Tensile testing of individual ultrathin electrospun poly(L-lactic acid) fibers. *J Appl Polym Sci* 2009, **114**(6)**:** 3774-3779.

53. Naraghi M, Chasiotis I, Kahn H, Wen Y, Dzenis Y. Novel method for mechanical characterization of polymeric nanofibers. *Rev Sci Instrum* 2007, **78**(8)**:** 7.

54. Samuel BA, Haque MA, Yi B, Rajagopalan R, Foley HC. Mechanical testing of pyrolysed poly-furfuryl alcohol nanofibres. *Nanotechnology* 2007, **18**(11)**:** 8.

55. Zhu Y, Chang T-H. A review of microelectromechanical systems for nanoscale mechanical characterization. *J Micromech Microeng* 2015, **25**(9)**:** 093001.

56. Guo Q, Landau P, Hosemann P, Wang YQ, Greer JR. Helium Implantation Effects on the Compressive Response of Cu Nanopillars. *Small* 2013, **9**(5)**:** 691-696.

57. Magagnosc DJ, Ehrbar R, Kumar G, He MR, Schroers J, Gianola DS. Tunable Tensile Ductility in Metallic Glasses. *Scientific Reports* 2013, **3:** 1096.

58. Tombler TW, Zhou CW, Alexseyev L, Kong J, Dai HJ, Lei L*, et al.* Reversible electromechanical characteristics of carbon nanotubes under local-probe manipulation. *Nature* 2000, **405**(6788)**:** 769-772.

59. Salvetat JP, Briggs GAD, Bonard JM, Bacsa RR, Kulik AJ, Stockli T*, et al.* Elastic and shear moduli of single-walled carbon nanotube ropes. *Phys Rev Lett* 1999, **82**(5)**:** 944-947.

60. Wu B, Heidelberg A, Boland JJ. Mechanical properties of ultrahigh-strength gold nanowires. *Nat Mater* 2005, **4**(7)**:** 525-529.

61. Carlisle CR, Coulais C, Namboothiry M, Carroll DL, Hantgan RR, Guthold M. The mechanical properties of individual, electrospun fibrinogen fibers. *Biomaterials* 2009, **30**(6)**:** 1205-1213.

62. Almecija D, Blond D, Sader JE, Coleman JN, Boland JJ. Mechanical properties of individual electrospun polymer-nanotube composite nanofibers. *Carbon* 2009, **47**(9)**:** 2253-2258.

63. Liu W, Jawerth LM, Sparks EA, Falvo MR, Hantgan RR, Superfine R*, et al.* Fibrin fibers have extraordinary extensibility and elasticity. *Science* 2006, **313**(5787)**:** 634-634.

64. Yang L, Fitié CFC, van der Werf KO, Bennink ML, Dijkstra PJ, Feijen J. Mechanical properties of single electrospun collagen type I fibers. *Biomaterials* 2008, **29**(8)**:** 955-962.

65. Yang L, Van der Werf KO, Fitie CFC, Bennink ML, Dijkstra PJ, Feijen J. Mechanical properties of native and cross-linked type I collagen fibrils. *Biophys J* 2008, **94**(6)**:** 2204-2211.

66. Wang W, Barber AH. Measurement of size-dependent glass transition temperature in electrospun polymer fibers using AFM nanomechanical testing. *J Polym Sci Pt B-Polym Phys* 2012, **50**(8)**:** 546-551.

67. Gestos A, Whitten PG, Wallace GG, Spinks GM. Actuating individual electrospun hydrogel nanofibres. *Soft Matter* 2012, **8**(31)**:** 8082-8087.

68. McCarthy EK, Bellew AT, Sader JE, Boland JJ. Poisson's ratio of individual metal nanowires. *Nat Commun* 2014, **5:** 4336.

69. Minot ED, Yaish Y, Sazonova V, Park JY, Brink M, McEuen PL. Tuning carbon nanotube band gaps with strain. *Phys Rev Lett* 2003, **90**(15)**:** 156401.

70. Kluge D, Singer JC, Neubauer JW, Abraham F, Schmidt HW, Fery A. Influence of the Molecular Structure and Morphology of Self-Assembled 1,3,5-Benzenetrisamide Nanofibers on their Mechanical Properties. *Small* 2012, **8**(16)**:** 2563-2570.

71. Heidelberg A, Ngo LT, Wu B, Phillips MA, Sharma S, Kamins TI*, et al.* A generalized description of the elastic properties of nanowires. *Nano Lett* 2006, **6**(6)**:** 1101-1106.

72. Calahorra Y, Shtempluck O, Kotchetkov V, Yaish YE. Young's Modulus, Residual Stress, and Crystal Orientation of Doubly Clamped Silicon Nanowire Beams. *Nano Lett* 2015, **15**(5)**:** 2945-2950.

73. Gere JM, Timoshenko SP. *Mechanics of Materials*, 3rd edn. Chapman & Hall: London, 1991, p 692.

74. Kluge D, Abraham F, Schmidt S, Schmidt H-W, Fery A. Nanomechanical Properties of Supramolecular Self-Assembled Whiskers Determined by AFM Force Mapping. *Langmuir* 2010, **26**(5)**:** 3020-3023.

75. Kluge D, Singer JC, Neugirg BR, Neubauer JW, Schmidt HW, Fery A. Top-down meets bottom-up: A comparison of the mechanical properties of melt electrospun and self-assembled 1,3,5-benzenetrisamide fibers. *Polymer* 2012, **53**(25)**:** 5754-5759.

76. Tanur AE, Wang J, Reddy ALM, Lamont DN, Yap YK, Walker GC. Diameter-Dependent Bending Modulus of Individual Multiwall Boron Nitride Nanotubes. *J Phys Chem B* 2013, **117**(16)**:** 4618-4625.

77. Chen YX, Dorgan BL, McIlroy DN, Aston DE. On the importance of boundary conditions on nanomechanical bending behavior and elastic modulus determination of silver nanowires. *J Appl Phys* 2006, **100**(10)**:** 104301.

78. Cronin-Golomb M, Sahin O. High-resolution nanomechanical analysis of suspended electrospun silk fibers with the torsional harmonic atomic force microscope. *Beilstein J Nanotechnol* 2013, **4:** 243-248.

79. Ling XY, Phang IY, Schonherr H, Reinhoudt DN, Vancso GJ, Huskens J. Freestanding 3D Supramolecular Particle Bridges: Fabrication and Mechanical Behavior. *Small* 2009, **5**(12)**:** 1428-1435.

80. Chen YX, Stevenson I, Pouy R, Wang LD, McIlroy DN, Pounds T*, et al.* Mechanical elasticity of vapour-liquid-solid grown GaN nanowires. *Nanotechnology* 2007, **18**(13).

81. Iwamoto S, Kai W, Isogai A, Iwata T. Elastic Modulus of Single Cellulose Microfibrils from Tunicate Measured by Atomic Force Microscopy. *Biomacromolecules* 2009, **10**(9)**:** 2571-2576.

82. Stachewicz U, Bailey RJ, Wang W, Barber AH. Size dependent mechanical properties of electrospun polymer fibers from a composite structure. *Polymer* 2012, **53**(22)**:** 5132-5137.

83. Tao XY, Dong LX, Wang XN, Zhang WK, Nelson BJ, Li XD. B4C-Nanowires/Carbon-Microfiber Hybrid Structures and Composites from Cotton T-shirts. *Adv Mater* 2010, **22**(18)**:** 2055–2059.

84. Hudson SD, Zhurov V, Grbic V, Grbic M, Hutter JL. Measurement of the elastic modulus of spider mite silk fibers using atomic force microscopy. *J Appl Phys* 2013, **113**(15)**:** 154307.

85. Xiong Q, Duarte N, Tadigadapa S, Eklund PC. Force-Deflection Spectroscopy: A New Method to Determine the Young's Modulus of Nanofilaments. *Nano Lett* 2006, **6**(9)**:** 1904-1909.

86. Celik E, Guven I, Madenci E. Mechanical characterization of nickel nanowires by using a customized atomic force microscope. *Nanotechnology* 2011, **22**(15)**:** 155702.

87. Ngo LT, Almecija D, Sader JE, Daly B, Petkov N, Holmes JD*, et al.* Ultimate-strength germanium nanowires. *Nano Lett* 2006, **6**(12)**:** 2964-2968.

88. Wen BM, Sader JE, Boland JJ. Mechanical Properties of ZnO Nanowires. *Phys Rev Lett* 2008, **101**(17)**:** 175502.

89. Wu B, Heidelberg A, Boland JJ, Sader JE, Sun XM, Li YD. Microstructure-hardened silver nanowires. *Nano Lett* 2006, **6**(3)**:** 468-472.

90. Yaish YE, Calahorra Y, Shtempluck O, Kotchetkov V. Three-point bending analysis of doubly clamped silicon nanowire beams; Young's modulus, initial stress, and crystal orientation. *J Appl Phys* 2015, **117**(16)**:** 164311.

91. Schniepp HC, Koebley SR, Vollrath F. Brown Recluse Spider's Nanometer Scale Ribbons of Stiff Extensible Silk. *Adv Mater* 2013, **25**(48)**:** 7028-7032.

92. Gestos A, Whitten PG, Spinks GM, Wallace GG. Tensile testing of individual glassy, rubbery and hydrogel electrospun polymer nanofibres to high strain using the atomic force microscope. *Polym Test* 2013, **32**(4)**:** 655-664.

93. Liu W, Carlisle CR, Sparks EA, Guthold M. The mechanical properties of single fibrin fibers. *J Thromb Haemost* 2010, **8**(5)**:** 1030-1036.

94. Carlisle CR, Coulais C, Guthold M. The mechanical stress-strain properties of single electrospun collagen type I nanofibers. *Acta Biomater* 2010, **6**(8)**:** 2997-3003.

95. Briscoe W. Surface Forces. In: Cosgrove T (ed). *Colloid Science Principles, methods and applications*. John Wiley & Sons Ltd: Chippenham, 2010, pp 329 - 362.

96. Tadros TF. *Interfacial Phenomena and Colloid Stability: Industrial Applications*. Gruyter, de Oldenbourg, 2015.

97. Hermansson M. The DLVO theory in microbial adhesion. *Colloids and Surfaces B-Biointerfaces* 1999, **14**(1-4)**:** 105-119.

98. Israelachvili JN, Adams GE. Measurement of forces between 2 mica surfaces in aqueous-electrolyte solutions in range 0-100 nm. *Journal of the Chemical Society-Faraday Transactions I* 1978, **74:** 975-1001.

99. Israelachvili JN. Intermolecular and surface forces. 3rd ed. Amsterdam: Elsevier; 2011.

100. Ducker WA, Senden TJ, Pashley RM. Direct measurement of colloidal forces using an atomic force microscope. *Nature* 1991, **353**(6341)**:** 239-241.

101. Butt HJ, Berger R, Bonaccurso E, Chen Y, Wang J. Impact of atomic force microscopy on interface and colloid science. *Adv Colloid Interfac* 2007, **133**(2)**:** 91-104.

102. Ninham BW. On progress in forces since the DLVO theory. *Adv Colloid Interfac* 1999, **83**(1-3)**:** 1-17.

103. Agarwal S, Greiner A, Wendorff JH. Functional materials by electrospinning of polymers. *Prog Polym Sci* 2013, **38**(6)**:** 963-991.

104. Greiner A, Wendorff JH. Electrospinning: A fascinating method for the preparation of ultrathin fibers. *Angew Chem-Int Edit* 2007, **46**(30)**:** 5670-5703.

105. Bhardwaj N, Kundu SC. Electrospinning: A fascinating fiber fabrication technique. *Biotechnol Adv* 2010, **28**(3)**:** 325-347.

106. Luo CJ, Stoyanov SD, Stride E, Pelan E, Edirisinghe M. Electrospinning versus fibre production methods: from specifics to technological convergence. *Chem Soc Rev* 2012, **41**(13)**:** 4708-4735.

107. Singer JC, Giesa R, Schmidt H-W. Shaping self-assembling small molecules into fibres by melt electrospinning. *Soft Matter* 2012, **8**(39)**:** 9972-9976.

108. Taylor G. Disintegration of Water Drops in an Electric Field. *P Roy Soc Lond A Mat* 1964, **280**(1380)**:** 383-397.

109. Reneker DH, Yarin AL, Zussman E, Xu H. Electrospinning of nanofibers from polymer solutions and melts. In: Aref H, VanDerGiessen E (eds). *Advances in Applied Mechanics*, vol. 41. Elsevier Academic Press Inc: San Diego, 2007, pp 43-195.

110. Reneker DH, Yarin AL. Electrospinning jets and polymer nanofibers. *Polymer* 2008, **49**(10)**:** 2387-2425.

111. Agarwal S, Greiner A, Wendorff JH. Electrospinning of Manmade and Biopolymer Nanofibers-Progress in Techniques, Materials, and Applications. *Adv Funct Mater* 2009, **19**(18)**:** 2863-2879.

112. Lahann J. Recent Progress in Nano-biotechnology: Compartmentalized Micro- and Nanoparticles via Electrohydrodynamic Co-jetting. *Small* 2011, **7**(9)**:** 1149-1156.

113. McCann JT, Li D, Xia YN. Electrospinning of nanofibers with core-sheath, hollow, or porous structures. *J Mater Chem* 2005, **15**(7)**:** 735-738.

114. Agarwal S, Wendorff JH, Greiner A. Use of electrospinning technique for biomedical applications. *Polymer* 2008, **49**(26)**:** 5603-5621.

115. Hassiba AJ, El Zowalaty ME, Nasrallah GK, Webster TJ, Luyt AS, Abdullah AM*, et al.* Review of recent research on biomedical applications of electrospun polymer nanofibers for improved wound healing. *Nanomedicine* 2016, **11**(6)**:** 715-737.

116. Barhate RS, Ramakrishna S. Nanofibrous filtering media: Filtration problems and solutions from tiny materials. *J Membr Sci* 2007, **296**(1-2)**:** 1-8.

117. Zucchelli A, Focarete ML, Gualandi C, Ramakrishna S. Electrospun nanofibers for enhancing structural performance of composite materials. *Polym Advan Technol* 2011, **22**(3)**:** 339-349.

118. Richard-Lacroix M, Pellerin C. Molecular Orientation in Electrospun Fibers: From Mats to Single Fibers. *Macromolecules* 2013, **46**(24)**:** 9473-9493.

119. Gosline JM, Guerette PA, Ortlepp CS, Savage KN. The mechanical design of spider silks: From fibroin sequence to mechanical function. *J Exp Biol* 1999, **202**(23)**:** 3295-3303.

120. Heim M, Keerl D, Scheibel T. Spider Silk: From Soluble Protein to Extraordinary Fiber. *Angew Chem-Int Edit* 2009, **48**(20)**:** 3584-3596.

121. Vollrath F, Knight DP. Liquid crystalline spinning of spider silk. *Nature* 2001, **410**(6828)**:** 541-548.

122. Rising A, Johansson J. Toward spinning artificial spider silk. *Nat Chem Biol* 2015, **11**(5)**:** 309-315.

123. Allmeling C, Jokuszies A, Reimers K, Kall S, Vogt PM. Use of spider silk fibres as an innovative material in a biocompatible artificial nerve conduit. *J Cell Mol Med* 2006, **10**(3)**:** 770-777.

124. Guinea GV, Elices M, Perez-Rigueiro J, Plaza G. Self-tightening of spider silk fibers induced by moisture. *Polymer* 2003, **44**(19)**:** 5785-5788.

125. Emile O, Le Floch A, Vollrath F. Biopolymers: Shape memory in spider draglines. *Nature* 2006, **440**(7084)**:** 621-621.

126. Eisoldt L, Smith A, Scheibel T. Decoding the secrets of spider silk. *Mater Today* 2011, **14**(3)**:** 80-86.

127. Humenik M, Scheibel T, Smith A. Spider Silk: Understanding the Structure–Function Relationship of a Natural Fiber. In: Stefan H (ed). *Progress in Molecular Biology and Translational Science*, vol. 103. Academic Press, 2011, pp 131-185.

128. Gosline JM, Denny MW, Demont ME. Spider silk as rubber. *Nature* 1984, **309**(5968)**:** 551-552.

129. Plaza GR, Guinea GV, Perez-Rigueiro J, Elices M. Thermo-hygro-mechanical behavior of spider dragline silk: Glassy and rubbery states. *J Polym Sci Pt B-Polym Phys* 2006, **44**(6)**:** 994-999.

130. Porter D, Vollrath F. Silk as a Biomimetic Ideal for Structural Polymers. *Adv Mater* 2009, **21**(4)**:** 487-492.

131. Papadopoulos P, Sölter J, Kremer F. Hierarchies in the structural organization of spider silk—a quantitative model. *Colloid Polym Sci* 2009, **287**(2)**:** 231-236.

132. Papadopoulos P, Solter J, Kremer F. Structure-property relationships in major ampullate spider silk as deduced from polarized FTIR spectroscopy. *Eur Phys J E* 2007, **24**(2)**:** 193-199.

133. Heidebrecht A, Scheibel T. Recombinant Production of Spider Silk Proteins. In: Sariaslani S, Gadd GM (eds). *Advances in Applied Microbiology*, vol. 82. Elsevier Academic Press Inc: San Diego, 2013, pp 115-153.

134. Vendrely C, Scheibel T. Biotechnological Production of Spider-Silk Proteins Enables New Applications. *Macromol Biosci* 2007, **7**(4)**:** 401-409.

135. Tokareva O, Michalczechen-Lacerda VA, Rech EL, Kaplan DL. Recombinant DNA production of spider silk proteins. *Microbial Biotechnology* 2013, **6**(6)**:** 651-663.

136. Spiess K, Wohlrab S, Scheibel T. Structural characterization and functionalization of engineered spider silk films. *Soft Matter* 2010, **6**(17)**:** 4168-4174.

137. Heidebrecht A, Eisoldt L, Diehl J, Schmidt A, Geffers M, Lang G*, et al.* Biomimetic Fibers Made of Recombinant Spidroins with the Same Toughness as Natural Spider Silk. *Adv Mater* 2015, **27**(13)**:** 2189-2194.

138. Spiess K, Lammel A, Scheibel T. Recombinant Spider Silk Proteins for Applications in Biomaterials. *Macromolecular Bioscience* 2010, **10**(9)**:** 998-1007.

139. Doblhofer E, Heidebrecht A, Scheibel T. To spin or not to spin: spider silk fibers and more. *Appl Microbiol Biot* 2015, **99**(22)**:** 9361-9380.

140. Bosman AW, Sijbesma RP, Meijer EW. Supramolecular polymers at work. *Mater Today* 2004, **7**(4)**:** 34-39.

141. Whitesides GM, Boncheva M. Beyond molecules: Self-assembly of mesoscopic and macroscopic components. *Proc Natl Acad Sci U S A* 2002, **99**(8)**:** 4769-4774.

142. Lehn JM. Toward complex matter: Supramolecular chemistry and self-organization. *Proc Natl Acad Sci U S A* 2002, **99**(8)**:** 4763-4768.

143. Desai A, Mitchison TJ. Microtubule polymerization dynamics. *Annu Rev Cell Dev Bi* 1997, **13:** 83-117.

144. Mulder BM, Janson ME. Biological filaments: Self-healing microtubules. *Nat Mater* 2015, **14**(11)**:** 1080-1081.

145. de Greef TFA, Meijer EW. Materials science: Supramolecular polymers. *Nature* 2008, **453**(7192)**:** 171-173.

146. Kulkarni C, Balasubramanian S, George SJ. What Molecular Features Govern the Mechanism of Supramolecular Polymerization? *Chemphyschem* 2013, **14**(4)**:** 661-673.

147. Cantekin S, de Greef TFA, Palmans ARA. Benzene-1,3,5-tricarboxamide: a versatile ordering moiety for supramolecular chemistry. *Chem Soc Rev* 2012, **41**(18)**:** 6125-6137.

148. Blomenhofer M, Ganzleben S, Hanft D, Schmidt H-W, Kristiansen M, Smith P*, et al.* "Designer" Nucleating Agents for Polypropylene. *Macromolecules* 2005, **38**(9)**:** 3688-3695.

149. Timme A, Kress R, Albuquerque RQ, Schmidt HW. Phase Behavior and Mesophase Structures of 1,3,5-Benzene- and 1,3,5-Cyclohexanetricarboxamides: Towards an Understanding of the Losing Order at the Transition into the Isotropic Phase. *Chem-Eur J* 2012, **18**(27)**:** 8329-8339.

150. Lightfoot MP, Mair FS, Pritchard RG, Warren JE. New supramolecular packing motifs: pi-stacked rods encased in triply-helical hydrogen bonded amide strands. *Chem Commun* 1999(19)**:** 1945-1946.

151. Sakamoto A, Ogata D, Shikata T, Urakawa O, Hanabusa K. Large macro-dipoles generated in a supramolecular polymer of N,N ',N ''-tris(3,7-dimethyloctyl) benzene-1,3,5-tricarboxamide in n-decane. *Polymer* 2006, **47**(4)**:** 956-960.

152. Fitie CFC, Roelofs WSC, Kemerink M, Sijbesma RP. Remnant Polarization in Thin Films from a Columnar Liquid Crystal. *J Am Chem Soc* 2010, **132**(20)**:** 6892-6893.

153. Albuquerque RQ, Timme A, Kress R, Senker J, Schmidt HW. Theoretical Investigation of Macrodipoles in Supramolecular Columnar Stackings. *Chem-Eur J* 2013, **19**(5)**:** 1647-1657.

154. Misslitz H, Kreger K, Schmidt HW. Supramolecular Nanofiber Webs in Nonwoven Scaffolds as Potential Filter Media. *Small* 2013, **9**(12)**:** 2053-2058.

155. Roosma J, Mes T, Leclère P, Palmans ARA, Meijer EW. Supramolecular Materials from Benzene-1,3,5-tricarboxamide-Based Nanorods. *J Am Chem Soc* 2008, **130**(4)**:** 1120-1121.

156. Weiss D, Skrybeck D, Misslitz H, Nardini D, Kern A, Kreger K*, et al.* Tailoring Supramolecular Nanofibers for Air Filtration Applications. *ACS Appl Mater Interfaces* 2016, **8**(23)**:** 14885-14892.

157. Singer JC, Ringk A, Giesa R, Schmidt H-W. Melt Electrospinning of Small Molecules. *Macromolecular Materials and Engineering* 2015, **300**(3)**:** 259-276.

III. Synopsis

“Sie dürfen nicht alles glauben, was Sie denken”

Heinz Erhardt

III.1 Outline

After the motivation for this work (part I) and the introduction of the fundamentals (part II), on which this thesis is built, part IV will give the experimental findings and their interpretation. That part is divided in three individual publications (chapters IV.1 through IV.3), that each contribute to the methodical advancement of AFM as a tool for fiber characterization as well as to a deeper understanding of the respectively considered fibrillar system.
The present part III gives short summaries of these three publications and elucidates their role in the superordinate theme of this thesis.

III.2 Tensile versus AFM Testing of Electrospun PVA Nanofibers: Bridging the Gap from Microscale to Nanoscale

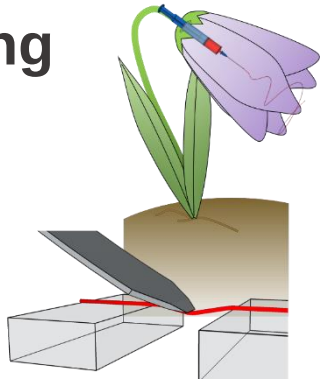

The major impact of this publication is the establishment of both, AFM-based three-point deformation tests and classical high-resolution tensile testing as mutually benchmarked approaches for the mechanical testing of individual (nano-)fibers.

Mechanical testing of individual nanofibers is not trivial. Their small size critically limits their handling as well as the actual testing. Fibers of nanoscale diameter can hardly be detected by the naked eye, only from their slight shimmering when observed against a light source, i.e. from their diffraction of light. Additionally, these fibers are prone to rupture during handling. Fluctuations in the motions of the experimentalist can easily overcome the force and deformation limits, and thus rupture such fibers. Finally, there is only a very limited number of setups that can resolve the forces and deformations during nanofiber testing and such experiments are far from being standardized.

To still face the task of single fiber mechanical characterization, efforts using special high-resolution tensile testing machines as well as AFM-based three-point deformation experiments have been made throughout the literature. A priori, it is not clear whether both approaches will give similar results, that allow an immediate comparison of the absolute values of mechanical properties. The deformation geometry and the raw data evaluation strongly differ and in either of the two techniques, the exact deformations cannot be observed in-situ. Studies on poly(ε-caprolactone) fibers, for instance, report Young's moduli values that differ up to a factor of 60 and it remains questionable whether this discrepancy is caused by the different testing methods themselves or by possible alterations in the respective fiber preparation routes.

Chapter IV.1 addresses this issue of methodical conformity for the well-characterized system of electrospun polyvinyl alcohol (PVA) fibers. Identically prepared fibers were tested by high-resolution tensile testing as well as AFM-based three-point testing. Excluding potential variations in the fiber preparation process, both testing techniques can be thoroughly compared for nanofibers of different diameters and intricacies inherent in the respective method can be spotted. This comparison can be used to benchmark those two commonly applied methods mutually against each other.

Figure 12 gives the diameter dependence of the Young's moduli for PVA nanofibers as determined by AFM-based three-point deformation testing and tensile testing (adapted from chapter IV.1). In essence, this figure also answers the question of methodical conformity of both approaches with yes: as indicated by the gray line, the respective results coincide on a master curve. Still this comparison reveals that there seem to be influences rendering the AFM results systematically higher than the tensile testing results. This may be attributed mainly to the different lengths of the specimen for the respective methods as well as the diverging means by which the fiber cross-sections are determined. The overall consistency, however, provides a thorough basis that ensures the comparability between the various studies and successfully vindicates the interchangeable application of both methods.

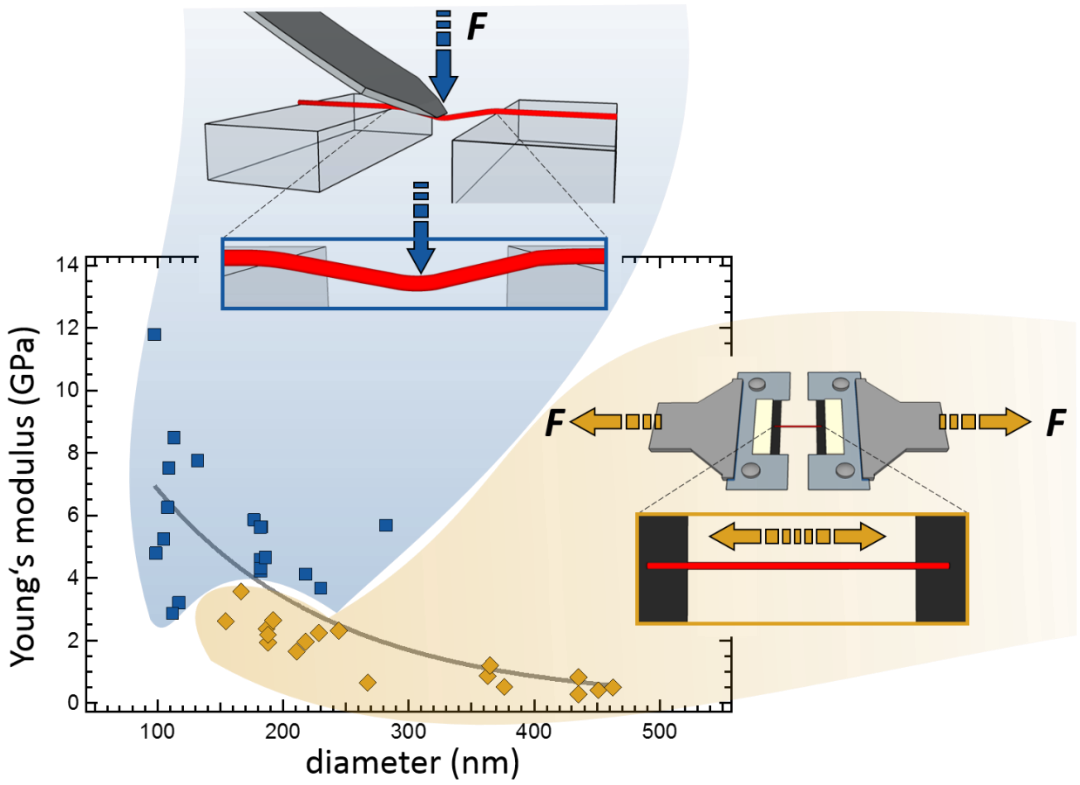

Figure 12| Summary of Young's moduli values of PVA nanofibers as determined by AFM-based three-point deformation testing (blue) or high-resolution tensile testing (yellow). The Young's moduli coincide on a master curve as illustrated by the gray line and increase with decreasing fiber diameter.

A second aspect (beyond the methodical one which is discussed above) is highlighted in chapter IV.1 and illustrates electrospinning as a fiber preparation technique that is strongly capable of influencing fiber properties. As demonstrated by nature (e.g. in spider silk), the fiber spinning procedure itself has to be considered an integral part of the final material, just as the chemical constituents of the material themselves. Through its harsh process that basically forces the fibers through the surface of the Taylor cone, electrospinning can extend and align the molecular polymer chains close to the fibers' surface. This conformational orientation of surface chains stiffens the respective parts of the fibers. As the fiber diameter decreases, the surface becomes more and more dominant with respect to the overall fiber properties. Hence, the Young's moduli increase with decreasing diameter.

III.3 Mechanical Testing of Engineered Spider Silk Filaments Provides Insights into Molecular Features on a Meso-Scale

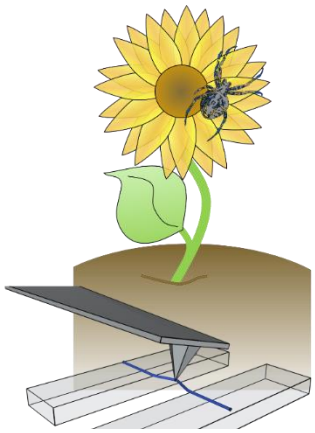

This publication takes the crucial step from elastic deformations to a full mechanical characterization up to fiber rupture properties. Thereby, it facilitates for the first time an investigation of spider silk on the filamentous mesoscale.

Vertical AFM-based three-point deformation tests (as employed in chapter IV.1) are limited in their deformation range by the z-piezo reach of the AFM (~ 10 µm). So, mostly small, elastic deformations can be carried out and used to determine the respective elastic properties as, for instance, the Young's modulus. The elastic range is yet just a small portion of a fiber's mechanical spectrum. For many applications, properties beyond that, e.g. the fiber's extensibility, its ultimate tensile strength or its toughness may even be more important. To evaluate those, however, larger deformations are indispensable and one possible way to attain those is lateral three-point testing as employed in chapter IV.2.

The course of a lateral three-point deformation test is illustrated in Figure 13 (adapted from chapter IV.2). A sharp tip cantilever travels perpendicular to the fiber axis and deforms the free-standing segment. Owing to the larger x- and y-piezo reach (~ 90 µm), the complete mechanical spectrum up to fiber rupture properties is accessible (points 1 – 5).

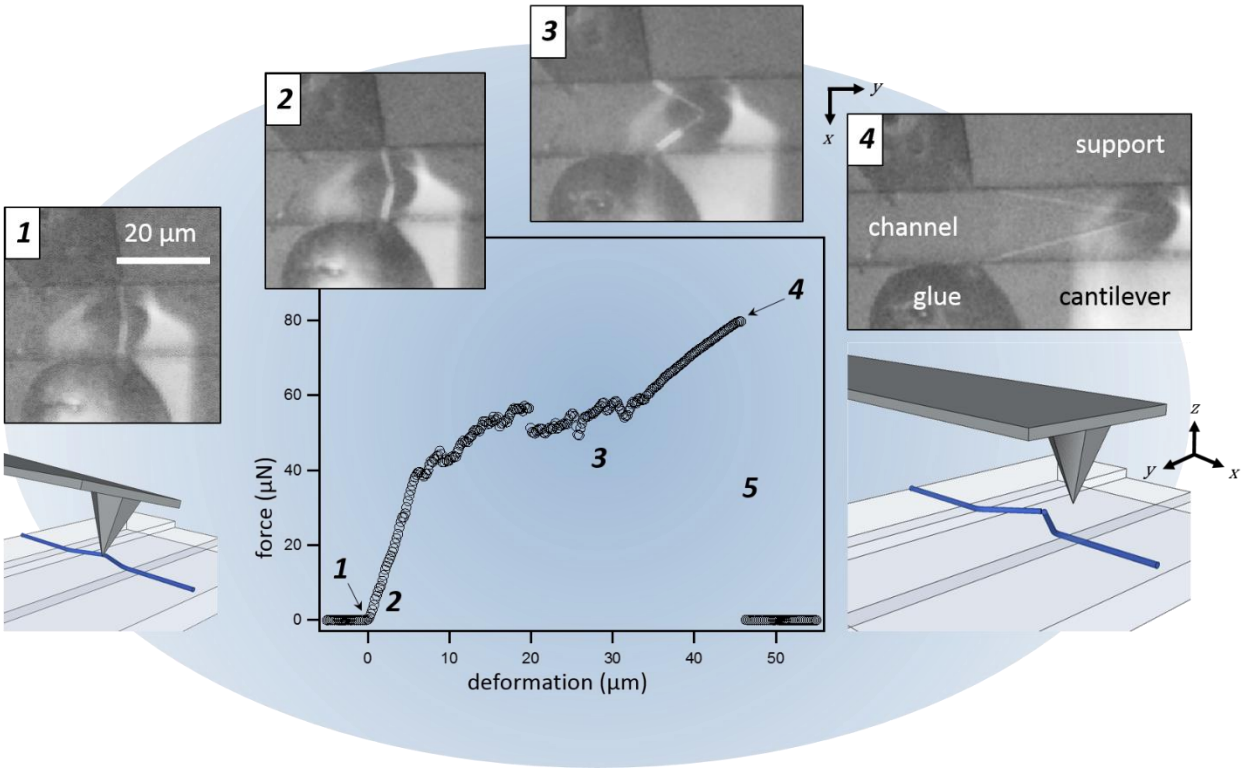

Figure 13| Lateral force-deformation curve (center) during single spider silk fiber testing at high relative humidity (~ 80 %). The labeled points are (1) the contact point, (2) the elastic and (3) the plastic regime, and (4) the maximum force followed by (5) the fiber rupture.

Together with the AFM's general tolerance for environmental conditions, this lateral approach is presented in chapter IV.2 to be suitable to mechanically characterize nanoscale electrospun protein fibers from the recombinant core sequence of dragline spider silk from *Araneus diadematus* (eADF4) at different relative humidity. In that way, the influence of hydration on the silk thread's mesoscale filaments could be investigated directly. Furthermore, the protein's β-sheet content could be adjusted from low (as-spun (AS) fibers) by a post-treatment (PT) procedure to high. Regulating a high humidity and a high β-sheet content, the single eADF4 fibers reach a toughness comparable to that of the natural dragline thread. However, the composition of the mechanical data differs as shown in Figure 14 and discussed in detail in chapter IV.2.

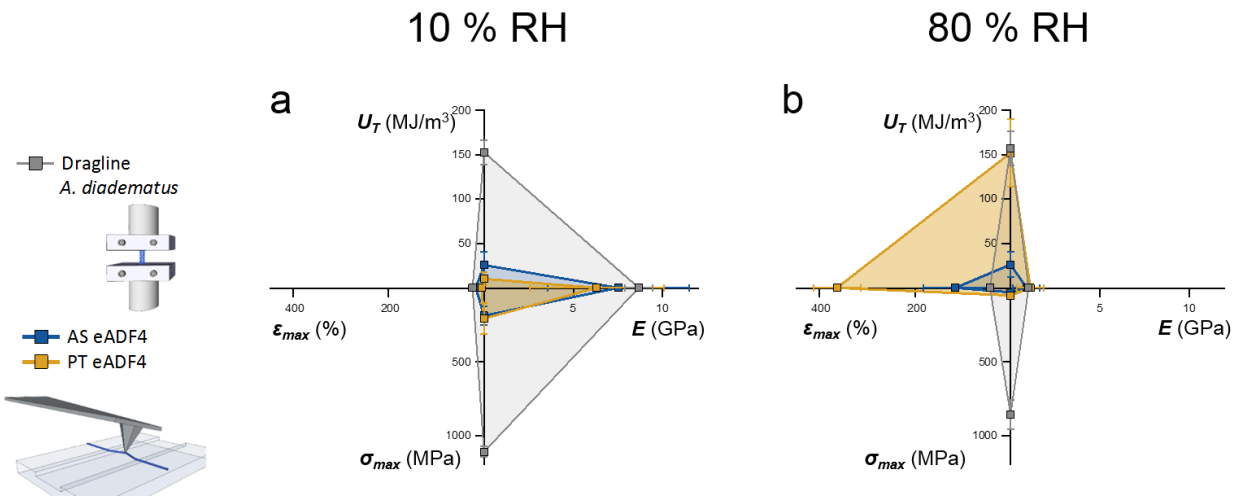

Figure 14| Mechanical data for natural dragline threads (tensile tested) and as-spun (AS) as well as post-treated (PT) eADF4 fibers (AFM tested) at (**a**) low and (**b**) high relative humidity (RH).

With respect to the general significance of hierarchal structuring in natural high-performance materials, accessing spider silk's mesoscale bridges the gap between the present molecular and macroscopic knowledge.

III.4 Long-Range Interaction Forces between 1,3,5-Cyclohexanetrisamide Fibers in Crossed-Cylinder Geometry

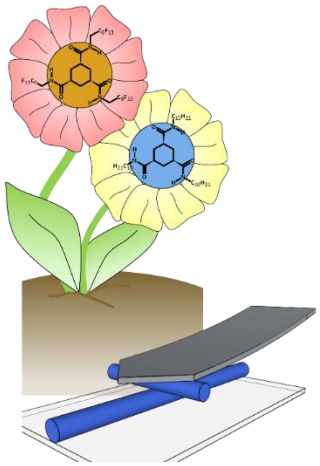

Colloidal in size, the interaction forces between fibers are governed by their surface properties. These forces can be directly measured in crossed-cylinder geometry using the colloidal probe technique as exemplified in this publication using melt-electrospun 1,3,5-cyclohexanetrisamides.

Having established single fiber mechanical testing, the next hierarchical step involves the interactions of fibers with their surroundings, i.e. amongst each other as well as with further particles, etc. A generic AFM-based approach to measure those forces is applied in chapter IV.3

. In general, tipless AFM cantilevers can be equipped with colloidal particles and used to directly measure the forces acting during an approach-retraction cycle with another surface. This is the basis of the so-called colloidal probe technique. In the specific case here, fibers with micron-sized diameters have been attached to the cantilever as well as immobilized on a surface and their interaction forces have been measured in crossed-cylinder geometry (Figure 15).

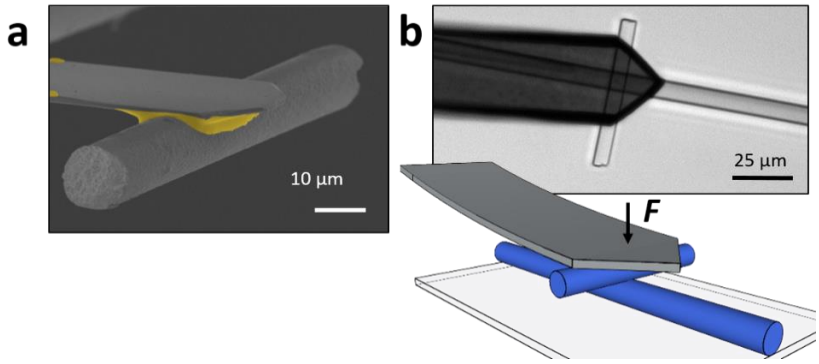

Figure 15| Micron-sized (~ 5 µm in diameter) melt-electrospun fibers from 1,3,5-cyclohexanetrisamides (CTAs) attached to tipless AFM cantilevers and during measurement in crossed-cylinder geometry. (**a**) SEM, (**b**) optical micrograph, and schematic setup.

1,3,5-cyclohexanetriamides (CTAs) provide an ideal platform to establish such measurements because they can be melt-electrospun to give smooth and homogeneous fibers with suitable diameters for handling. Furthermore, they can be modified chemically to expose different surface groups, e.g. aliphatic or perfluorinated carbon chains and hence change their surface potential in aqueous media.

The force-distance relations in aqueous solution of various ionic strength can be modeled according to the DLVO theory (see chapter II.4) and will yield a surface potential and consecutively the surface charge density (Figure 16).

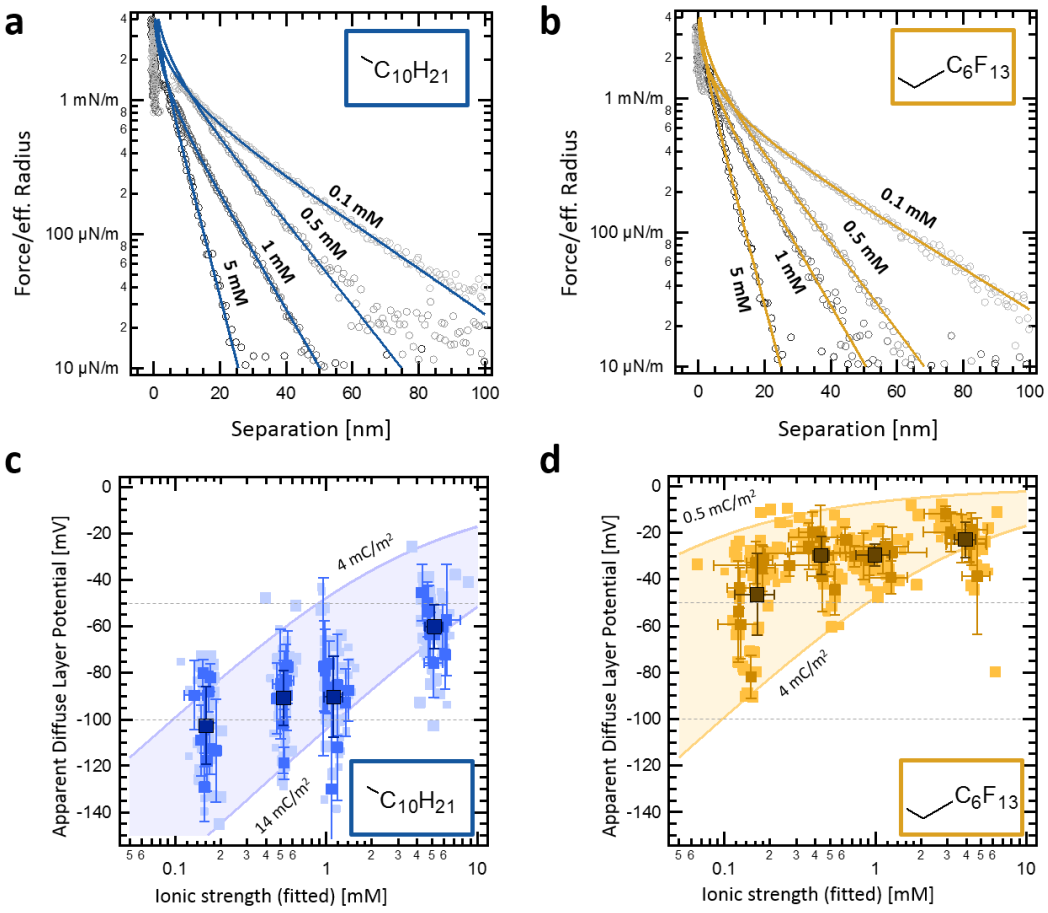

Figure 16| (**a**) and (**b**) show representative approach force curves of fibers in crossed-cylinder geometry with the surface groups indicated in the respective insets. The salt concentrations of the aqueous solution, in which these curves were measured are also given. (**c**) and (**d**) give the distinct ranges of surface charge densities determined for the different CTAs.

The charge densities of the respective CTA fibers reflect the trends as reported in the literature for aliphatic self-assembled monolayers or Teflon. Therefore, the origin of charge generation on the surface may be the accordingly asymmetric adsorption of hydroxide ions with a preference for the aliphatic surface.

III.5 Individual Contributions to Joint Publications

All presented publications in this thesis are joint collaborations with fellow researchers. My part is mostly centered around the application of the AFM for the respective fiber characterization and the interpretation of these data. The individual contributions of the authors to each publication is specified below.

Chapter IV.1 is published in the *Journal of Polymer Science, Part B: Polymer Physics* under the title "**Tensile versus AFM Testing of Electrospun PVA Nanofibers: Bridging the Gap from Microscale to Nanoscale**" by Benedikt R. Neugirg, Matthias Burgard, Andreas Greiner, and Andreas Fery.
I carried out all AFM experiments including fiber imaging and mechanical testing, programmed the evaluation procedures, evaluated the data and wrote the majority of the manuscript. Matthias Burgard prepared the fibers and performed and evaluated the tensile testing experiments. Andreas Greiner and Andreas Fery supervised the project, were involved in scientific discussions and corrected the manuscript.

Chapter IV.2 is published in *ACS Applied Materials and Interfaces* under the title "**Mechanical Testing of Engineered Spider Silk Filaments Provides Insights into Molecular Features on a Mesoscale**" by Gregor Lang, Benedikt R. Neugirg, Daniel Kluge, Andreas Fery, and Thomas Scheibel.
I immobilized the fibers and performed parts of the SEM imaging. Furthermore, I carried out all AFM experiments including fiber imaging and mechanical testing, programmed the evaluation procedures, evaluated the data and wrote approximately 50 % of the manuscript. Gregor Lang prepared the spider silk protein, spun the fibers, and performed and analyzed the post-treatment. He also tensile tested the natural silk thread as well as fiber yarns, evaluated the data and wrote approximately 50 % of the manuscript. Daniel Kluge was involved in the scientific discussions. Andreas Fery and Thomas Scheibel supervised the project, were involved in scientific discussions and corrected the manuscript.

Chapter IV.3 is published in *Polymer* under the title "**Long-Range Interaction Forces between 1,3,5-Cyclohexanetrisamide Fibers in Crossed-Cylinder Geometry**" by Benedikt R. Neugirg, Nicolas Helfricht, Steffen Czich, Hans-Werner Schmidt, Georg Papastavrou, and Andreas Fery.

I carried out all AFM experiments, namely the imaging of the fiber surfaces, the attachment of fiber segments to AFM cantilevers and the interaction measurements. I evaluated the data and wrote the manuscript. Nicolas Helfricht evaluated parts of the data, helped writing the manuscript and took part in scientific discussions. Steffen Czich synthesized the fluorinated 1,3,5-cyclohexanetrisamides and prepared the fibers. Hans-Werner Schmidt, Georg Papastavrou, and Andreas Fery supervised the project, were involved in scientific discussions and corrected the manuscript.

IV. Publications

“Wenn wir alles täten, wozu wir imstande sind, würden wir uns wahrscheinlich in Erstaunen versetzen.”

Thomas A. Edison

IV.1 Tensile versus AFM Testing of Electrospun PVA Nanofibers: Bridging the Gap from Microscale to Nanoscale*

Reproduced with permission from:

"Tensile versus AFM Testing of Electrospun PVA Nanofibers: Bridging the Gap from Microscale to Nanoscale", B.R. Neugirg, M. Burgard, A. Greiner, A. Fery, *Journal of Polymer Science Part B: Polymer Physics*, **2016**, *54* (23), 2418-2424

© 2016 Wiley Periodicals, Inc.

Design and application of mechanically extraordinary electrospun nanofibers requires their full comprehension, based on conclusive testing methods. The non-trivial task of mechanical nanofiber probing is commonly faced by specialized tensile or AFM-based three-point testing. Despite the methods' inherent dissimilarity, we herein resolve their conformity for the first time, with respect to the determination of Young's moduli.

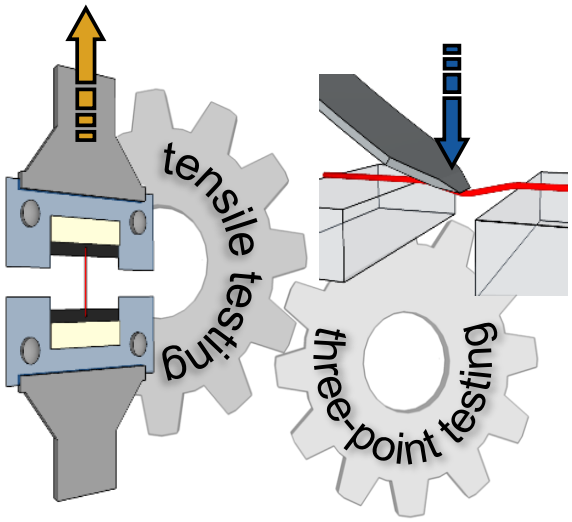

* Matthias Burgard and Benedikt R. Neugirg contributed equally to this work.

Abstract

Design and application of mechanically extraordinary nanofibers requires their full comprehension, based on conclusive testing methods. Electrospun polymer nanofibers, for instance, show a progressive and pronounced increase in their Young's moduli when diameters decrease below the µm-scale. Measurement of mechanical properties in this diameter range is challenging and in the vast majority of reports, two classes of methods are commonly used: highly sensitive tensile testing and atomic force microscopy three-point deformation testing. Despite the methods' inherent dissimilarity, we resolve their conformity for the first time, with respect to the determination of Young's moduli. Here, we benchmark them against each other for electrospun polyvinyl-alcohol nanofibers, a well-defined model system. Our results provide an experimental basis for a comprehensive understanding of nanofiber structures and its implications on their mechanical properties.

Introduction

Nanofibers are the commonly shared structural building component in both, nature's evolved mechanical high-performance composites[1, 2] and designed modern multifunctional materials.[3-5] Their attractiveness arises from their beneficial physical properties that differ significantly from the ones of the respective bulk material. High aspect ratios at diameters down to the nanoscale provide nanofibers with, for example, superior toughness[6] or extraordinary electrical properties.[7] Opening up the opportunity for the technical use of nanofibers, electrospinning has emerged as a popular and versatile technique which is capable of shaping a wide variety of materials into well-defined nanofibers even at industrially relevant scales.[8, 9] One example which is especially attractive for applications are mechanically exceptional, stiff yet tough electrospun polymer nanofibers.[6, 10]

While such nanofibers provide exciting perspectives for high-performance materials, the lack of quantitative information on fiber mechanics in the sub-micron regime is a major bottleneck for rational design of next-generation nanofibers. Intricate issues associated with mechanical testing of single nanofibers are their handling, sufficient force and extension resolution during testing, and the determination of the fiber's cross-sectional area. As conventional techniques are stretched to their limits or simply fail when facing nanofibers, new approaches have emerged: particularly

instrumented highly sensitive tensile testing[6, 11] (Figure 17 a) and three-point deformation tests[10, 12-14] that employ the atomic force microscope (AFM) (Figure 17 b).[15, 16] Among other approaches these two are most commonly applied to determine the (axial) Young's modulus E of nanofibers. In contrast, for example, widely used nanoindentation measurements aim at the radial fiber modulus which is distinct from the axial one in anisotropic (electrospun) fibers.

Both methods – instrumented tensile and AFM-based three-point testing – were used individually and independently in different studies investigating the mechanical properties of similar single polymer nanofibers. While studies on poly(L-lactic acid) (PLLA) revealed comparable results for E irrespective of the testing method and preparation procedure,[17-19] the results for nylon 6 show a pronounced distribution[20-23] and in the case of poly(ε-caprolactone) measured E values differ up to a factor of almost 60.[11, 24-28] This overall inconsistency of results may adequately be attributed to the non-uniformity of material (e.g. molecular weight) and spinning parameters (solvent type and concentration, voltage applied, flow rate, and many more) between the different studies. Yet, a thorough validation of the consistency of the testing methods themselves is still lacking and restraining fiber design. Here, for the first time, we bridge this gap between tensile and AFM-based three-point testing and elucidate their conformity studying equally electrospun single polyvinyl-alcohol (PVA) nanofibers with both methods, accordingly.

Besides the distinct fiber deformation modes, both testing methods predominantly differ in the respective length L of the specimen (Figure 17 a&b). Tensile testing requires an L of several mm which is the lower limit for feasible fiber handling. In contrast, AFM testing was reported for suspended segment lengths as short as several hundreds of nm[29, 30] and up to several hundreds of µm.[31] The probability of flaws and defects is proportional to L, hence relatively low on a µm-scale and accordingly higher for mm long fibers (albeit more dominant in brittle materials). Therefore, it is of central importance – especially when comparing the testing methods - to probe nanofibers that are homogeneous throughout these scales, that is, diameter variations should be restricted to a minimum and catastrophic flaws must be avoided. To obtain such homogenous fibers we employed electrospinning. Here, a droplet of a material's (predominantly polymer's) solution or melt is forced by high electrical fields to eject thin jets which undergo bending and stretching as they travel toward a counter electrode collector.[8, 9] Electrospinning of PVA was shown to be well-suited to form homogeneous and uniform nanofibers with lengths on the meter-scale.[32]

Results and Discussion

We prepared PVA nanofibers with diameters below 500 nm by electrospinning from an aqueous polymer solution at controlled and constant spinning parameters (i.e., temperature, humidity, voltage, flow rate, and distance of electrodes) throughout. As counter electrode collector, we used a metal frame which yielded continuous single fibers spanning the frame in free-standing, cm-long segments.[33] Individual PVA nanofibers were isolated, transferred to a corresponding substrate and consecutively subjected to both methods of mechanical testing.

We performed two independent sets of mechanical measurements, one using a tensile tester (Figure 17 left column) and one using AFM-based three-point testing (Figure 17 right column). During all testing, we kept the environmental conditions constant, that is, room temperature and 44 % relative humidity (RH). Especially the RH is known to alter mechanical properties as it has a plasticizing effect on hydrophilic materials that causes pronounced softening.[34] Therefore, thorough drying processes after fiber preparation (3 days at 40 °C and 7 mbar) and precise control of RH during the mechanical tests are essential to obtain comparable results. Using a polymer with humidity dependent mechanics, we show that the used mechanical testing methods are not only comparable for standardized low effort polymers such as polystyrene or poly(methyl methacrylate), but can rather be transferred even to demanding approaches.

The first set of measurements utilizes a highly sensitive tensile tester with a force and extension resolution of 100 nN and 100 nm, respectively. To test an individual nanofiber, it is glued onto a cardboard frame which is then mounted in the tensile tester grips. On cutting the frame joints, the grips move apart in opposite directions applying a uniaxial force (Figure 17 a&c). The fiber is stretched until failure thus covering the complete stress-strain relation. To determine the fiber's cross-sectional area A, we imaged each fiber beyond the clamping points on the cardboard frame by scanning electron microscopy (SEM) (Figure 17 e). The normalization of the measured forces to A and the deformation to the initial fiber length yields a stress-strain curve as shown in Figure 17 g. The Young's modulus is defined as the initial (elastic) slope of the stress-strain curve and can be obtained from a linear fit. Overall, this method is fast and benefits from straightforward data conversion and evaluation and the comprehensive mechanical information. Yet, its drawbacks are a relatively coarse force and extension resolution and the delicate fiber handling.

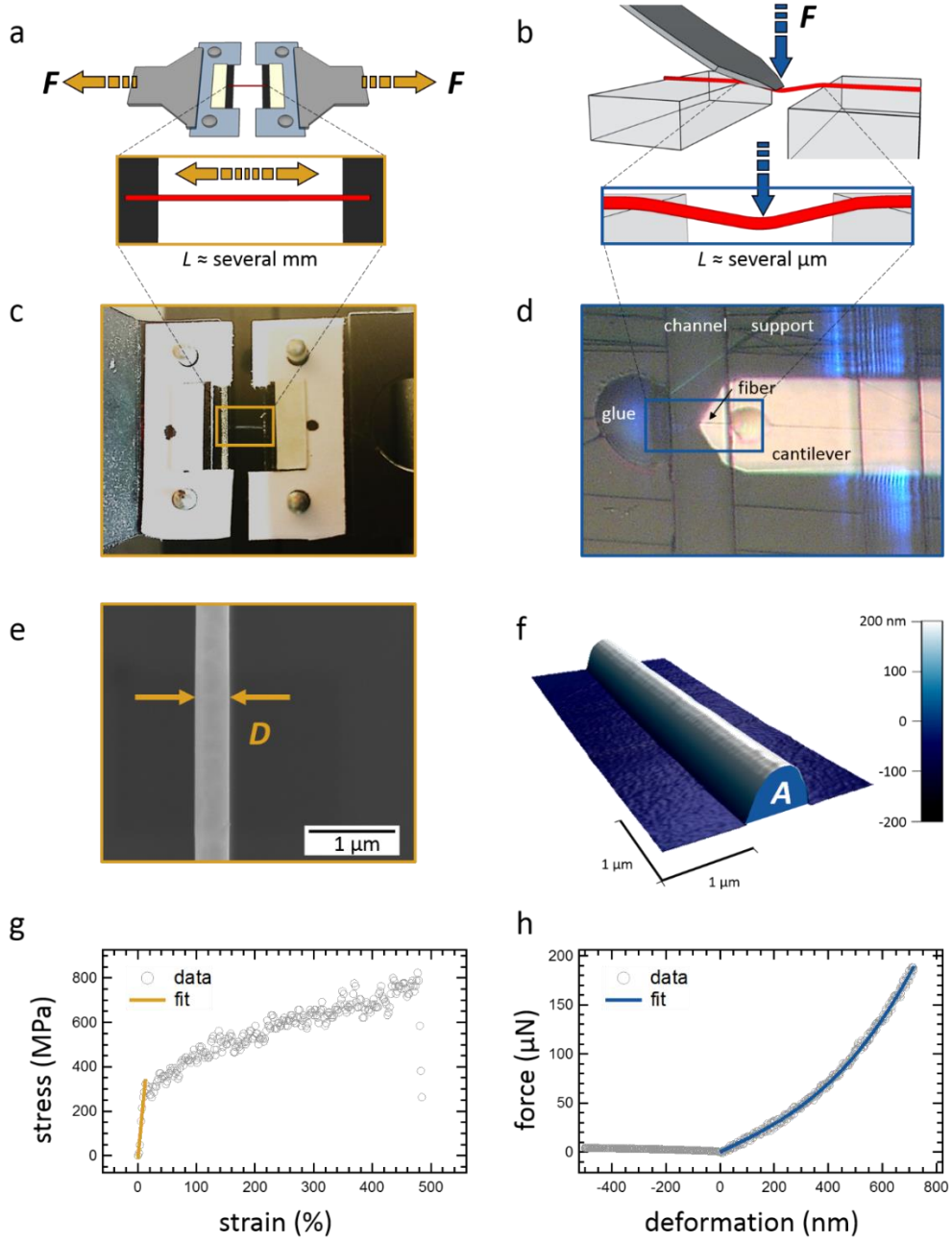

Figure 17| Single fiber tensile (left column) and AFM-based three-point testing (right column). Schematics of tensile (a) and AFM testing (b) as well as optical images of the experimental configurations (c and d). (d) shows a bottom-view optical micrograph during fiber testing. The channel width is 20 µm. The fiber's diameter D and cross-sectional area A can be determined ex-situ from SEM (e) and AFM (f) micrographs, respectively. The respective loading data for each method is given in (g) and (h) including a linear fit of the initial stress-strain slope (g) and a fit of the force-deformation data based on the model of Hudson et al.[14] (h). Both fits yield the axial Young's modulus of the fiber.

For the second set of measurements – AFM-based three-point testing – we deposited electrospun PVA fibers from the collector frame onto a glass substrate that is pre-structured with micro-channels of 20 µm width. The fibers span those channels leaving segments suspended and accessible to AFM-based testing (Figure 17 b&d). To ensure well-defined boundary conditions, we immobilized the supported fiber segments by gluing them to the substrate (glue droplets on both sides of the channel in Figure 17 d). To achieve the precise application of such small volumes of glue, we equipped a micromanipulation setup with a separate tipless AFM cantilever as a micro-"spatula." After transfer to the AFM setup, the free-standing fiber portion between these two anchoring points is subjected to vertical loading at its midpoint by a calibrated tipless AFM cantilever. The deformation range is limited by the reach of the piezo-actuators that move the cantilever. Hence, most studies focus on the deformation of the fiber vertical to the substrate, which naturally limits the experiments to small, elastic deformations. In a few cases, deformations of the fiber parallel to the substrate plane were investigated, which gives access to deformations until mechanical failure, similar to the tensile tests at the cost of lower force resolution.[35, 36]

In the AFM-based approaches, force and deformation resolution are superior, yet data conversion and interpretation is generally more complex. First, the raw data needs to be converted and corrected for the cantilever deflection to obtain the fiber's force-deformation (F-d) relation. A representative approach F-d curve is shown in Figure 17 h. Second, an appropriate model to determine E needs to be identified. At the forces applied here, deformations beyond one fiber radius R (R = 109 nm in the case shown in Figure 17 h) occur resulting in a non-linear F-d relationship. This indicates that bending and stretching contributions superimpose as described by Heidelberg et al. (*Equation 14*):[13]

$$F = \frac{192EI}{L^3} \cdot f(\alpha) \cdot d \qquad \textit{Equation 14}$$

where I is the area moment of inertia, L the length of the suspended fiber segment, and $f(\alpha)$ can be derived from *Equation 15*.

$$f(\alpha) = \frac{\alpha}{48 - \frac{192 \cdot \tanh(\sqrt{\alpha}/4)}{\sqrt{\alpha}}} \qquad \textit{Equation 15}$$

We found an expansion of the Heidelberg model - as derived by Hudson et al.[14] and Calahorra et al.[37] - which additionally accounts for pre-tension in the fiber, to conclusively fit our data. Here, f(α) can be derived depending on the pre-tension T_0 from *Equation 16*.[14]

$$\left(1-\frac{L^2T_0}{\alpha EI}\right)\left(\frac{EA}{T_0+EA}\right) \cdot\left[\frac{\alpha\cosh^2\left(\sqrt{\alpha}/4\right)}{2+\cosh\left(\sqrt{\alpha}/2\right)-6\frac{\sinh\left(\sqrt{\alpha}/2\right)}{\sqrt{\alpha}}}\cdot\left(1-4\frac{\tanh\left(\sqrt{\alpha}/4\right)}{\sqrt{\alpha}}\right)^2\right] = \frac{A}{I}d^2 \qquad \textit{Equation 16}$$

In contrast to the simple Euler-Bernoulli bending model, this model describes a larger deformation range (beyond one R) rendering the results unambiguous. Furthermore, it is worth noting that the length-to-diameter ratios of all tested fibers are well above 10 (> 67 in all cases), which is the limit for significant contribution of shearing. Hence, shearing contributions can be neglected in this study. AFM imaging allows for precise determination of the suspended fiber length L and the fiber cross-sectional area A that are required as input parameters to derive E. A representative AFM image of the supported fiber segment to derive A is shown in Figure 17 f.

Despite the different loading modes, both testing methods yield the same axial Young's modulus E. While a tensile tester applies uniaxial forces in opposite directions (Figure 17 a) inducing homogenous stresses throughout the fiber, the force in three-point testing acts perpendicular to the fiber's long axis (Figure 17 b). However, the latter analogously probes the axial E as the material is respectively stretched or compressed along the fiber direction at the bending points. Furthermore, at deformations larger than one fiber radius, the whole free-standing segment experiences additional tensile stresses.[13]

Figure 18 summarizes the results of E derived from both techniques, respectively. The diameters of the tested fibers range from 100 to 470 nm with the tensile data (yellow) covering the regime of larger D (approximately 150 – 470 nm) whereas the AFM data (blue) focuses on fibers with smaller D (below 300 nm). Each set seen individually reproduces the trend from ref. [10] for PVA nanofibers: E significantly increases with decreasing D. In the limit of large diameters, the tensile testing results approach a Young's modulus of roughly 1 GPa which corresponds to the modulus that was determined macroscopically for PVA at corresponding RH.[38] Additionally, the values from tensile and

AFM-based testing coincide on one master curve as indicated by the gray line which is an exponential fit and serves as guide to the eye. This overall consistency of the magnitude and the trend of the Young's moduli for PVA nanofibers determined independently by tensile and AFM-based testing convincingly illustrates the conformity of both methods. Furthermore, our twofold mechanical study also mutually verifies the respective approaches that are based on complementary deformation modes.

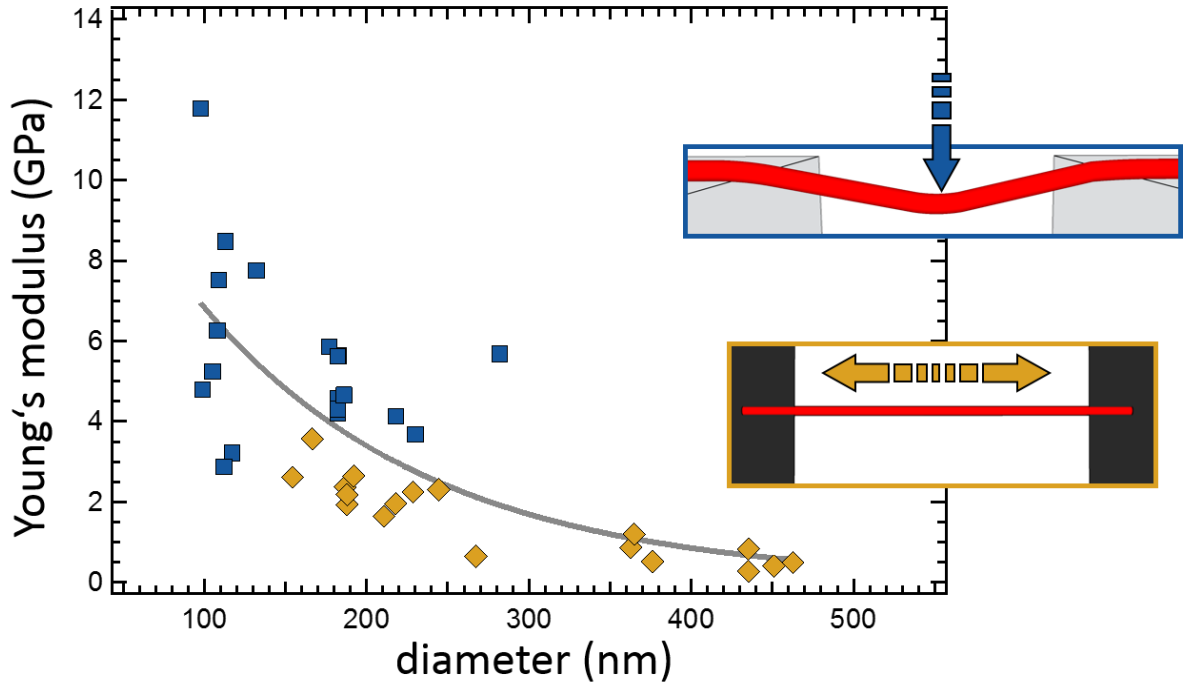

Figure 18| Young's moduli determined via three-point bending (blue) and tensile testing (yellow) versus fiber diameters. The gray line is an exponential fit and serves as a guide to the eye.

A dependence of E on the diameter as reported here, was also found for several polymer-based electrospun nanofibers[6, 10] and can be attributed to a process cascade unique to electrospinning: the high electrical field forces the polymer jet to pass through the surface of the Taylor cone. This specific process involves enormous shear rates that orient the polymer chains on the jet's surface preferentially along the fiber axis. Consecutive rapid loss of solvent and fast solidification largely conserve the jet's molecular structure in the resulting solid nanofibers including aligned chains in proximity to the fiber surface.[6, 10, 39] Usually, polymers exist in bulk as an entangled network of randomly coiled chains. These coils respond to tension as relatively soft entropic springs. The chains

at the surface of electrospun polymer fibers are pre-stretched and oriented in strain direction because of the aforementioned processes during electrospinning. On stretching of such a fiber, on average more extended polymer chains are probed which are significantly stiffer. Reducing the fiber diameter down to nanoscale dimensions dramatically increases the surface-to-volume ratio. This intensifies the surface contribution to the fiber's overall mechanical response. Consequently, one expects that fiber properties (especially E) are changing, as the diameter decreases. Indeed several studies point toward dramatic changes in mechanical properties when fiber diameters approach the sub-micron regime[6, 10] and the same trend is evidenced by our results.

Analyzing the diameter range in which E values from both methods are available (150 – 270 nm), it becomes obvious that E derived from tensile testing tends to be lower than respective AFM data and also lower than expected from previous results.[10] Furthermore, the results acquired by AFM are subjected to a larger scatter especially at very small fiber diameters. These two aspects require further discussion:

The former aspect can be explained by inevitable diameter variations along mm-long fiber segments in tensile testing. We found, for instance, the diameter of a fiber to vary by approximately 5 % around the average value of 310 nm within a segment length of 7.7 µm as measured by SEM (data not shown). Therefore, deviations should be estimated on the order of 10 %, which includes actual diameter variations as well as variations due to intricacies in SEM imaging and diameter determination. The established mechanical evaluation procedure supposes a perfectly homogeneous fiber with a cross-sectional area A which can be derived from the fiber's diameter at basically any position prior to stretching. We determined two diameter values for each fiber via SEM, namely at both ends protruding from the clamping points. Despite the overall homogeneity of electrospun fibers, small diameter variations remain experimentally inevitable. Hence, A might be smaller somewhere along the mm-long fiber segment. On stretching, the applied force is the same throughout the fiber but the stresses will peak at the position of rejuvenation. Consequently, when the true stresses are underestimated, the Young's modulus based on the measured (broader) diameters will be underestimated, accordingly. As the cross-sectional area depends on the square of the diameter, small variations will cause significant effects. However, imaging the fiber at its clamping points is established[40, 41] and convenient whereas further imaging of the fiber prior to testing would be very time-consuming and might require additional fiber treatment (e.g. sputtering of a metal layer) which in turn might alter the mechanical behavior.

In case of the AFM data, diameter variations play a minor role as the suspended segments were just 20 µm in length and were monitored via optical microscopy. Furthermore, the argument for the underestimation of E in tensile testing (stated above) cannot be applied analogously with respect to an overestimation. The observed scatter might be explained by the sensitivity of AFM-based three-point testing to experimental parameters which are progressively critical as fiber diameters decrease. Issues such as unobservable defects, convolution effects during the determination of the cross-sectional area, or fiber slack influence the data interpretation. Yet another factor that remains to be resolved is whether glue used to immobilize the supported fiber segments is absorbed to a certain extend.[28, 42] If so, it might enhance the rigidity of the fiber, especially at the bending points close to the channel edges, and consecutively lead to an overestimation of E. Furthermore, the data interpretation in nanoscopic three-point tests itself is still not standardized (as in tensile testing). The three-point configuration provides an F-d relation that contains the convoluted contributions of bending, stretching, and possibly pre-tension. Despite existing models that account for this superposition[13, 14, 37] and that were applied here, the evaluation is not fully established and remains a subject of current research.

The aforementioned aspects, however, are inevitable when manipulating, deforming, and analyzing nanofibers and need to be kept in mind when interpreting the results. A precise assessment of errors is difficult due to the unpredictable manifestation of different effects within single fiber specimen (as diameter variations or defects). Therefore, we can only estimate an error of 10 % accounting for diameter variations in tensile tested fibers as well as an error of 20 % for the AFM results based on the uncertainties related to cantilever calibration. However, all incalculables are superimposed by the scatter of the data points of Figure 18. This scatter is reasonable due to inter-fiber variations and typically seen in single fiber studies.[6] Yet it does not blur the conformity of tensile and AFM testing as evidenced by our results for PVA nanofibers. Both methods agree very well on the trends and the magnitude of E for electrospun PVA nanofibers. Our study represents a thorough basis vindicating the comparability of Young's moduli derived for nanofibers by either tensile or AFM-based three-point testing.

Conclusion

We demonstrated the conformity of tensile and AFM-based three-point testing for the determination of the Young's moduli by means of electrospun PVA nanofibers. We have chosen PVA intentionally as it is a well-studied polymer for electrospinning and highly relevant for a variety of applications, for example in technical filtration. PVA can be readily shaped into equal and long, yet homogenous fibers by electrospinning. This homogeneity of specimen produced at constant spinning parameters is a crucial prerequisite for a comparative mechanical study. Despite different specimen lengths, deformation modes, and evaluation routines, we unambiguously proved the consistency of tensile and AFM-based testing: the Young's moduli derived from both methods exhibit the same magnitude and dependence on the fiber diameter. The observed increase in E for decreasing fiber diameters can be attributed to polymer chain orientations on the fiber surface which enhance fiber stiffness.

The experimental conformity of uniaxial and perpendicular loading as evidenced here is only valid for elastic deformations and elastic properties such as the Young's modulus. At larger deformations, stress and strain distributions throughout the specimen remain homogeneous in tensile testing but exhibit pronounced local peaks at the bending points in three-point testing. These peaks render the exact determination of, for example, rupture properties such as stress and strain at break extremely difficult in a nanofiber three-point testing experiment. The comparability of both methods in that deformation regime is yet to be resolved. Our study acts as a first approach to conclusively unify mechanical testing of nanofibers to ensure consistent and reproducible results which facilitate the identification, verification, and design of advanced nanofiber-based materials.

Experimental Section

Materials and Solution Preparation: PVA powder was purchased from Sigma Aldrich (87-89% hydrolyzed, M_w = 146,000 – 186,000 g mol^{-1}) and was dissolved in distilled water (distilled water, again purified with a Millipore-Qplus machine; Column: QPAK® 2; electrical conductivity: 18.2 MΩ cm) to produce a 6 wt% PVA solution.

Electrospinning: Electrospinning was performed on a custom-built device. The voltage at the syringe was set to be +17 kV and -2 kV at the metal frame collector (inner dimensions: 17.5 cm x 3.0 cm;

frame thickness: 0.5 cm; frame depth: 0.1 cm). The distance between needle and collector was 30 cm. The temperature during electrospinning was 21 °C at a RH of 16%. After electrospinning, the samples were dried in a vacuum oven at 40 °C and 7 mbar for 3 days. For the electrospinning process a short initial pump impulse was executed, so that the electrospinning process endured only a few seconds. With that, mostly separated single nanofibers were collected on the metal frame.

Tensile Testing: For tensile testing, a single fiber was isolated on the metal frame collector by removing all neighboring fibers. This was possible as observing the collector frame against a light source uncovered the fiber positions due to light refraction and allowed for deliberate removal of individual fibers. The remaining fiber was consecutively transferred onto a cardboard frame, which was equipped with double-sided, conductive adhesive tapes to ensure fixation. This process furthermore prevented any fiber damage, as the transfer from collector to cardboard frame exclusively strained and ruptured the exterior fiber portions, while the fiber segment within the frame remained relaxed as it was fixed on both sides by the adhesive tape. After mounting the cardboard frame into the tensile tester (JSF10 Powereach; load cell: ULA-10GR Minebea Company, Japan, 0.01 – 98.07 mN measuring range, 100 nN load resolution; stepping motor: BSHB366 Shenzhen Baishan Mechatronics, China, 0.1 µm step resolution) the linked side of the cardboard frame was cut to ensure free movability of the two clamping points, which were 5 mm apart. The tests were performed at 21-22 °C and 44% RH. The speed of the test was set to be 0.094 mm s^{-1} (strain rate: 0.0188 s^{-1}). For the analysis of the cross-section area of the fibers, the two regions of the conductive adhesive tape where a fiber was attached were cut out and analyzed with a Zeiss 1530 SEM, equipped with a field-emission electron source. The samples were coated with 1.3 nm Pt with a 208HR high resolution sputter coater, equipped with a quartz crystal and a Cressington MTM-20 thickness controller to precisely control the sputtered thickness. The acceleration voltage of the SEM was 1 kV. As tests were conducted without pre-loading and the initial region of baseline noise removed for convenient data representation.

AFM Three-Point Bending & Data Analysis: PVA fibers were transferred from the metal frame collector to prestructured glass substrates (GeSiM, Grosserkmannsdorf, Germany) by simple physical contact. We identified individual fibers that appeared homogeneous and spanned a substrate channel (2 µm deep and 20 µm wide) perpendicularly by optical microscopy and immobilized the adjacent supported segments by gluing (UHU plus endfest 300, UHU GmBH & Co, Baden-Baden, Germany) using a micromanipulator (MP-285, Sutter Instrument, Novato, California) equipped with

a separate tipless AFM cantilever as micro-"spatula". Before gluing and prior to mechanical testing, the fiber's cross section and the exact length of the free-standing segment, respectively, were determined by AFM imaging (MFP3D, Asylum Research, Santa Barbara, California). Consecutively, the same AFM setup was equipped with a calibrated[43] tipless cantilever (NSC12/TL/AlBS, µmasch, Sofia, Bulgaria) which was positioned over the midst of the free-standing fiber segment with the assistance of an optical microscope (Olympus IX 71, Olympus, Tokyo, Japan). On each fiber segment we performed at least 15 deformation curves at 2 µm/s and a force setpoint of 50 – 100 nN. The ambient humidity during testing was adjusted by the ratio of a dry and a humid He-flow within the measurement cell. Each of the force-deformation curves was fit individually to the model of Hudson et al.[14] and the average of a Gaussian distribution of the Young's moduli is given as the respective value for each fiber.

Acknowledgements

The authors are indebted to DFG (SFB 840 project B8) for financial support. BRN acknowledges the support of the Elite Network of Bavaria.

References

1. Fratzl P, Weinkamer R. Nature's hierarchical materials. *Prog Mater Sci* 2007, **52**(8)**:** 1263-1334.

2. Wegst UGK, Bai H, Saiz E, Tomsia AP, Ritchie RO. Bioinspired structural materials. *Nat Mater* 2015, **14**(1)**:** 23-36.

3. De Volder MFL, Tawfick SH, Baughman RH, Hart AJ. Carbon Nanotubes: Present and Future Commercial Applications. *Science* 2013, **339**(6119)**:** 535-539.

4. Boudriot U, Dersch R, Greiner A, Wendorff JH. Electrospinning approaches toward scaffold engineering - A brief overview. *Artificial Organs* 2006, **30**(10)**:** 785-792.

5. Mitschang F, Schmalz H, Agarwal S, Greiner A. Tea- Bag- Like Polymer Nanoreactors Filled with Gold Nanoparticles. *Angew Chem-Int Edit* 2014, **53**(19)**:** 4972-4975.

6. Papkov D, Zou Y, Andalib MN, Goponenko A, Cheng SZD, Dzenis YA. Simultaneously Strong and Tough Ultrafine Continuous Nanofibers. *Acs Nano* 2013, **7**(4)**:** 3324-3331.

7. Li Y, Qian F, Xiang J, Lieber CM. Nanowire electronic and optoelectronic devices. *Mater Today* 2006, **9**(10)**:** 18-27.

8. Greiner A, Wendorff JH. Electrospinning: A fascinating method for the preparation of ultrathin fibers. *Angew Chem-Int Edit* 2007, **46**(30)**:** 5670-5703.

9. Agarwal S, Greiner A, Wendorff JH. Functional materials by electrospinning of polymers. *Prog Polym Sci* 2013, **38**(6)**:** 963-991.

10. Stachewicz U, Bailey RJ, Wang W, Barber AH. Size dependent mechanical properties of electrospun polymer fibers from a composite structure. *Polymer* 2012, **53**(22)**:** 5132-5137.

11. Tan EPS, Ng SY, Lim CT. Tensile testing of a single ultrafine polymeric fiber. *Biomaterials* 2005, **26**(13)**:** 1453-1456.

12. Kluge D, Abraham F, Schmidt S, Schmidt H-W, Fery A. Nanomechanical Properties of Supramolecular Self-Assembled Whiskers Determined by AFM Force Mapping. *Langmuir* 2010, **26**(5)**:** 3020-3023.

13. Heidelberg A, Ngo LT, Wu B, Phillips MA, Sharma S, Kamins TI*, et al.* A generalized description of the elastic properties of nanowires. *Nano Lett* 2006, **6**(6)**:** 1101-1106.

14. Hudson SD, Zhurov V, Grbic V, Grbic M, Hutter JL. Measurement of the elastic modulus of spider mite silk fibers using atomic force microscopy. *J Appl Phys* 2013, **113**(15)**:** 154307.

15. Neugirg BR, Koebley SR, Schniepp HC, Fery A. AFM-based mechanical characterization of single nanofibres. *Nanoscale* 2016, **8**(16)**:** 8414-8426.

16. Tan EPS, Lim CT. Mechanical characterization of nanofibers - A review. *Compos Sci Technol* 2006, **66**(9)**:** 1102-1111.

17. Tan EPS, Lim CT. Physical properties of a single polymeric nanofiber. *Appl Phys Lett* 2004, **84**(9)**:** 1603-1605.

18. Ryuji I, Masaya K, Seeram R. Structure and properties of electrospun PLLA single nanofibres. *Nanotechnology* 2005, **16**(2)**:** 208.

19. Jaeger D, Schischka J, Bagdahn J, Jaeger R. Tensile testing of individual ultrathin electrospun poly(L-lactic acid) fibers. *J Appl Polym Sci* 2009, **114**(6)**:** 3774-3779.

20. Li L, Bellan LM, Craighead HG, Frey MW. Formation and properties of nylon-6 and nylon-6/montmorillonite composite nanofibers. *Polymer* 2006, **47**(17)**:** 6208-6217.

21. Ding Y, Zhang P, Jiang Y, Xu F, Yin J, Zuo Y. Mechanical properties of nylon-6/SiO2 nanofibers prepared by electrospinning. *Materials Letters* 2009, **63**(1)**:** 34-36.

22. Bazbouz MB, Stylios GK. The Tensile Properties of Electrospun Nylon 6 Single Nanofibers. *J Polym Sci Pt B-Polym Phys* 2010, **48**(15)**:** 1719-1731.

23. Arinstein A, Burman M, Gendelman O, Zussman E. Effect of supramolecular structure on polymer nanofibre elasticity. *Nat Nanotechnol* 2007, **2**(1)**:** 59-62.

24. Chew SY, Hufnagel TC, Lim CT, Leong KW. Mechanical properties of single electrospun drug-encapsulated nanofibres. *Nanotechnology* 2006, **17**(15)**:** 3880-3891.

25. Wong S-C, Baji A, Leng S. Effect of fiber diameter on tensile properties of electrospun poly(ε-caprolactone). *Polymer* 2008, **49**(21)**:** 4713-4722.

26. Lim CT, Tan EPS, Ng SY. Effects of crystalline morphology on the tensile properties of electrospun polymer nanofibers. *Appl Phys Lett* 2008, **92**(14)**:** 141908.

27. Croisier F, Duwez AS, Jérôme C, Léonard AF, van der Werf KO, Dijkstra PJ*, et al.* Mechanical testing of electrospun PCL fibers. *Acta Biomater* 2012, **8**(1)**:** 218-224.

28. Baker SR, Banerjee S, Bonin K, Guthold M. Determining the mechanical properties of electrospun poly-ε-caprolactone (PCL) nanofibers using AFM and a novel fiber anchoring technique. *Materials Science and Engineering: C* 2016, **59:** 203-212.

29. Salvetat JP, Briggs GAD, Bonard JM, Bacsa RR, Kulik AJ, Stockli T*, et al.* Elastic and shear moduli of single-walled carbon nanotube ropes. *Phys Rev Lett* 1999, **82**(5)**:** 944-947.

30. Tombler TW, Zhou CW, Alexseyev L, Kong J, Dai HJ, Lei L*, et al.* Reversible electromechanical characteristics of carbon nanotubes under local-probe manipulation. *Nature* 2000, **405**(6788)**:** 769-772.

31. Schniepp HC, Koebley SR, Vollrath F. Brown Recluse Spider's Nanometer Scale Ribbons of Stiff Extensible Silk. *Adv Mater* 2013, **25**(48)**:** 7028-7032.

32. Zhang C, Yuan X, Wu L, Han Y, Sheng J. Study on morphology of electrospun poly(vinyl alcohol) mats. *Eur Polym J* 2005, **41**(3)**:** 423-432.

33. Beachley V, Wen X. Effect of electrospinning parameters on the nanofiber diameter and length. *Materials science & engineering C, Materials for biological applications* 2009, **29**(3)**:** 663-668.

34. Vehoff T, Glisovic A, Schollmeyer H, Zippelius A, Salditt T. Mechanical properties of spider dragline silk: Humidity, hysteresis, and relaxation. *Biophys J* 2007, **93**(12)**:** 4425-4432.

35. Wu B, Heidelberg A, Boland JJ. Mechanical properties of ultrahigh-strength gold nanowires. *Nat Mater* 2005, **4**(7)**:** 525-529.

36. Carlisle CR, Coulais C, Namboothiry M, Carroll DL, Hantgan RR, Guthold M. The mechanical properties of individual, electrospun fibrinogen fibers. *Biomaterials* 2009, **30**(6)**:** 1205-1213.

37. Calahorra Y, Shtempluck O, Kotchetkov V, Yaish YE. Young's Modulus, Residual Stress, and Crystal Orientation of Doubly Clamped Silicon Nanowire Beams. *Nano Lett* 2015, **15**(5)**:** 2945-2950.

38. Soundararajah QY, Karunaratne BSB, Rajapakse RMG. Mechanical Properties of Poly(vinyl alcohol) Montmorillonite Nanocomposites. *Journal of Composite Materials* 2009.

39. Richard-Lacroix M, Pellerin C. Molecular Orientation in Electrospun Fibers: From Mats to Single Fibers. *Macromolecules* 2013, **46**(24)**:** 9473-9493.

40. Jiang S, Duan G, Zussman E, Greiner A, Agarwal S. Highly Flexible and Tough Concentric Triaxial Polystyrene Fibers. *ACS Appl Mater Interfaces* 2014, **6**(8)**:** 5918-5923.

41. Chen F, Peng XW, Li TT, Chen SL, Wu XF, Reneker DH*, et al.* Mechanical characterization of single high-strength electrospun polyimide nanofibres. *J Phys D-Appl Phys* 2008, **41**(2)**:** 025308.

42. Gestos A, Whitten PG, Spinks GM, Wallace GG. Tensile testing of individual glassy, rubbery and hydrogel electrospun polymer nanofibres to high strain using the atomic force microscope. *Polym Test* 2013, **32**(4)**:** 655-664.

43. Hutter JL, Bechhoefer J. Calibration of atomic-force microscope tips. *Rev Sci Instrum* 1993, **64**(7)**:** 1868-1873.

IV.2 Mechanical Testing of Engineered Spider Silk Filaments Provides Insights into Molecular Features on a Mesoscale*

Reproduced with permission from:

"Mechanical Testing of Engineered Spider Silk Filaments Provides Insights into Molecular Features on a Mesoscale", G. Lang, B.R. Neugirg, D. Kluge, A. Fery, T. Scheibel, *ACS Applied Materials and Interfaces,* **2017**, *9* (1), 892-900

© 2016 American Chemical Society

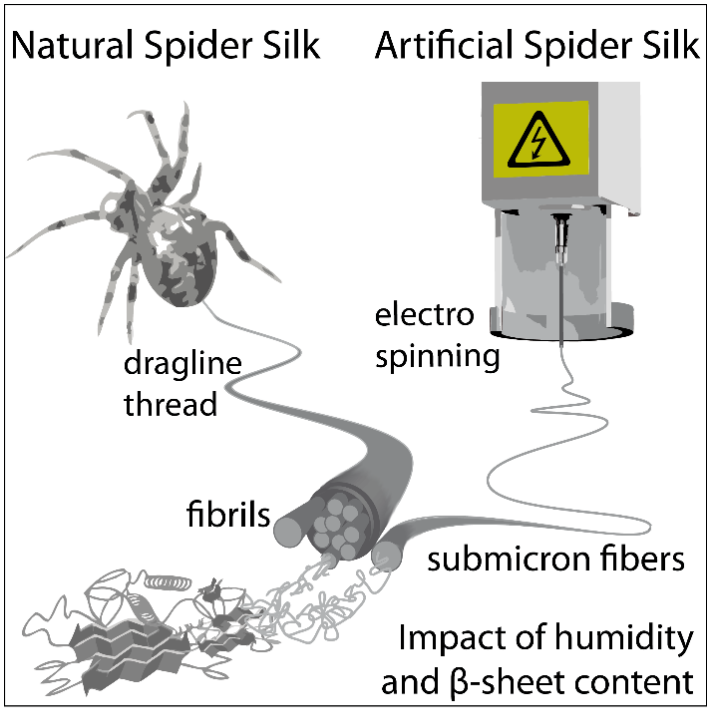

* Gregor Lang and Benedikt R. Neugirg contributed equally to this work.

Abstract

Spider dragline silk shows the highest toughness in comparison to all other known natural or man-made fibers. Despite a broad experimental foundation concerning the macroscopic silk thread properties as well as a thorough simulation-based molecular understanding, the impact of the mesoscale building blocks, namely nano-/submicrometer-sized filaments, on the mechanical properties of the threads remains the missing link. Here, we illustrate the function of these mesoscaled building blocks using electrospun fibers made of a recombinant spider silk protein and show the impact of β-sheet content and fiber hydration on their mechanical performance. Specifically elucidating the interplay between β-sheet-cross-linking (fiber strength) and structural water (fiber extensibility), the results bridge the gap between the molecular and the macroscopic view on the mechanics of spider silk. It is demonstrated that the extensibility of the here used single (MaSp2-like) protein system is in good accordance with the simulated extensibilities published by other groups. Furthermore, sufficient hydration of the fibers is shown to be a prerequisite to obtain a toughness in the range of that of natural dragline silk. Preliminary studies on electrospun fibers of the MaSp2-based recombinant spider silk proteins used in this work have indicated their basic applicability in the technical field of filter systems as well as in regenerative medicine. The presented work provides a fundamental understanding of the mechanical performance of such fibers under different wetting conditions, a prerequisite to further specify their potential for such applications.

Introduction

The highly defined hierarchical structure of spider dragline silk is synergized by protein composition and spinning process, yielding an unrivalled toughness of the natural dragline silk thread.[1, 2] Despite a broad experimental foundation concerning the macroscopic thread properties[3, 4] as well as a computational simulation-based molecular understanding,[5, 6] the role of the main structural building units, the mesoscale nano-/submicrometer-sized filaments, and their impact on the mechanical properties of the threads are still unresolved. In natural dragline (DL) silk threads, a thin protective and regulatory shell (comprising lipids, glycoproteins, and minor ampullate spidroins) encases these major ampullate spidroin (MaSp) filaments (see Figure 19) without significantly contributing to the mechanical properties.[7] The amino acid sequence of MaSp comprises a core domain with highly repetitive motifs flanked by short, nonrepetitive carboxy- (NR_C) and amino-terminal (NR_N) domains.

While the termini prevent undesired protein aggregation in the gland and trigger protein assembly in the duct,[8, 9] the structure of the core domain defines the mechanical properties of the spider's final silk thread.[4] Typically, most MaSp core domains comprise characteristic polyalanine stretches which fold into distinct ordered β-sheet nanocrystallites (dimensions between 5 and 7 nm) and glycine-rich repeats composing an amorphous matrix embedding those nanocrystallites upon spinning.[5] The thread's structural hierarchy is illustrated on the left side of Figure 19.

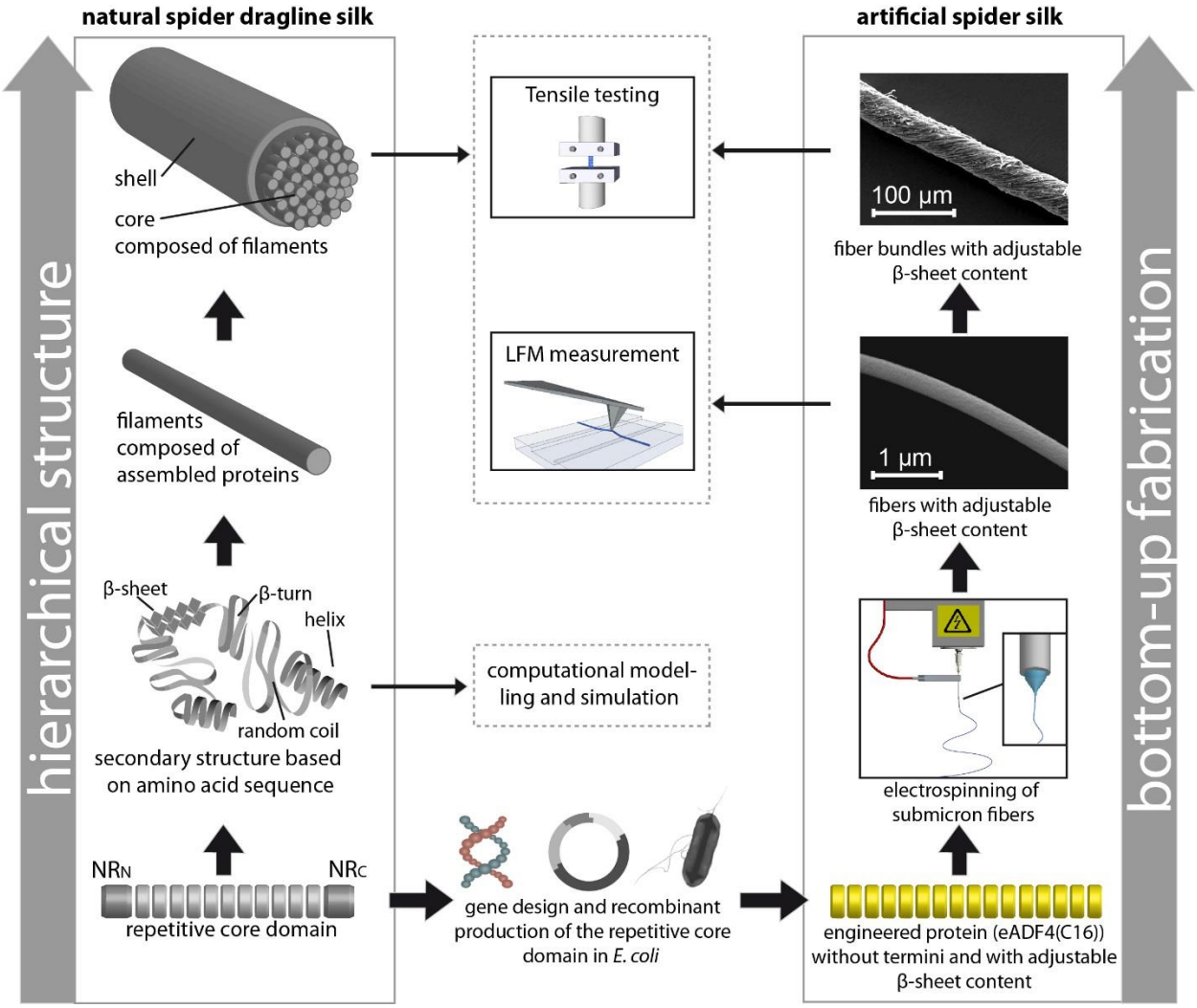

Figure 19| From hierarchical *Araneus diadematus* DL (dragline) silk to mechanically strong electrospun single fibers and fiber bundles made of recombinant eADF4(C16). NR_N: nonrepetitive amino-terminal domain; NR_C: nonrepetitive carboxy-terminal domain; LFM: lateral force microscopy.

To investigate the structure-property relationship of natural DL, previous studies correlated the macroscopic mechanical properties of natural DL silk threads to environmental conditions.[10, 11] Therein, individual contributions of proteins, filaments, or other components could not be determined. Alternatively, bottom-up molecular dynamic simulations were used to investigate the significance of β-sheet nanocrystals for the silk's toughness but without a direct correlation to structural hierarchical orders.[5, 6] Here, we bridge this gap performing (nano-)mechanical measurements based on lateral force microscopy (LFM) to identify the deformation behavior of electrospun mesoscale single-component MaSp fibers (150 – 450 nm in diameter) mimicking the filaments of natural silk (Figure 19, right side). Beyond single mesoscale fibers, this bottom-up approach also allows for the fabrication and tensile testing of macroscopic bundles made of these filaments.

We used a previously established biotechnological procedure to recombinantly produce spider silk mimics based on the repetitive sequence of one *Araneus diadematus* MaSp2 protein. Unlike other orb weaving spiders, *A. diadematus* has at least two different MaSp2 proteins, namely fibroin 3 and 4 (ADF3 and ADF4). In this work, an engineered *A. diadematus* fibroin 4 (eADF4(C16)), based on the consensus sequence of ADF4, was electrospun into filaments.[12] The molecular weight of the protein is determined by the number of repeats of the specific consensus sequence, the so called C-module, consisting of polyalanine and a glycine-rich region. Here, eADF4(C16) with 16 C-repeats (MW = 48 kDa) was used due to its excellent performance in an established electrospinning process and its high potential for application as filter materials and in regenerative medicine.[13, 14] Furthermore, the absence of both flanking termini in eADF4(C16) enables for the first time an explicit mechanical investigation of the core domain quantifying the impact of the interplay between β-sheets and amorphous structures in combination with structural water within the fibers (without the influence of the termini). These fundamental insights can on the one hand be transferred to the natural system and on the other hand significantly contribute to understand the mechanics of recombinant spider silk fibrils on a single-protein level bridging the gap between atomistic simulations and macroscopic experiments. Moreover, these findings constitute an important prerequisite to specify the fields of application of recombinant spider silk fibers.

Results and Discussion

eADF4(C16) (recombinantly produced in *Escherichia coli* as previously published)[12] was dissolved in hexafluoroisopropanol (HFIP) and subsequently electrospun into submicrometer fibers (Figure 20 a, b). The routes toward sample preparation for single fiber and fiber bundle testing differ in the counter electrode used during electrospinning. Two parallel conducting wires generate free-standing fiber segments bridging those wires. The segments can be easily transferred to structured glass substrates to be used for single fiber testing (Figure 20 a). In contrast, aligned fiber mats are gained using a rotating cylinder as counter electrode, and the mats can be twisted into fiber bundles (Figure 20 b). The rotational velocity of the cylinder collector has a dominating impact on the fiber alignment.Figure 20 c, d correlates both parameters and best alignment for a surface speed of 33 ms^{-1} is demonstrated, which has been used in the following for the fabrication of fiber bundles.

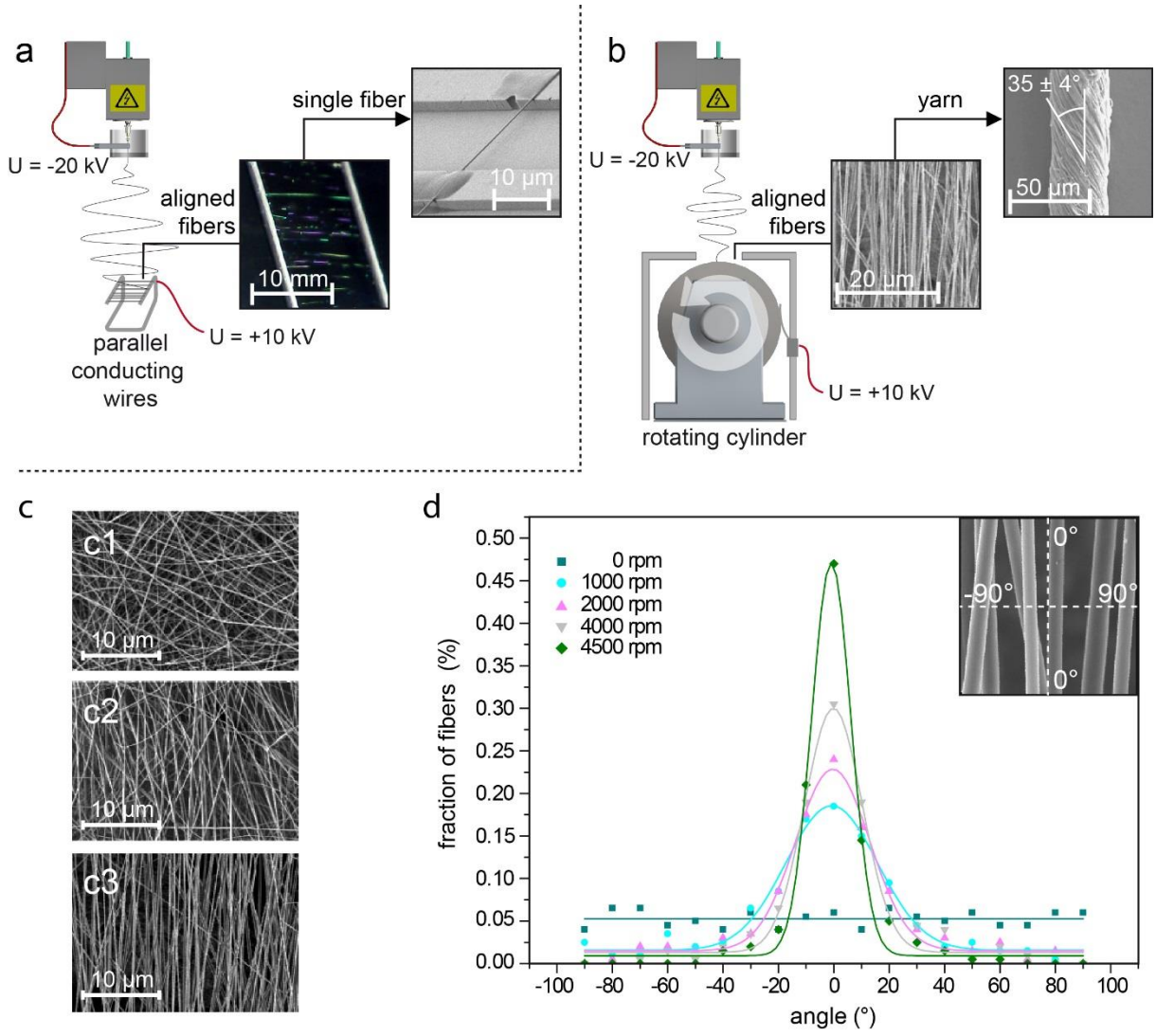

Figure 20| Two different custom-built electrospinning setups were applied using a potential difference of 30 kV (-20 kV at the spinning head and +10 kV at the collector, distance: 20 cm), a feeding rate of 14 µL min-1 and an 18G needle. Electrospinning was performed at controlled relative humidity (50 % RH) and room temperature. a) To obtain aligned single fibers for LFM measurements, two conducting wires mounted in parallel (length: 2 cm, gap: 1 cm) were applied as a collector/counter electrode, and electrospinning was performed for a short period of time (approx. 4s). b) For the production of fiber bundles, a rotating drum was employed as a collector/counter electrode with a diameter of d = 14 cm at a maximum speed of 4500 rpm (≙ 33 m s-1 surface speed). Fiber mats were removed subsequently and twisted into bundles with a twist angle of 35 ± 4° (10 samples, analyzed by SEM). c) SEM images of eADF4(C16) fiber mats spun at different reeling speeds of the collecting cylinder (surface velocities): c1) 0 rpm (0 m s-1); c2) 1000 rpm (7.3 m s-1) and c3) 4500 rpm (33.0 m s-1). d) Angular distribution of the fiber orientation of eADF4(C16) fibers electrospun at different reeling speeds as indicated.

HFIP as a solvent typically conserves α-helical conformations and dissolves crystalline structures, which has also been previously demonstrated in the specific case of eADF4(C16).[15] This enables the production of silk fibers with an initially low β-sheet content. The fast evaporation of HFIP during electrospinning kinetically hinders conformational switches and traps the spidroins in this as-spun (AS) state with a low β-sheet content. To induce crystallization, a post-treatment (PT) procedure was conducted applying 2-propanol, ethanol or methanol vapor in a way similar to that previously published.[13] While the AS fibers can be dissolved upon water immersion, the PT procedure renders eADF4(C16) water insoluble which can be attributed to the increase in β-sheet content. To monitor the evolution of secondary structures in eADF4(C16), time-resolved secondary structural analysis was carried out using Fourier transform infrared spectroscopy (FTIR) and subsequent Fourier-self-deconvolution (FSD).[16] An exemplary evolution for ethanol PT is shown in Figure 21 c, while the self-deconvoluted spectra of a sample are given in Figure 21 a, b without treatment and after 240 min in ethanol vapor including all identified secondary structure contributions.

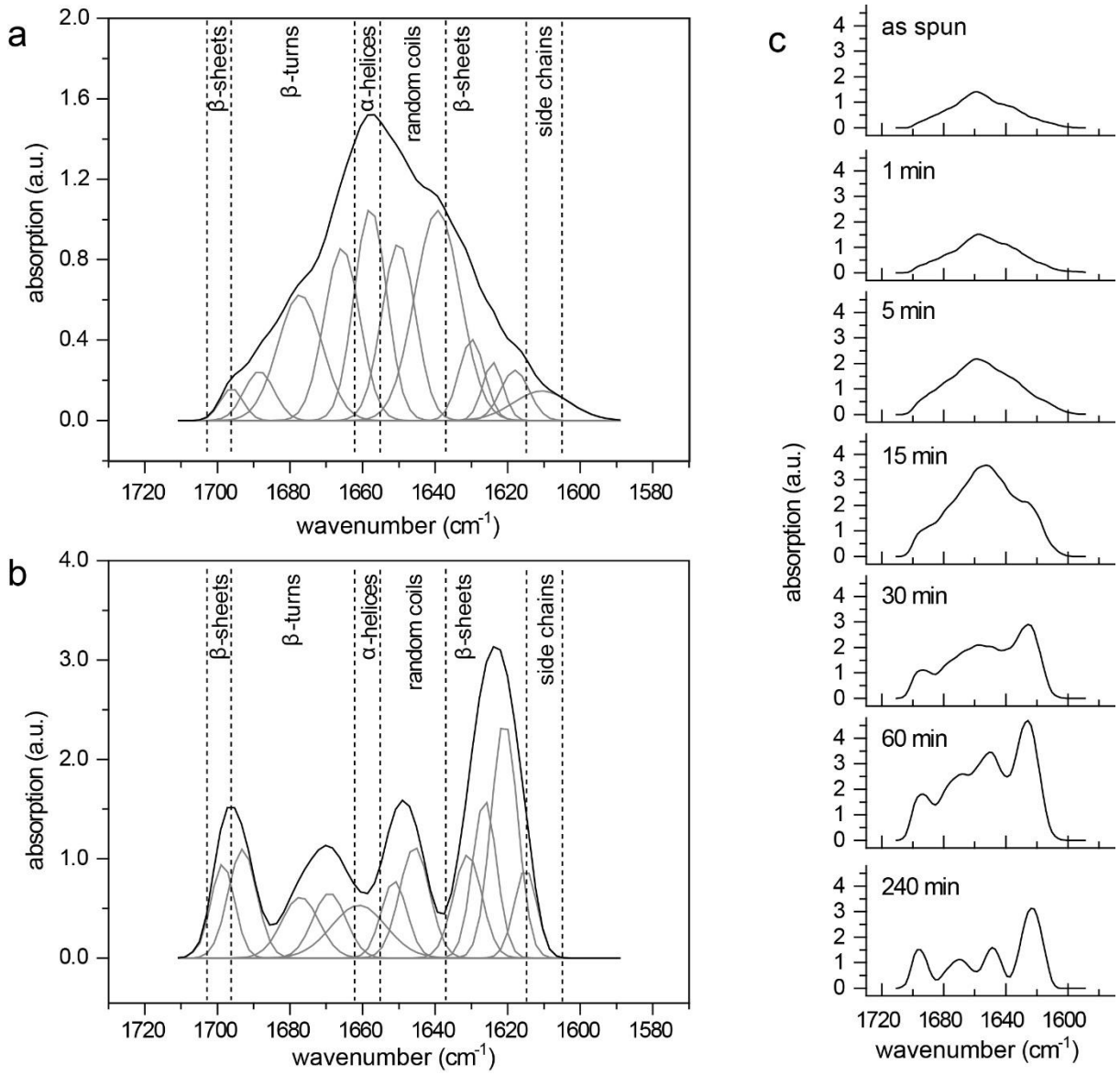

Figure 21| FSD FTIR spectra (grey) of the amide I band (black) of eADF4(C16) fiber mats. Curve fit and secondary structure classification of an a) untreated and b) ethanol-treated sample (60°C, 240 min). c) Time-dependent alteration of the amide I band of eADF4(C16) fibers during ethanol vapor exposure at 60°C.

At 60°C, the initial amount of β-sheet structures was 10.9 ± 1.5 % and remained low and constant in air (AS fibers), whereas it increased upon PT in alcohol vapor at this temperature to a maximum value of 35 ± 4 % (PT fibers) (Figure 22). The final composition of secondary structures was similar irrespective of the alcohol employed. However, the speed of structural conversion was found to

depend on the molecular size of the alcohol indicating a diffusive process. As we found morphological changes, i.e., coalescence of the fibers in 2-propanol vapor, and due to the toxicity of methanol, we decided to employ ethanol PT for all further experiments.

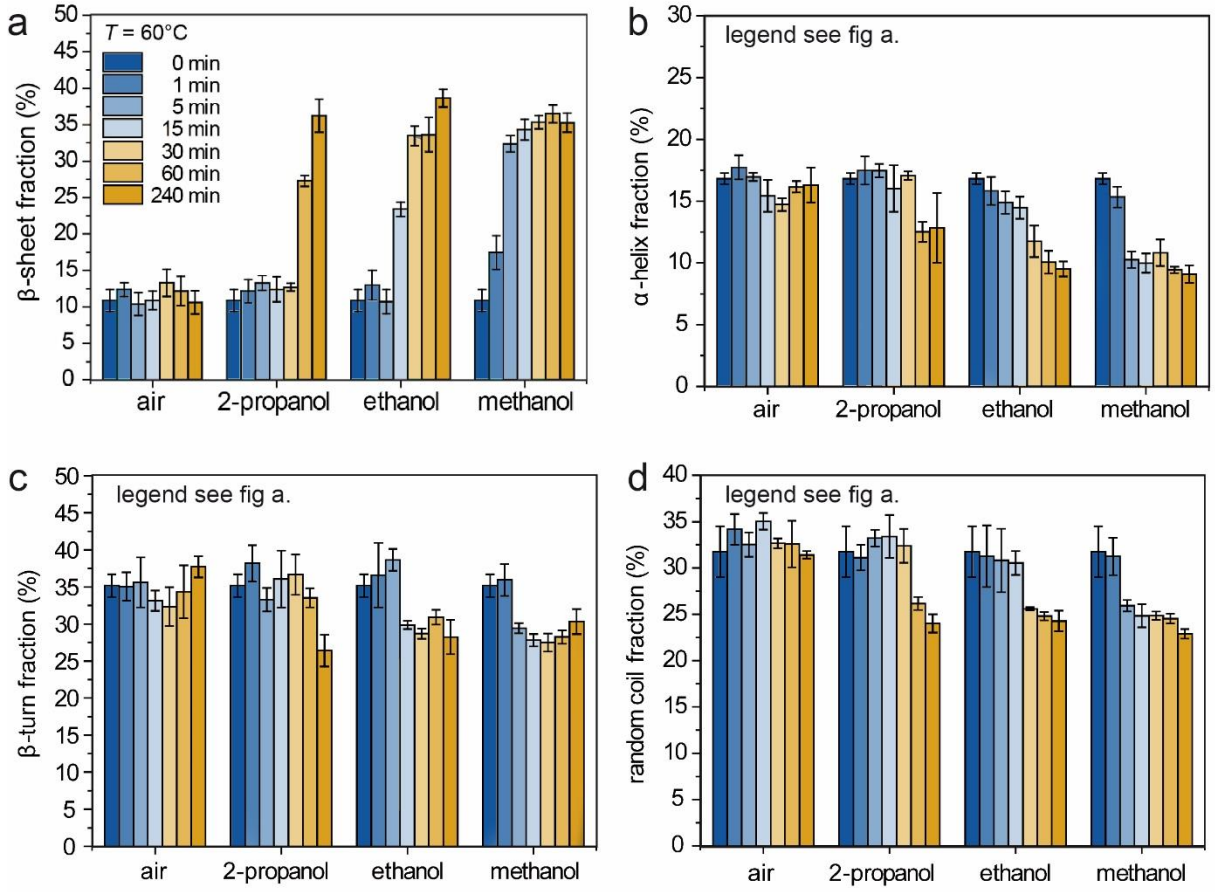

Figure 22| Time-dependent protein secondary structure analysis of eADF4(C16) after post-treatment with alcohol vapor (2-propanol, ethanol and methanol) at 60 °C. As a control, a series of measurements was carried out in air at 60 °C. The secondary structure fractions were calculated by integration of the fitted curves (see Figure 3) and subdivided in a) β-sheets, b) α-helices, c) β-turns, and d) random coils.

AS and PT fibers were comprehensively mechanically analyzed on the single-fiber level and complementarily for fiber bundles (Figure 19). Direct probing of the material properties of single eADF4(C16) submicrometer-fibers imposes special requirements on the testing technique: a sufficient resolution in force and deformation at adjustable environmental conditions and the

capability to test consecutive, short segments within the same fiber to exclude fiber defects or statistical interfiber property variations. For measurements of electrospun single fibers, we employed three-point deformation testing based on LFM[17] (Figure 19 center and Figure 23). For that purpose, electrospun eADF4(C16) fibers were transferred to a grooved glass substrate to obtain suspended segments which were successively clamped by gluing (see Figure 23 a). An atomic force microscope (AFM) cantilever was used to mechanically deform the respective free-standing fiber segment until it ruptured (micrograph sequence in Figure 23 a). The cantilever's sharp tip was used to load the segment laterally at its middle which allows for deducing force-deformation curves from the cantilever torsion (Figure 23 b, c). The elastic deformation regime was fitted to determine the Young's modulus based on established models.[17, 18] The extensibility and strength were derived from characteristic points in the force curves (as indicated in Figure 23 c) and represent lower estimates as local stress peaks occur at the bending points. After adjustment of the RH, a consecutive segment spanning the adjacent groove of the same fiber can be probed in a similar manner. The single-fiber results were benchmarked against tensile-tested natural *A. diadematus* silk threads. Furthermore, electrospun fibers were twisted into bundles and subsequently tensile-tested (Figure 19 center).

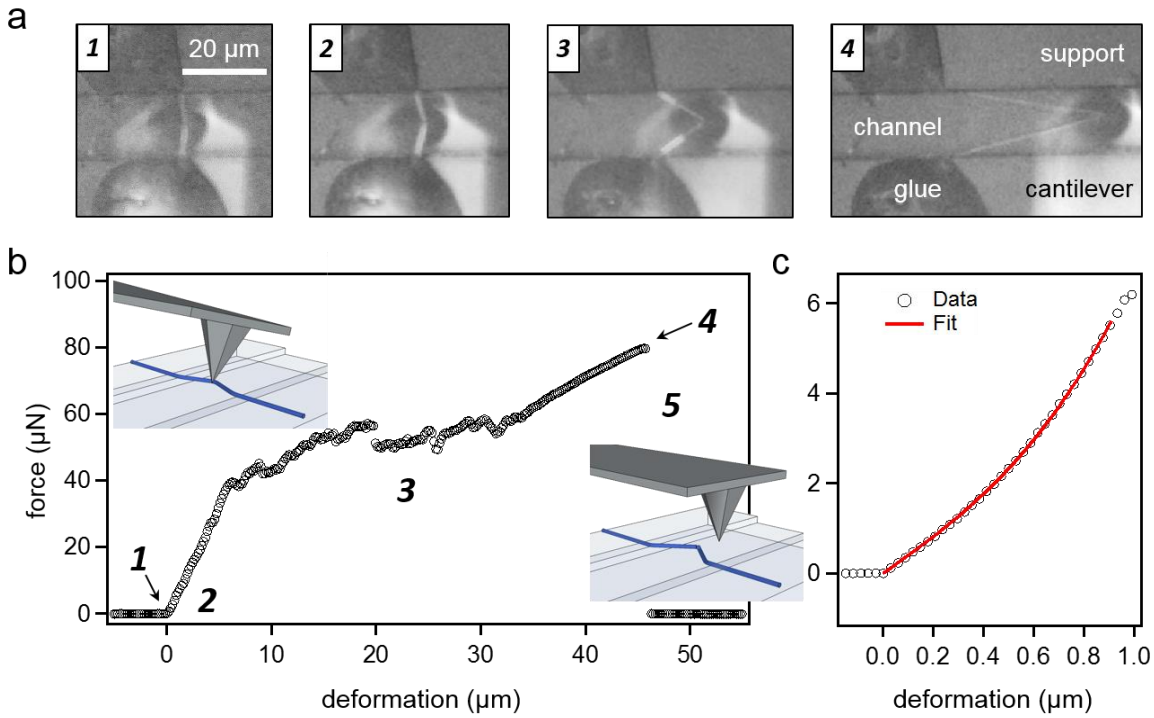

Figure 23| LFM testing of a post-treated eADF4(C16) fiber at 80 % RH. a) Series of optical microscope images during LFM testing in correspondence to the numbered points in panel b illustrating the extraordinary extensibility of post-treated fibers at 80 % RH. b) Force-deformation curve of an eADF4(C16) single fiber upon LFM testing with specific regions as marked by numbers: contact point (1) and elastic regime (2) used to determine the Young's modulus by a fitting procedure according to Hudson et al. (as detailed in panel c). A plastic regime (3) is followed by the maximum force (4) and the point of steepest decrease (5), which defines the strength and extensibility of the fiber.

The mechanical behavior of both morphologies, individual fiber and fiber bundle, demonstrates the interplay between physical β-sheet cross-linking and water-induced segment mobility of the amorphous matrix.

A. diadematus dragline silk showed a toughness (U_T) of 156 MJ m^{-3} composed of a Young's modulus (E = 6.5 GPa), a strength (σ_{max} = 1.1 GPa), and an extensibility (ε_{max} = 27%) in accordance with previously published results.[19] Figure 24 a, b compiles the sets of these parameters for the natural silk thread (gray) in comparison to those of the LFM results of nontreated AS fibers with low (blue), as well as PT fibers with high β-sheet content (yellow) in dry (Figure 24 a: 10 % RH) and humid (Figure 24 b: 80 % RH) conditions (for the detailed set of mechanical properties, also at 30 % RH, see

Figure SI 1). Comparing the mechanical parameters of the dry and the humid systems (Figure 24 a, b), the plasticizing effect of water becomes evident: Water enhances the protein mobility/fiber extensibility at the expense of stiffness (lower *E* at increased RH). This observation can be rationalized considering water saturating hydrogen bonding sites and thus interrupting H-bonds.[20, 21]

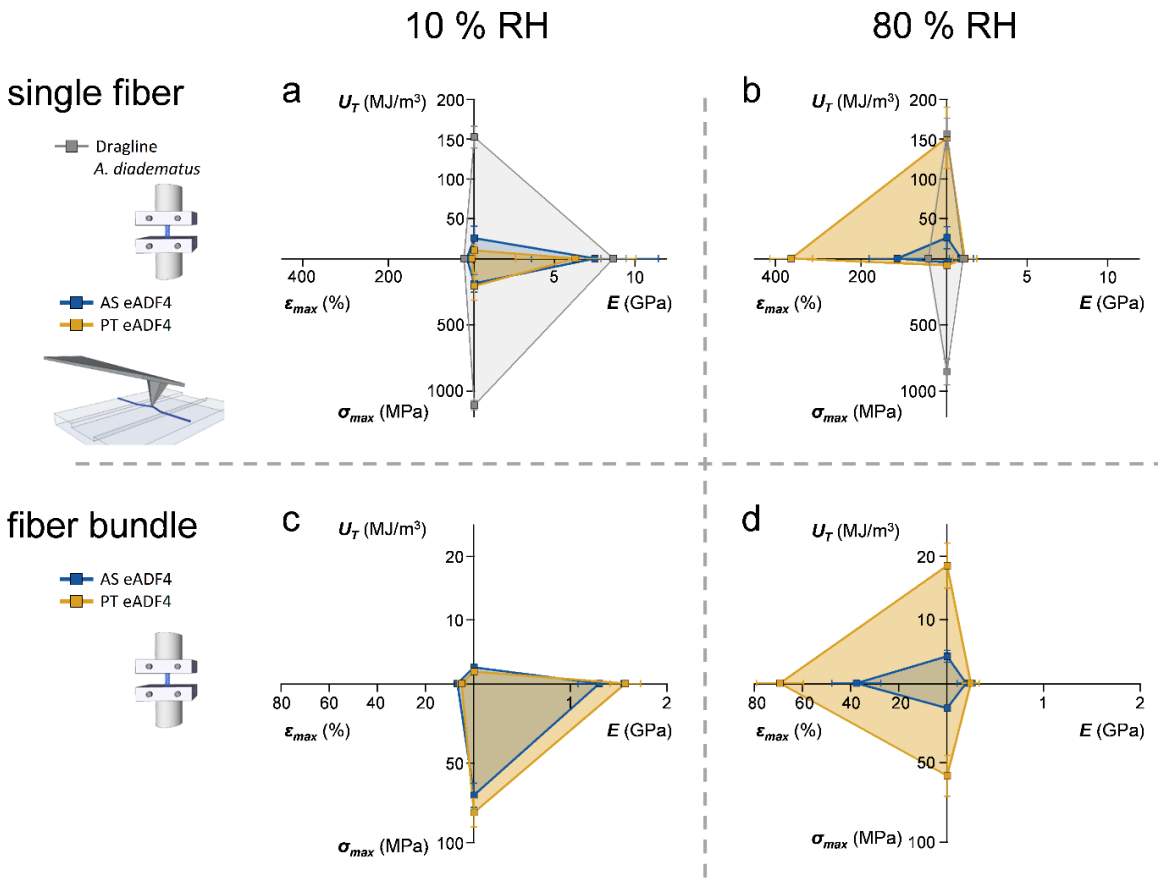

Figure 24| Mechanical properties of electrospun eADF4(C16) single fibers and fiber bundles compared to that of *A. diadematus* dragline silk: U_T, denotes toughness, *E*, Young's modulus, σ_{max}, fiber strength and ε_{max}, fiber extensibility, respectively. The specimen and the respective testing method are given in the left panel. Additional histograms for all mechanical properties and their standard deviations can be found in Figure SI 1. a) At 10 % RH, the natural silk thread outperformed the artificial eADF4(C16) fibers. b) The toughness of the PT eADF4(C16) fibers matched that of the natural dragline silk at 80 % RH. Whereas natural silk mostly maintained its strength, the high toughness of the recombinant fibers arose from their extraordinary extensibility at high humidity. A similar effect was seen for eADF4(C16) fiber bundles, although the overall mechanical properties were lower: c) At 10 % RH, the measured parameters of AS and PT eADF4(C16) fiber bundles did not differ significantly. d) At 80 % RH, the extensibility and strength distinctly increased for PT

fiber bundles resulting in a higher toughness. Please note the different axis-ranges in case of fiber bundles. AS = as spun; PT = post-treated. The error bars indicate the standard deviation.

The natural threads differed significantly from the artificial filament-like system in the extent of their response to humidity changes. Their attenuated reaction to moisture points to the shell's regulatory function, foremost keeping core spidroins hydrated and thus elastic in dry environment. The water-induced softening was compensated by a slight increase of ε_{max}, and σ_{max} was almost completely preserved maintaining the vital toughness of natural silk. Recombinant electrospun fibers experienced a decrease in E and σ_{max}, yet PT fibers overcompensated these effects with an enormous increase in ε_{max} (by a factor of almost 70). This increase corresponded to a 9-fold higher extensibility compared to that of natural DL silk, yielding a similar toughness. Furthermore, wet PT fibers remained significantly stronger (higher σ_{max}) than untreated AS ones. The mechanical properties of fiber bundles were much lower than those of single fibers (Figure 24 c, d). This mechanical inferiority was most likely due to morphological defects and the lack of strong fiber-fiber interactions. However, the relative tendencies upon comparing AS and PT fiber bundles unambiguously confirmed the nanomechanical results: AS and PT fiber bundles predominantly differed in σ_{max} and ε_{max} yielding a significantly increased U_T in PT fiber bundles.

The structural model in Figure 25 interrelates the secondary structure of eADF4(C16) proteins with the mechanical properties of fibers made thereof. The humidity-induced rubber transition could be explained similar to that of natural DL silk by the disruption of hydrogen bonds in the amorphous regions of the thread's core proteins.[20, 21] Furthermore, hydration mobilizes the amorphous glycine-rich matrix thus attaining extensibility based on an enhanced sliding ability of single proteins against each other, due to the lack of terminal (dimeric) domains keeping them in place (Figure 25 b, d). In contrast, the lack of water causes a reduction in molecular mobility explaining the fibers' brittleness as found at 10 % RH (Figure 25 a, c). The differences observed between AS and PT eADF4(C16) fibers were based on the distinct β-sheet content: the rapid solidification of eADF4(C16) during electrospinning partially preserved the initially predominant α-helical / random coiled structure and inhibited the transformation into β-sheet structures (AS fibers). Subsequently, moisture absorption led to an expansion of the amorphous regions within AS fibers, and in spite of enhancing the mobility of the protein chain, water molecules also prevented the formation of β-sheets as they occupied hydrogen binding sites (Figure 25 a, b). PT of electrospun eADF4(16) fibers, however,

induced a replacement of several weak (individual) hydrogen bonds as found in the amorphous regions with densely packed (synergetic) ones typical for β-sheets (Figure 25 c, d).[22]

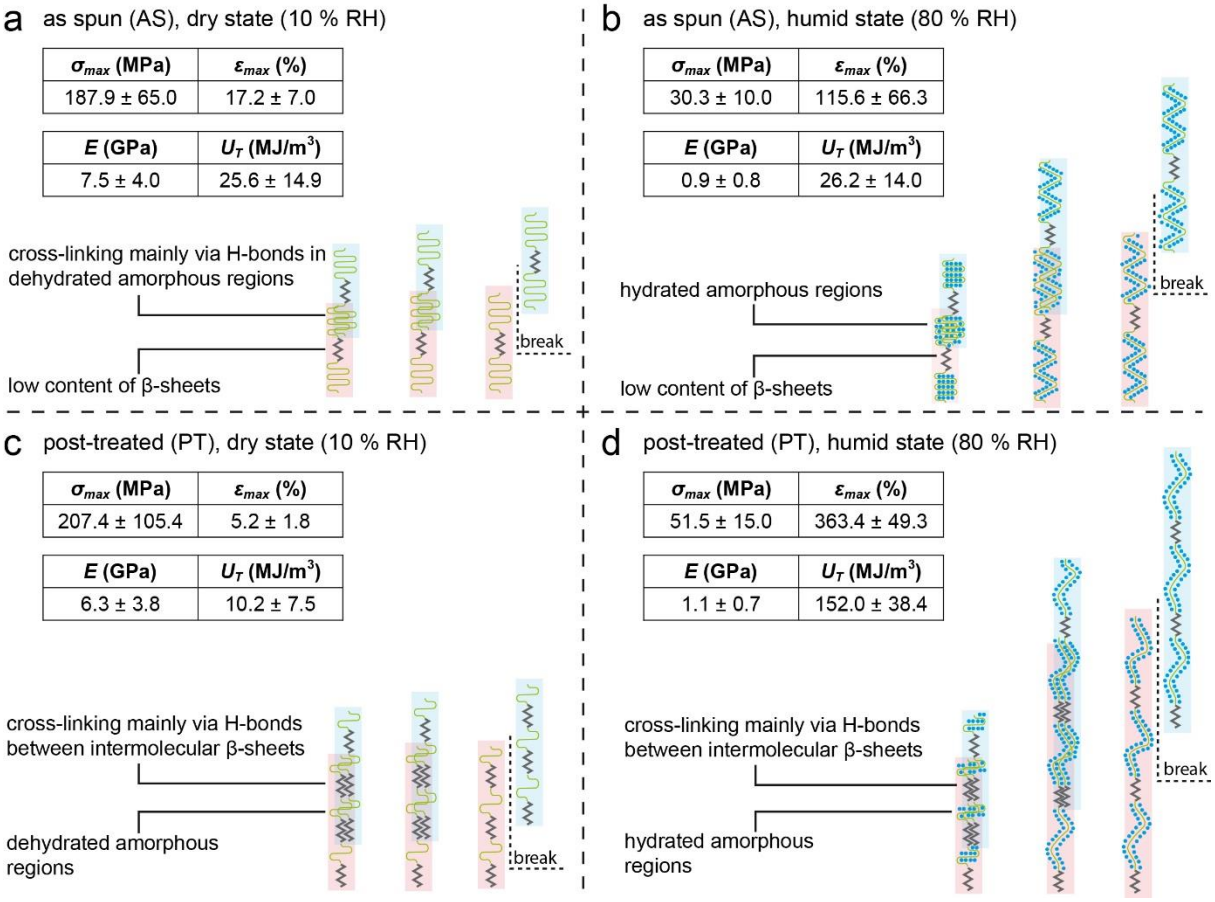

Figure 25| Relation of secondary structure and mechanical properties of single fibers shows the impact of β-sheet content (AS and PT) and state of hydration (schematic illustration of two interacting eADF4(C16) proteins, one highlighted in red and one in blue). a, b) As spun (AS) single fibers display a low β-sheet content (11 ± 2 %). a) In the dry state, the structure is mainly stabilized by weak hydrogen bonds between the amorphous regions of protein chains. b) With increasing humidity, water (blue dots) is absorbed and intercalates with hydrogen bonding in the amorphous regions, resulting in increased mobility of the chains and thus a significantly higher extensibility ε_{max}. Solvating of hydrogen bonds furthermore leads to decreasing tensile strength σ_{max} and elastic modulus E. Though the mechanical properties completely change, the resulting toughness U_T stays nearly the same upon hydration of AS filaments. c, d) Post-treatment of filaments results in a high β-sheet content (39 ± 1 %) enabling the formation of a much higher number of intermolecular β-sheets. c) In the dry state, this leads to a significant decrease of ε_{max} and only slight changes of σ_{max} and E, resulting in a reduction of U_T compared to AS samples in panel a. d) Hydration of the post-treated fibers

displays similar trends as seen for untreated ones in panel b, but the fibers retain more intermolecular hydrogen bonds (through the β-sheet structures), enabling further elongation ε_{max}. Strikingly, the combination of stable cross-linking via intermolecular β-sheets and the hydrated extensible amorphous regions results in a significantly higher toughness indicating that the secondary structure, its molecular interaction, as well as structural water is essential for the mechanical properties of spider silk fibers.

On the basis of a denser physical cross-linking by β-sheets in PT fibers, failure at high RH can be rationalized as follows: AS fibers rupture when the external force overcomes the sum of interaction forces of hydrogen bonds in the amorphous regions connecting individual protein strands. As the individual interactions are comparatively weak, the fiber strength σ_{max} is accordingly low. During fiber elongation, AS fibers will rupture as soon as the force required for stretching the amorphous regions surpasses the cohesion forces provided by the amorphous interactions, i.e., ε_{max} is reached. In PT fibers, β-sheets distribute and transfer stress more homogeneously. As they firmly interconnect the protein strands, σ_{max} can be traced back to breaking stronger β-sheet structures (synergetic hydrogen bonds) as compared to weak (individual) hydrogen bonds in the amorphous regions. Accordingly, the elongation at break ε_{max} is increased elucidating the remarkable extensibility (Figure 25 d).

A related β-sheet-rich proteinaceous system is amyloid fibrils which have also been investigated applying (geometrically limited vertical) single-fibril testing approaches based on AFM.[23, 24] Structural analysis of recombinant spider silk proteins and amyloid-like fibrils has revealed predominant similarities apart from minor structural differences such as the presence of 3_1-helical structures and/or random coil conformations in spider silk.[25] Though it has been shown that the Young's modulus of amyloid fibrils is in the range of the here tested spider silk fibers[26] a direct comparison remains difficult due to a lack of experimentally determined mechanical data such as the extensibility and sensitivity to humidity of amyloid fibrils.[27] Furthermore, it is so far impossible to produce continuous, i.e., endless, amyloid fibers, which in contrast is one big advantage of silk.

Comparing the results in this experimental work with simulation approaches, the model in Figure 25 is in accordance with previously published atomistic simulations of the mechanical behavior of MaSp2 protein segments from a different species, *Nephila clavipes*.[5] Keten et al. observed a sigmoidal constitutive shape of force-deformation curves, an initially high modulus followed by strain softening, and eventual strain hardening. This could be rationalized by the structural model presented here, since this shape coincides with our findings for single fibers, and the simulated

extensibilities (179 - 312 %) approximately fit the ones found in this experimental study (363 ± 49 %). Whereas the simulation assumes perfect alignment of protein chains in strain direction, the alignment of chains in electrospun fibers may deviate therefrom to a certain extent, giving rise to additional hidden length revealed upon stretching. The extensibility of natural spider silk dragline usually is in the range of 30 %.[4, 9] This striking difference to artificial silk can be explained by the impact of the nonrepetitive terminal domains that are missing in both, the simulated short sequence segments and the recombinantly produced eADF4(C16) core domain used here. In the natural spinning process, the carboxy-terminal domains form disulfide-linked parallel dimers and the amino termini dimerize upon pH drop inducing the preassembly of a lyotropic liquid crystalline phase.[19, 28] The terminal-domain-induced oligomerization reduces the average mesh size in the silk's molecular network, predesignating the β-sheet formation and alignment. Upon strain, this configuration is less extensible but stronger, which explains the discrepancy in the strength-extensibility combination as found in natural DL silk and eADF4(C16) fibers. Furthermore, it must be considered that natural dragline is composed of not only MaSp2 (the blueprint of eADF4(C16)) but also MaSp1 proteins; thus, the mechanical properties are also determined by its composite nature. Strikingly, both combinations yield a similar toughness if a sufficient state of hydration and crystallization is provided. This emphasizes the need of including (structural) water as an important parameter in silk mechanics simulations.[29]

Conclusion

In summary, our mechanical analysis of recombinant eADF4(C16) fibers elucidates the basic structural mechanisms governing spider silk mechanics and uniquely quantifies the crucial role of (structural) water for the toughness of the spidroin filaments. Furthermore, the study bridges the gap between simulations of molecular mechanics[5] and the macroscopically observed mechanical properties of spider silk threads. Combined with previous studies on electrospun eADF4(C16) fibers demonstrating their high biocompatibility and the ability to morphologically trigger cell adhesion and proliferation, the mechanical data obtained in this work can be applied to further evaluate their potential for specific technical or biomedical applications.[14] The extraordinary extensibility of post-treated hydrated fibers could be attractive in the field of nerve regeneration, where the material should be flexible to preserve the nerve connection.

Experimental Section

Electrospinning: All proteins were produced and purified as published previously.[12] eADF4(C16) (10 % w/v) was dissolved in 1,1,1,3,3,3-hexafluoro-2-propanol (HFIP, Alfa Aesar, Karlsruhe, Germany) and electrospun using a custom-built setup at a potential difference of 30 kV, a feeding rate of 14 µL min^{-1} and a 18G needle (Terumo, Tokyo, Japan). To obtain aligned single fibers for LFM measurements, two conducting wires mounted in parallel (length: 2 cm, gap: 1 cm) were applied as a collector/counter electrode, and electrospinning was performed for a short period of time (ca. 4s). For the production of fiber bundles, a rotating drum was employed as a collector/counter electrode with a diameter of d = 14 cm at a maximum speed of 4500 rpm (≙ 33 m s^{-1} surface speed). The degree of fiber alignment was determined upon analyzing SEM images with ImageJ 1.42q (National Institutes of Health, Bethesda, MD, USA) to measure the angles of 200 fibers per sample and subsequent Gaussian fitting applying Origin 8.1 (OriginLab, Northampton, MA, USA) (see Figure 2 d). Fiber mats were removed from the substrate and manually twisted into bundles with a twist angle of 35 ± 4° (analyzed by SEM). This twisting was done extremely carefully to largely prevent stress in the fibers/bundles prior to mechanical testing. Electrospinning was performed at controlled humidity (50 % RH) using a FR 400 humidifier (Mytrom, Heilbad Heiligenstadt, Germany) at room temperature.

Forced Silking: DL silk of Araneus diadematus was forcibly silked from an adult individual (body weight: 400-440 mg) at 3 cm s-1 in air. The spider was taken out of its web and placed under an overturned glass beaker. After a few minutes of settling, the spider stopped moving, and the DL fiber could be pulled by tweezers through the beaker's outlet and transferred to a rotating cylinder in a custom built glovebox under controlled humidity (30 % RH) at 25 °C. Forced silking (reeling speed: 3 cm s-1) was carried out until interrupted by the spider, which usually occurred after forced silking of 5-30 m.

Post-Treatment and FTIR: Electrospun eADF4(C16) single fibers and fiber bundles were placed free-hanging in a heated vessel (60 °C). First, alcohol (2-propanol, ethanol or methanol) was added to create an alcohol steam atmosphere for β-sheet induction. Incubation times were varied to comprehend the time dependency of the post-treatment procedure. In the next step, alcohol was

removed and water was added to enable moisture absorption, thus softening of the samples for subsequent handling.

FTIR spectra were recorded using a Hyperion microscope (Bruker, Ettlingen, Germany) in contact-free transmission mode at 800 – 4000 cm^{-1}. Each spectrum is the result of averaging 60 individual spectra. To determine individual secondary structure elements, the amide I band (1600 – 1700 cm^{-1}) was analysed using the Opus 6.5 software from Bruker Optics Corp. (Billerica, MA, USA) applying FSD. As shown in earlier studies,[30] the procedure was performed according to a previously established protocol for secondary structure analysis of fibrous proteins.[16] It includes a narrowing of the spectra using a high pass filter and a curve fitting of the deconvoluted curves resulting in Gaussian Peaks that represent individual secondary structure elements. The relative peak areas were calculated and assigned to the corresponding structural fractions as described in the reference.[16]

Mechanical testing: LFM. Electrospun fibers were transferred onto grooved glass substrates (channel depth = 2 µm and width = 20 µm)[31] and immobilized using a 2-component epoxy glue (UHU plus endfest 300 by UHU GmbH & Co, Baden-Baden, Germany). A combined setup of an AFM (MFP3D by Asylum Research, Santa Barbara, California) and an inverted optical microscope (Olympus IX 71 by Olympus, Tokyo, Japan) was used for mechanical testing. Prior to and after mechanical testing, each fiber was imaged via AFM to determine the length of the suspended segment as well as the fiber cross section. Thoroughly calibrated cantilevers[32] (NSC35, µmasch, Sofia, Bulgaria) were used to deform suspended segments at their middle with the tip apex 1 µm below the fiber's top side. The cantilever was chosen to have a vertical spring constant of 8.61 N m^{-1} and a lateral spring constant of 202 N m^{-1}, accordingly. These values allowed for sufficient force resolution in the elastic regime as well as sufficient stability to rupture the fibers. The cantilever's sharp tip loaded the segment laterally at its midst deducing force-deformation curves from the cantilever torsion. The elastic deformation regime was fitted to determine the Young's modulus based on established models.[18, 33] The mechanical rupture properties were derived from characteristic points in the force curves and represent lower estimates as local stress peaks occur at the bending points. All experiments were performed in a Humidity Sensing Cell (Asylum Research, Santa Barbara, California, USA) enabling monitoring and control of the ambient humidity. Using a lab-built flow setup, the humidity could be set by adjusting the relative flows of a humid and a dry

helium stream. Experiments were performed at 10, 30 and 80 ± 2 % RH. Thus, 43 individual segments of AS eADF4 fibers and 31 segments of ethanol post-treated fibers were measured.

Tensile testing. For macroscopic mechanical testing, fiber bundles and forcibly silked natural DL silk threads were cut into 1 cm pieces and glued onto plastic sample holders (frame shaped) with a gap width of 2 mm. The sample holders were then clamped in the grips of a tensile tester (Electroforce 3200, Bose, Bloomington, Minnesota, USA), the plastic frame connections between the grips were cut, and the specimens were deformed at 0.005 mm s^{-1} until failure while recording force and deformation (applied load cells: 0.49 and 2.45 N, Bose, Bloomington, Minnesota, USA). The number of measured samples was >20 for each analysis condition. Humidity was controlled using dry air and an ultrasonic humidifier (Mytrom, Heilbad Heiligenstadt, Germany). To account for the less dense structure of fiber bundles, an effective cross section using the weight per length of the bundle and the protein density (1.3 g cm^{-3}) was calculated. Furthermore, the tapering of fibers undergoing high deformations was considered by calculation of true stress and true strain.[34]

Acknowledgements

G. Lang and B. R. Neugirg contributed equally to this work. The authors thank Prof. Dr. Jeffrey L. Hutter for fruitful discussions. This work received financial support from the German Research Foundation (Deutsche Forschungsgemeinschaft) within the SFB 840 (projects A8, B8, and C4, respectively). B. R. Neugirg acknowledges the support of the Elite Network of Bavaria.

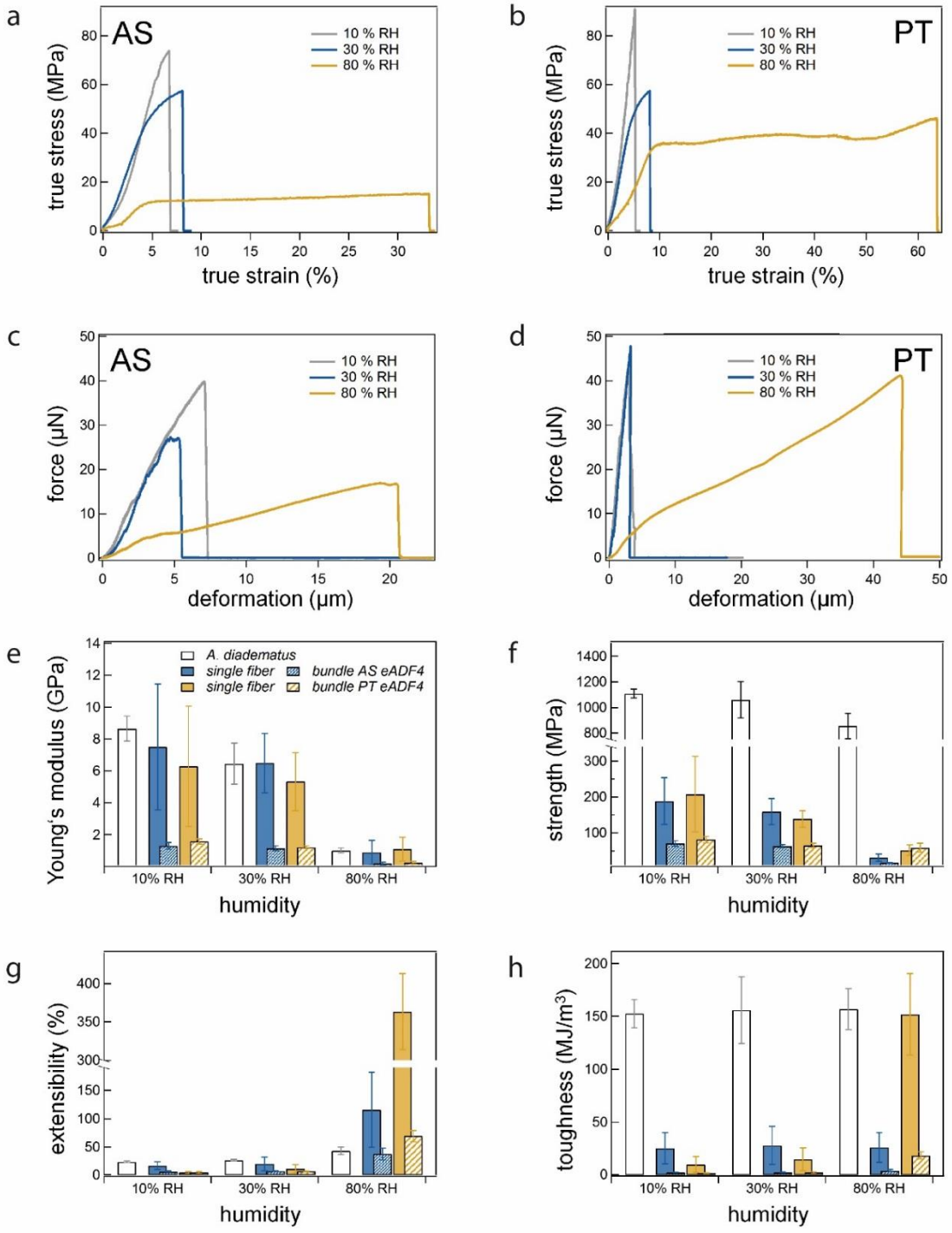

Figure SI 1| Mechanical properties of Araneus diadematus dragline silk, eADF4 single fibers and fiber bundles. Exemplary stress-strain curves of a) as spun and b) post-treated eADF4 fiber bundles (measured by tensile testing). Force-deformation curves of eADF4 single fibers (measured by lateral AFM bending) in the c) as spun

(AS) and d) post-treated (PT) state. e) Increasing of RH softened all fibers reducing the Young's moduli. Dragline silk overall retained its strength and extensibility throughout the humidity range (f, g) whereas PT eADF4 fiber bundles and single fibers show a significant increase in extensibility at 80 % RH. This behavior leads to a similar toughness of dragline silk and single PT eADF4 fibers at 80 % RH (h). The data at 30 % RH are in the same range as compared to the dry state which indicates a humidity driven glass transition as studied by Plaza et al.[21]

References

1. Vollrath F, Knight DP. Liquid crystalline spinning of spider silk. *Nature* 2001, **410**(6828)**:** 541-548.

2. Humenik M, Scheibel T, Smith A. Spider silk: understanding the structure-function relationship of a natural fiber. *Progress in molecular biology and translational science* 2011, **103:** 131-185.

3. Liu Y, Shao ZZ, Vollrath F. Relationships between supercontraction and mechanical properties of spider silk. *Nat Mater* 2005, **4**(12)**:** 901-905.

4. Gosline JM, Guerette PA, Ortlepp CS, Savage KN. The mechanical design of spider silks: From fibroin sequence to mechanical function. *J Exp Biol* 1999, **202**(23)**:** 3295-3303.

5. Keten S, Buehler MJ. Nanostructure and molecular mechanics of spider dragline silk protein assemblies. *Journal of the Royal Society Interface* 2010, **7**(53)**:** 1709-1721.

6. Keten S, Xu ZP, Ihle B, Buehler MJ. Nanoconfinement controls stiffness, strength and mechanical toughness of beta-sheet crystals in silk. *Nat Mater* 2010, **9**(4)**:** 359-367.

7. Sponner A, Vater W, Monajembashi S, Unger E, Grosse F, Weisshart K. Composition and Hierarchical Organisation of a Spider Silk. *PLoS One* 2007, **2**(10).

8. Heim M, Keerl D, Scheibel T. Spider Silk: From Soluble Protein to Extraordinary Fiber. *Angew Chem-Int Edit* 2009, **48**(20)**:** 3584-3596.

9. Rising A, Johansson J. Toward spinning artificial spider silk. *Nat Chem Biol* 2015, **11**(5)**:** 309-315.

10. Vehoff T, Glisovic A, Schollmeyer H, Zippelius A, Salditt T. Mechanical properties of spider dragline silk: Humidity, hysteresis, and relaxation. *Biophys J* 2007, **93**(12)**:** 4425-4432.

11. Agnarsson I, Boutry C, Wong SC, Baji A, Dhinojwala A, Sensenig AT*, et al.* Supercontraction forces in spider dragline silk depend on hydration rate. *Zoology* 2009, **112**(5)**:** 325-331.

12. Huemmerich D, Helsen CW, Quedzuweit S, Oschmann J, Rudolph R, Scheibel T. Primary Structure Elements of Spider Dragline Silks and Their Contribution to Protein Solubility†. *Biochemistry* 2004, **43**(42)**:** 13604-13612.

13. Lang G, Jokisch S, Scheibel T. Air filter devices including nonwoven meshes of electrospun recombinant spider silk proteins. *Journal of visualized experiments : JoVE* 2013(75)**:** e50492-e50492.

14. Leal-Egana A, Lang G, Mauerer C, Wickinghoff J, Weber M, Geimer S*, et al.* Interactions of Fibroblasts with Different Morphologies Made of an Engineered Spider Silk Protein. *Adv Eng Mater* 2012, **14**(3)**:** B67-B75.

15. Drummy LF, Phillips DM, Stone MO, Farmer BL, Naik RR. Thermally induced alpha-helix to beta-sheet transition in regenerated silk fibers and films. *Biomacromolecules* 2005, **6**(6)**:** 3328-3333.

16. Hu X, Kaplan D, Cebe P. Determining beta-sheet crystallinity in fibrous proteins by thermal analysis and infrared spectroscopy. *Macromolecules* 2006, **39**(18)**:** 6161-6170.

17. Neugirg BR, Koebley SR, Schniepp HC, Fery A. AFM-based mechanical characterization of single nanofibres. *Nanoscale* 2016, **8**(16)**:** 8414-8426.

18. Hudson SD, Zhurov V, Grbic V, Grbic M, Hutter JL. Measurement of the elastic modulus of spider mite silk fibers using atomic force microscopy. *J Appl Phys* 2013, **113**(15)**:** 154307.

19. Heidebrecht A, Eisoldt L, Diehl J, Schmidt A, Geffers M, Lang G*, et al.* Biomimetic Fibers Made of Recombinant Spidroins with the Same Toughness as Natural Spider Silk. *Adv Mater* 2015.

20. Schafer A, Vehoff T, Glisovic A, Salditt T. Spider silk softening by water uptake: an AFM study. *European Biophysics Journal with Biophysics Letters* 2008, **37**(2)**:** 197-204.

21. Plaza GR, Guinea GV, Perez-Rigueiro J, Elices M. Thermo-hygro-mechanical behavior of spider dragline silk: Glassy and rubbery states. *J Polym Sci Pt B-Polym Phys* 2006, **44**(6)**:** 994-999.

22. Hu YP, Zhang Q, You RC, Wang LS, Li MZ. The Relationship between Secondary Structure and Biodegradation Behavior of Silk Fibroin Scaffolds. *Advances in Materials Science and Engineering* 2012, **2012:** 5.

23. Smith JF, Knowles TPJ, Dobson CM, MacPhee CE, Welland ME. Characterization of the nanoscale properties of individual amyloid fibrils. *Proc Natl Acad Sci U S A* 2006, **103**(43)**:** 15806-15811.

24. Guo SL, Akhremitchev BB. Packing density and structural heterogeneity of insulin amyloid fibrils measured by AFM nanoindentation. *Biomacromolecules* 2006, **7**(5)**:** 1630-1636.

25. Slotta U, Hess S, Spiess K, Stromer T, Serpell L, Scheibel T. Spider silk and amyloid fibrils: A structural comparison. *Macromolecular Bioscience* 2007, **7**(2)**:** 183-188.

26. Knowles TPJ, Buehler MJ. Nanomechanics of functional and pathological amyloid materials. *Nat Nanotechnol* 2011, **6**(8)**:** 469-479.

27. Schleeger M, vandenAkker CC, Deckert-Gaudig T, Deckert V, Velikov KP, Koenderink G*, et al.* Amyloids: From molecular structure to mechanical properties. *Polymer* 2013, **54**(10)**:** 2473-2488.

28. Hagn F, Eisoldt L, Hardy JG, Vendrely C, Coles M, Scheibel T*, et al.* A conserved spider silk domain acts as a molecular switch that controls fibre assembly. *Nature* 2010, **465**(7295)**:** 239-U131.

29. Cetinkaya M, Xiao SB, Markert B, Stacklies W, Grater F. Silk Fiber Mechanics from Multiscale Force Distribution Analysis. *Biophys J* 2011, **100**(5)**:** 1298-1305.

30. Spiess K, Ene R, Keenan CD, Senker J, Kremer F, Scheibel T. Impact of initial solvent on thermal stability and mechanical properties of recombinant spider silk films. *J Mater Chem* 2011, **21**(35)**:** 13594-13604.

31. Kluge D, Singer JC, Neubauer JW, Abraham F, Schmidt HW, Fery A. Influence of the Molecular Structure and Morphology of Self-Assembled 1,3,5-Benzenetrisamide Nanofibers on their Mechanical Properties. *Small* 2012, **8**(16)**:** 2563-2570.

32. Munz M. Force calibration in lateral force microscopy: a review of the experimental methods. *J Phys D-Appl Phys* 2010, **43**(6)**:** 063001.

33. Heidelberg A, Ngo LT, Wu B, Phillips MA, Sharma S, Kamins TI*, et al.* A generalized description of the elastic properties of nanowires. *Nano Lett* 2006, **6**(6)**:** 1101-1106.

34. Kontou E, Farasoglou P. Determination of the true stress-strain behaviour of polypropylene. *Journal of Materials Science* 1998, **33**(1)**:** 147-153.

IV.3 Long-Range Interaction Forces between 1,3,5-Cyclohexanetrisamide Fibers in Crossed-Cylinder Geometry

Reproduced with permission from:

"Long-Range Interaction Forces Between 1,3,5-Cyclohexanetrisamide Fibers in Crossed-Cylinder Geometry", B.R. Neugirg, N. Helfricht, S. Czich, H.-W. Schmidt, G. Papastavrou, A. Fery, *Polymer*, **2016**, *102*, 363-371

© 2016 Elsevier Ltd

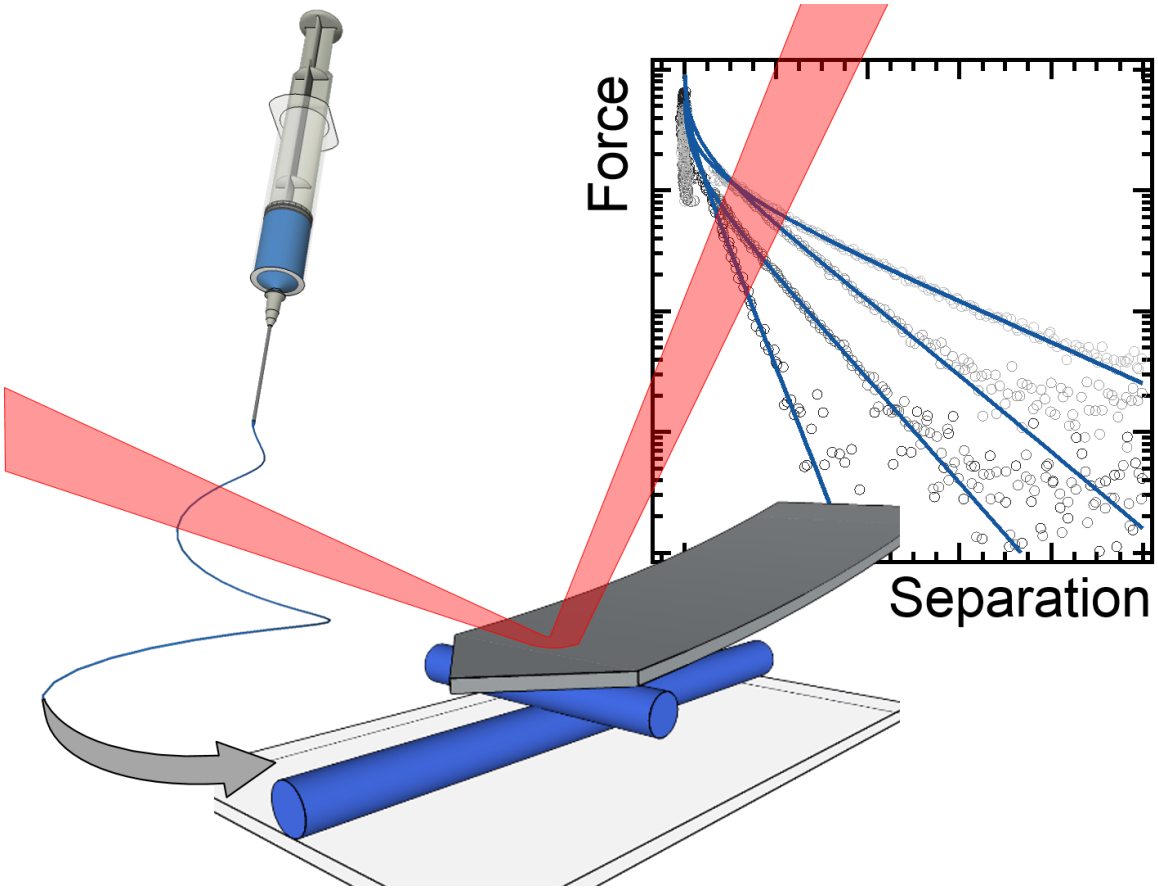

Abstract

We report on direct force measurements between single melt-electrospun 1,3,5-cyclohexanetrisamide (CTA) fibers in crossed-cylinder geometry. The two CTA compounds selected for this study differ in their peripheral substituents: aliphatic ($-C_{10}H_{21}$) and fluorinated chains ($-CH_2C_6F_{13}$), respectively. Melt-electrospinning of the CTAs results in smooth and circular fibers with diameters of about 5 µm. Individual segments of these fibers were attached to tipless atomic force microscope (AFM) cantilevers and used to measure long-range interaction forces versus a second fiber from the same compound in crossed-cylinder geometry. This geometry is well-known from the surface force apparatus and allows for the normalization of forces according to the Derjaguin approximation. From symmetrical measurements, i.e. measurements between fibers from the same type of CTA, we quantify the diffuse layer properties in aqueous electrolyte solutions within the framework of the Derjaguin, Landau, Verwey and Overbeek (DLVO) theory. Apparent diffuse layer potentials resulting from the fits to the full solutions of the Poisson-Boltzmann equation show that the fiber surfaces bear a negative surface charge. Most likely, the origin of charging is the adsorption of hydroxyl ions as residual charges from the electrospining process would be compensated upon the immersion in the electrolyte solutions. Such ion adsorption processes are well-known for other hydrophobic surfaces such as aliphatic and fluorinated self-assembled monolayers (SAMs) (terminating with $-CH_3$ and $-CF_3$ groups). The apparent diffuse layer potentials for CTA fibers are comparable to the values reported for these SAMs .

Introduction

The invention of the atomic force microscope (AFM) fundamentally changed the way how colloidal and soft matter systems can be studied in-situ.[1] In addition to the possibility of imaging a surface, one can also probe the interaction of an AFM tip with the sample by direct force measurements.[2] To overcome the problem of ill-defined contact, the colloidal probe (CP) technique was invented.[3] Typically, the CP-technique utilizes a spherical, µm-sized colloidal particle that replaces the sharp tip at the end of an AFM cantilever. The particle's dimensions can be determined with reasonable accuracy by optical or scanning electron microscopy (SEM). A CP allows for a well-defined interaction geometry, which on the one hand enables the determination of mechanical properties. In contact mechanics, one relates the force exerted by the CP on the sample and the resulting

deformation in the contact area. Thus, material properties such as Young's modulus and the work of adhesion per unit area can be obtained.[2, 4-6] On the other hand, a well-defined interaction geometry is the prerquisite to investigate long-range forces in colloidal suspensions in a quantitative manner.[7, 8] The Derjaguin approximation relates experimentally determined forces to free interaction energies per unit area.[9] Prior to the advent of CP, the only possibility to accomplish such direct force measurements was the surface force apparatus (SFA) which is based on the measurements of interaction forces between two smooth macroscopic mica surfaces of cylindrical shape in crossed-cylinder geometry.[10, 11] This particular interaction geometry was first adapted to the AFM in 1998 by Meagher et al. and permitted to determine the interaction forces between α-alumina fibers in electrolyte solutions.[12, 13]

Utilizing fiber fragments as CPs represents an important experimental approach as fibrillar (cylindrical) systems are ubiquitous in nature. For instance in case of hair, the contact interactions, i.e. adhesive and frictional properties, dominate the haptics and are thus of great interest in the formulation of hair care products. To study these interactions, researchers attached hair fragments to tipless AFM cantilevers. Force versus distance ($F - D$) curves and lateral friction loops acquired in sliding contact with a second hair enabled the direct investigation of adhesion and friction on the level of single hairs for the first time.[14-16] Adhesion and friction also play an important role in many non-woven fabrics made from polymer fibers. A crucial factor for the stability and integrity in many networks is the junction strength of two fibers touching each other. Polyester[17] and pulp[18] microfibers as well as Nylon[19] nanofibers were studied in terms of their adhesive and frictional behavior.

Self-assembly processes provide the possibility to form micro- and nanofibers by a bottom-up approach via secondary interactions. Among the multitude of suitable supramolecular motifs, a well-known example are 1,3,5-benzenetrisamides (BTAs), which are capable of forming nanofibers. Typically, the formation of supramolecular nanofibers by these small molecules is driven by three uniaxially directed hydrogen bonds. AFM investigations on individual supramolecular objects unraveled a pronounced mechanical stability of these BTA-based micro- and nanofibers.[20, 21] Recently, we have reported on the in-situ formation of supramolecular nanofibers in a polymer nonwoven scaffold resulting in a remarkably stable microfiber-nanofiber composite. These composites, which exhibit a dense nanofiber network, are highly suitable to remove particulate matter from air and are thus promising to be used in air filtration applications.[22] However, a

fundamental understanding of the interaction forces between individual fibers in these composites is missing.

Besides fiber formation via self-assembly processes, BTAs can also be melt-electrospun into supramolecular micro- and nanofibers.[23] Electrospinning is a technique commonly used for fiber fabrication from viscous polymer solutions.[24] Under the influence of a strong electrical field, a thin jet is ejected from the so-called Taylor cone (see Figure 26).[25] Electrospinning of BTAs to homogenous[26] and mechanically stable[27] fibers with circular cross-section and smooth surfaces depends on various parameters such as molecular structure, temperature and viscosity of the melt, and the applied electric field. In this context, electrospinning of supramolecular fibers and avoiding the formation of solid spheres during the electrospinning process (i.e. electrospraying) is facilitated by using 1,3,5-cyclohexanetrisamides (CTAs) compared to BTAs.[26, 28]

Here, we investigate the interaction forces between individual melt-electrospun supramolecular fibers. We selected two distinct CTAs that differ significantly in the terminating functional groups at their periphery (Figure 26). In the alkyl CTA (Figure 26 left side), each amide group is linked to a decyl chain. In the fluorinated CTA (Figure 26 right side) the amide substituent consists of a methylene group followed by a perfluorinated C_6 chain. Due to the length of these pending chains, the outmost layer of the compounds can be considered as aliphatic or perfluorinated, respectively. By attaching CTA fiber fragments to AFM cantilevers and immobilizing a second fiber of the same compound on the substrate, we adapted the classical crossed-cylinder geometry from the SFA. Direct F-D measurements in these symmetric systems immersed in aqueous electrolyte solution of various concentrations allow for unambiguous identification of the fiber surface's interaction forces, including apparent diffuse layer potentials.[29]

Results and Discussion

Melt-Electrospun Cyclohexanetrisamide Fibers

Both CTAs have been obtained by the reaction of the cyclohexane-1,3,5-tricarboxylic acid chloride with the corresponding amines in THF in the presence of pyridine. Details of the synthesis for the alkyl CTA (Figure 26 left side) have been reported previously.[30, 31] The ones for the fluorinated CTA (Figure 26 right side) are given in the experimental section.

For melt-electrospinning, we utilized the same custom-made setup as described in detail by Singer et al.[28] Electrospinning of CTAs results in a jet that is sufficiently stable to obtain continuous fibers and thereby illustrates their strong inter-molecular cohesion.[26] Important for the successful melt-electrospinning to fibers is the knowledge of the thermal stability and the phase behavior of the CTAs (see Figure SI 2). Typically, electrospinning of BTAs from the isotropic phase results in the formation of solid droplets (electrospraying), whereas highly ordered mesophases are too viscous to perform electrospinning. However, CTAs feature columnar nematic phases readily allowing for fiber formation by melt-electrospinning. Both CTAs could be spun employing identical electrospinning parameters. The CTAs were placed into a glass syringe and equilibrated in the heating unit at 300 °C for 3 min. After this step a voltage of U = -30 kV was applied to spin fibers which were collected on top of an aluminum foil. Under these conditions, we obtained homogeneous and smooth fibers with a diameter in the range of 5 µm, which are well-suited for fiber manipulation and direct force measurements (Figure 26 bottom).

Melt-electrospun fiber segments can be immobilized on solid substrates by means of a UV-curable glue. Figure 27 compares tapping-mode AFM images in air of fibers from both compounds. Despite a pronounced convolution effect of the cylindrical fiber and the sharp AFM tip, there are no indications for the fiber cross-section to deviate from a circular shape. These observations are in perfect agreement with the SEM images (Figure 26 bottom).

The surfaces of both fiber types are smooth and defect-free. However, on the nm-level a pronounced ultrastructure can be observed: the topography of the alkyl CTA consists of elongated features with an overall root mean square (RMS) roughness of 4.1 ± 1.6 nm and an average peak-to-peak distance of 34.9 ± 11.7 nm (Figure 27 a). The drop-like ultrastructure in the case of the fluorinated CTA, leads to a significantly larger roughness (RMS: 16.4 ± 2.4 nm and peak-to-peak distance: 112 ± 29 nm) (Figure 27 b). These values for the roughnesses were derived from the residuals after a 3rd-order plane fit to remove the surface curvature from the 2x2 µm images. The roughnesses determined for the fibers here are slightly larger than the one reported for Al-fibers in the study of Meagher et al.[12, 13] Nevertheless, the overall circular cross-section and relative smoothness of melt-electrospun CTA fibers still allows for the determination of apparent diffuse layer potentials. The latter is the potential, as determined from fits to the full Poisson-Boltzmann equation at large separation distances, without any corrections for the surface roughness.

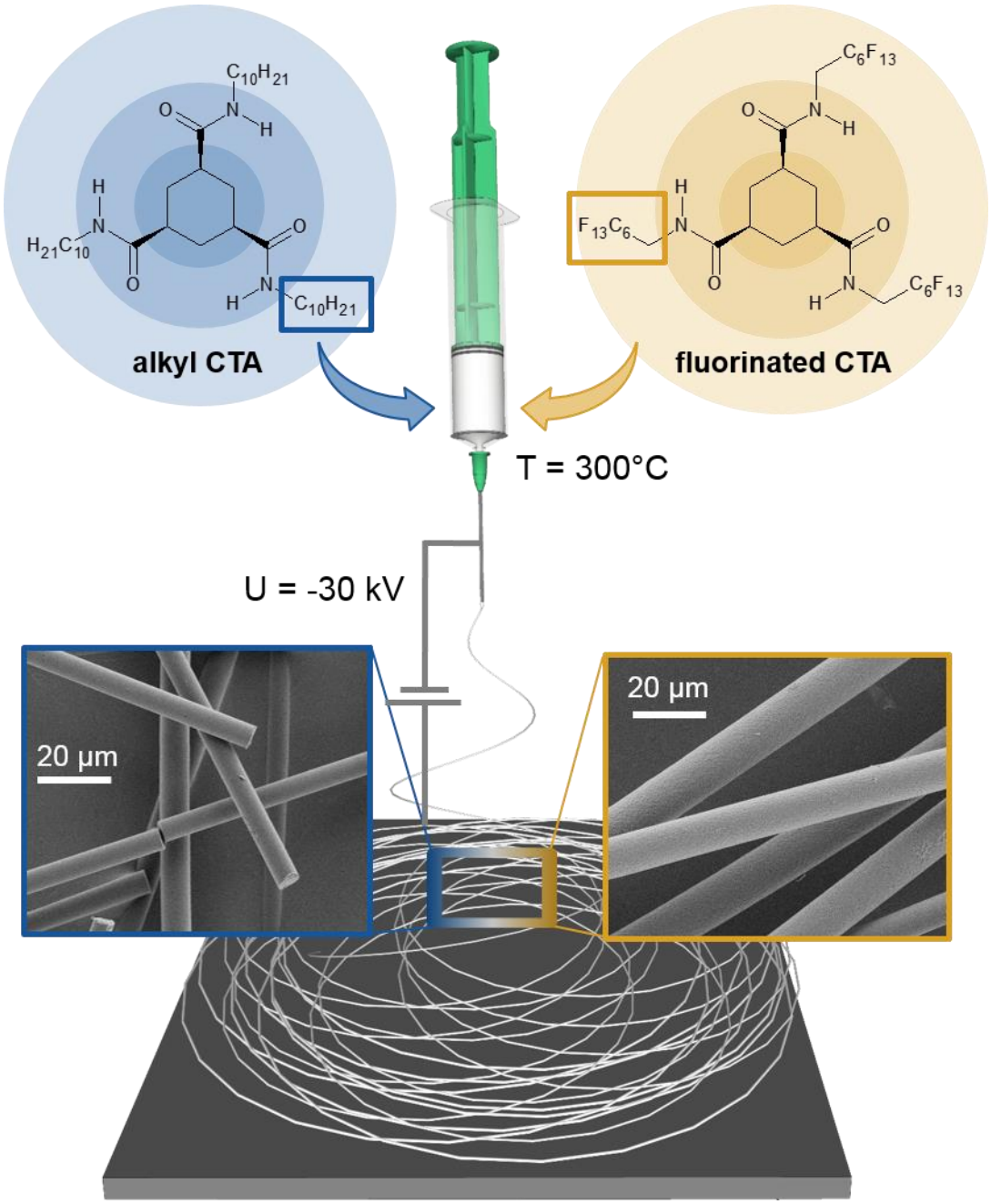

Figure 26| Schematic fabrication of 1,3,5-cyclohexanetrisamide (CTA) fibers by melt-electrospinning. The chemical structures of both CTAs consist of a cyclohexane core surrounded by three amide groups and peripheral aliphatic -$C_{10}H_{21}$ (left side) and fluorinated -$CH_2C_6F_{13}$ (right side) substituents, respectively. For both compounds, electrospinning from a melt at T = 300 °C at a voltage of -30 kV yields in continuous and homogeneous fibers with diameters in the range of 5 µm as verified by SEM.

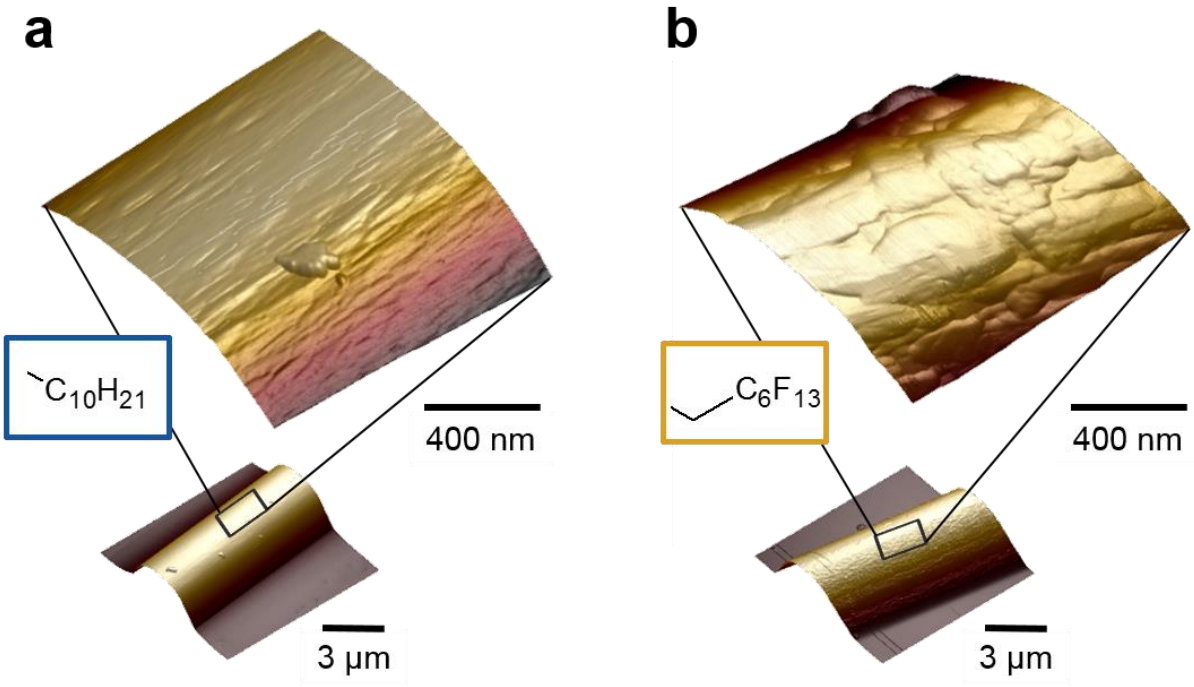

Figure 27| AFM tapping-mode images acquired in air depicting a fiber segment of the alkyl CTA (a) and the fluorinated CTA (b). The magnified sections show the morphology of the fiber surfaces. The RMS roughness of the topography is 4.1 ± 1.6 nm for the alkyl CTA and 16.4 ± 2.4 nm for the fluorinated CTA, respectively.

Direct Interaction Force Measurements in Crossed-Cylinder Geometry

We probed the long-range interaction forces between a symmetrical pair of CTA fibers by direct force measurements in crossed-cylinder geometry. This geometry follows the one used in the surface force apparatus (SFA).[10, 11] The bottom fiber is immobilized in the same manner as in the previous paragraph. For the probe, we prepared fiber segments attached to tipless AFM cantilevers by means of a micromanipulator. Here again, it is essential that the glue does not contaminate the future contact area of the fibers. Hence, a very thin film of the glue, which can be observed under an optical microscope was deposited on the cantilever. As indicated by the iridescence color due to interference effects, the film thickness can be assumed to be below 1 µm (Figure 28 a and b). During the preparation process, special diligence is necessary to avoid any rotation of the fiber segment about its long axis as this would inevitably contaminate the fiber surface. We verified additionally for a separate set of cantilevers by SEM that only the part of the fiber in contact with the cantilever

is wetted by glue (as highlighted by the yellow color in Figure 28 c and d). We found also by SEM no indication for any glue residues on the lower surface of the fiber fragments for which we report the interaction forces. This set of cantilevers were not used for any interaction measurements due to the metal coating necessary for SEM imaging.

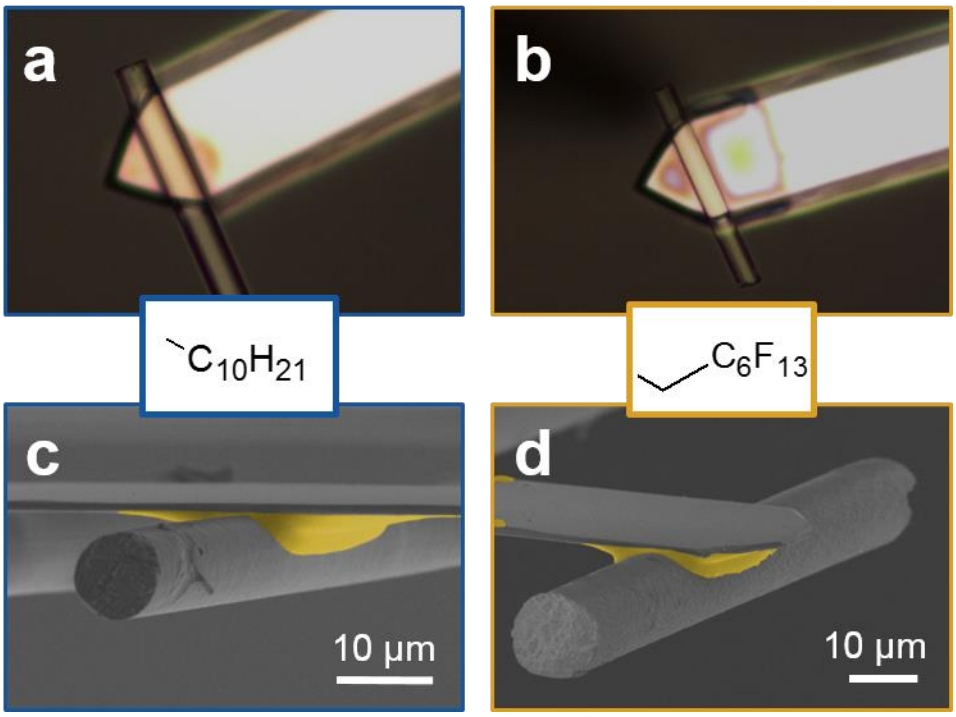

Figure 28| Fragments of the alkyl (a and c) and the fluorinated CTA (b and d) fibers attached to tipless AFM cantilevers. a and b show optical bottom view micrographs acquired during the micromanipulation process. The area of the cantilever covered in glue can be recognized by its darker shade and the iridescence color. c and d show SEM images for a different set of cantilevers prepared by an identical procedure. SEM confirms that no glue residues are present on the lower surface of the fiber fragments (c and d). The glue is highlighted by the yellow color.

We determined the interaction forces only for symmetric combinations of two aliphatic or two fluorinated CTA fibers, respectively. The measurements were carried out in aqueous electrolyte solutions of pH 5.5 and varying ionic strength (nominal NaCl concentrations 0.1, 0.5, 1 and 5 mM). The crossed-cylinder geometry applied for these measurements is schematically illustrated in Figure

29 a. In our setup, the AFM is combined with an inverted optical microscope, which we used to align the fibers perpendicular to each other (Figure 29 b). Furthermore, we determined the fiber radii optically and found them to be in the range of 4 – 8 µm. Diameters of about 5 µm are best suited for CP preparation and force measurements. The crossed-cylinder geometry has the advantage that it is self-adjusting, therefore, possible tilts of the cantilever would not influence the interaction geometry of two fibers. Due to the high lateral spring constant of the cantilever, torsional motion can be neglected in the examined force regime.

Our aim is to relate the forces measured between two fibers at perpendicular contact to their diffuse layer properties. In this quantitative analysis, a well-defined interaction geometry is essential: the Derjaguin approximation allows to relate the measured interaction forces *F* at a separation distance *D* with the free interaction energy $W(D)$ at the same separation.[9] Analytical expressions for the normalization of several interaction geometries exist, e.g. sphere/plane, sphere/sphere and two crossed cylinders.[11] *Equation 17* gives the corresponding approximation for two crossed cylinders of radii R_1 and R_2 and the effective radius R_{eff}.

$$F_{cylinder}(D) = 2\pi \cdot \sqrt{R_1 R_2} \cdot W(D) = 2\pi \cdot R_{eff} \cdot W(D) \qquad \textit{Equation 17}$$

Figure 28 c and d show representative force versus distance profiles acquired during approach in crossed-cylinder geometry. The interaction forces have been normalized to the effective radius for the crossed-cylinder geometry (according to *Equation 17*) and are represented in semi-logarithmic graphs. The retract part of the curves is omitted as we want to focus on long-range electrostatic interactions in the following.

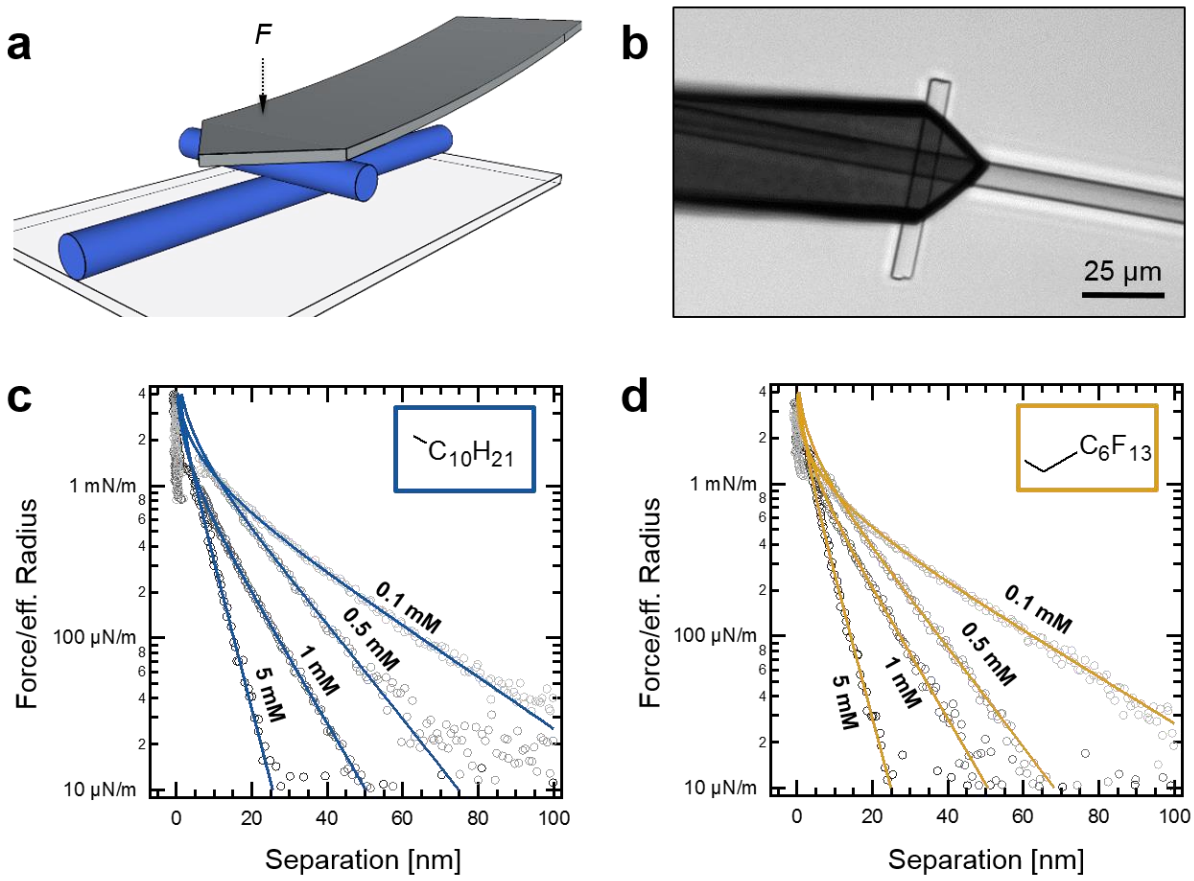

Figure 29| Schematic representation of the crossed-cylinder measurement configuration (a) and optical micrograph during the experiment (b). Representative approach F-D curves normalized to the crossed-cylinder geometry for the alkyl (c) and the fluorinated CTA (d) show a decrease of electrostatic interaction with increasing nominal electrolyte (NaCl) concentration.

In an AFM experiment, conversion of the photo-diode signal to forces requires the inverse optical lever sensitivity ($InvOLS$) and the effective cantilever spring constant k_{eff}. In the case of the fiber-CP, the determination of these two parameters is non-trivial. To account for possible thermal drifts during a measurement session, we determined the $InvOLS$ for each fiber-fiber approach curve individually from the constant compliance regime. The exclusion of any mechanical deformations in the applied force regime has been verified by reference measurements with a hard spherical silica colloidal probe (see Figure SI 4 for details). The cantilever spring constant k was calibrated by the thermal noise method.[32] It has to be corrected due to off-end loading as the fiber is attached a

certain distance ΔL away from the cantilever's free end at L (see scheme in Figure SI 5). The effective spring constant k_{eff} accounting for the apparent cantilever stiffening due to the shift in the contact point is given by:[33]

$$k_{eff} = k \cdot \left(\frac{L}{L - \Delta L}\right)^3 \qquad \textit{Equation 18}$$

All measurements were performed in electrolyte solutions with a total ionic strength (0.1, 0.5, 1 and 5 mM) adjusted by addition of NaCl. The Debye length κ^{-1} for an ionic strength of c_0 is given by *Equation 19*.[11]

$$\kappa = \sqrt{\frac{2 \cdot e^2 \cdot c_0}{\varepsilon\varepsilon_0 \cdot k_B T}} \qquad \textit{Equation 19}$$

where $\varepsilon\varepsilon_0$ is the total permittivity of the medium, $k_B T$ the thermal energy and e the elementary charge. At large separation distances the interaction force decays exponentially with κ^{-1} as decay constant. In the semi-logarithmic representation of Figure 29 c and d such a decay results in a linear dependency.

For a symmetric system of two identical materials, the total interaction energy $W(D)$ is given by two contributions: the diffuse layer overlap W_{DL} and the van-der-Waals W_{vdW} force according to Derjaguin, Landau, Verwey and Overbeek (DLVO) theory. However, this assumes ideal, smooth surfaces. At large separation distances W_{DL} dominates the interaction and the diffuse layer potential ψ_0 can be obtained from fits to the Poisson-Boltzmann theory. The van-der-Waals forces are generally much shorter ranged. Thus, for rough surfaces, a general expression for the interaction energy as function of separation is extremely difficult to determine, in particular when the decay length of the interaction is of the same order as the surface roughness. Despite different studies,[34-36] no consistent theory has been established to date as standard approach in order to account for the effects of surface roughness in direct force measurements, especially regarding non-contact forces.

The CTA fibers that we study here have a RMS surface roughness of several nm (cf. Figure 27), which is of the order of the Debye length. Due to the special interaction geometry of crossed cylinders, we do not apply any corrections for surface roughness. Instead, we state the apparent diffuse layer potential $\psi_{0,app}$ that results from the fits at large separation distances D (with $D > 10$ nm). An additional advantage is that thereby charge regulation can be neglected and, moreover, also the van

der Waals forces are reduced due to the surface roughness. We did not take these forces into account for data fitting. The interaction force profiles were fitted at large separation distances (D > 10 nm) and the Hamaker constants of hydro- and fluorocarbons in water are relatively small. Hence, we found very similar surface potentials when theoretical Hamaker constants for both fibers have been considered (data not shown).

The solid lines in Figure 29 c and d represent fits to full solutions of the Poisson-Boltzmann equation under the boundary condition of constant charge.[29] The Debye length resulting from these fits is in good agreement with the one calculated based on the nominal ionic strength (cf. *Equation 19* and Figure SI 3). However, deviations at low ionic strength are expected due to dissolution of CO_2 as reported previously.[37]

From symmetric $F - D$ measurements, two positively or two negatively charged surfaces are indistinguishable as they would give the same repulsive W_{DL}. Due to the symmetric combination of fibers investigated here, the sign of the apparent diffuse layer potential $\psi_{0,app}$ has to be verified in a separate set of measurements. Hence, we utilized the CP technique with a spherical silica particle that is well-known to be negatively charged in aqueous media.[3, 38] A schematic representation of the measurement with the silica colloidal probe and a fiber segment is shown in Figure 30 a. A corresponding optical micrograph is given in Figure 30 b. In the fiber-fiber experiments described above, the interaction forces were normalized to the effective radius for two crossed cylinders, which is well known from the Derjaguin approximation. However, in the case of a sphere-cylinder geometry no analytical expression is available and interaction potentials would have to be calculated numerically.[39-41] Therefore, the force profiles in Figure 30 c and d are only given as force versus separation and not normalized with respect to the interaction geometry. Figure 30 c and d show interaction force profiles at three consecutive spots (2 µm apart) for the silica colloidal probe measured against an alkyl-terminated and a fluorinated CTA fiber, respectively. We repeated these measurements in several regions along the bottom fibers. In every case, the resulting interaction forces are completely repulsive, which confirms that both fiber types are negatively charged. Several previous studies reported negative potentials for hydrophobic surfaces in aqueous solutions.[42-44] We found the force profiles to be highly reproducible showing almost no deviations from spot to spot indicating an absence of charge heterogeneities on the scale of the resolution achievable by a µm-sized probe (Figure 30 c and d).

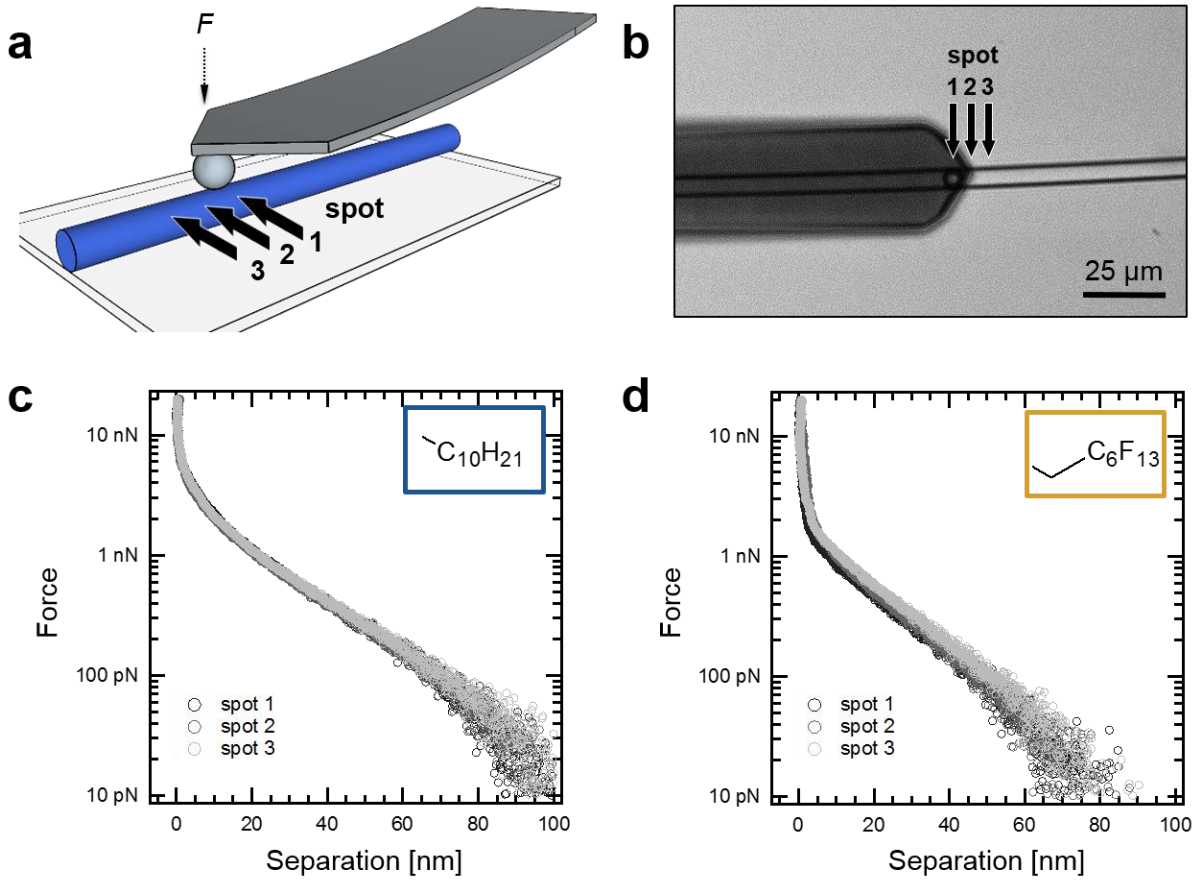

Figure 30| Schematic representation of the sphere-cylinder measurement configuration (a) and optical micrograph during the experiment (b). Representative approach F-D curves for the alkyl (c) and the fluorinated CTA (d) show purely repulsive forces irrespective of the fiber type and position on the fiber.

Figure 31 summarizes the results for $\psi_{0,app}$ as obtained from fits to the full Poisson-Boltzmann equation. In this graph $\psi_{0,app}$ is plotted against the ionic strength as determined from the same set of fits (derived from fitted κ^{-1} values). In order to account for the variations in the measurement, the following representation has been chosen: each lightly colored data point corresponds to the average from fitting of 30 $F-D$ curves of a fiber CP-probe at three spots on a bottom fiber. The average of one top-bottom fiber combination is shown as the intermediate color shade. The overall average of all fiber-fiber pairs for one ionic strength is presented in the darkest shade. Figure 31 a is based on measurements of 10 different alkyl fiber-fiber pairs (2 independent fiber probes versus 5 independent bottom fibers) and Figure 31 b on the results of 8 different fluorinated fiber-fiber pairs

(2 independent fiber probes versus 4 independent bottom fibers) at 4 different electrolyte concentrations (0.1, 0.5, 1 and 5 mM), respectively.

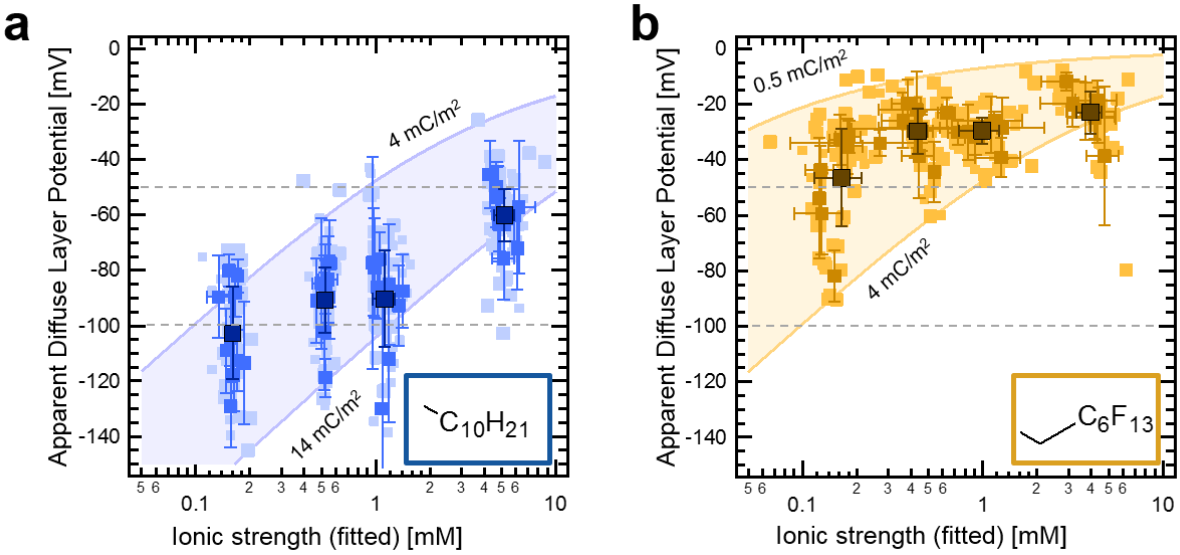

Figure 31| Fitted apparent diffuse layer potentials as a function of the fitted ionic strength for the alkyl (a) and the fluorinated CTA (b). The limits for the resulting surface charge density as calculated by the Grahame equation are indicated by the solid lines.

We found apparent diffuse layer potentials of the alkyl CTA in the range of - 50 to - 120 mV and for fluorinated CTA between - 20 and - 50 mV. Hence, the charge of fibers with alkyl periphery exceeds the one of the fluorinated CTA over the whole investigated range of ionic strengths. The decline of the absolute potential with increasing ionic strength is in accordance with the Gouy-Chapman theory. The Grahame equation relates the previously determined diffuse layer potential $\psi_{0,app}$ and the surface charge density σ_{app} (*Equation 20*), where the index "app" indicates again that the resulting charge density is not necessarily the true surface charge density of the rough surface.

$$\sigma_{app} = \sqrt{8c_0\varepsilon\varepsilon_0 RT}\sinh\left(\frac{ze\psi_{0,app}}{2k_BT}\right) \qquad \textit{Equation 20}$$

where *R* denotes the universal gas constant and *z* is the charge number.

The solid lines in Figure 31 indicate an approximate range for σ_{app} of the CTA fibers. We found σ_{app} roughly between 4 and 14 mC/m^2 for aliphatic and between 0.5 and 4 mC/m^2 for fluorinated fibers.

It should be pointed out additionally that even at large ionic strength and thus small Debye-lengths smaller values for the fluorinated fibers have been found. Under these conditions surface roughness should influence $\psi_{0,app}$ and thus σ_{app} to a much smaller degree.

Electrospun fibers loose their residual charges from the electrospinning process upon immersion in electrolyte solutions. Hence, these residual charges are not responsible for the observed surface charge. As both CTA fiber types are lacking ionizable groups on their surface, the proposed mechanism for charge generation on these hydrophobic surfaces is the asymmetric adsorption of water ions. Especially hydroxide ions have been shown to adsorb preferentially onto hydrophobic surfaces.[45] Studies on undecanethiol self-assembled monolayers (SAMs) as well as Teflon AF thin films showed an isoelectric point at about pH 4.[42] The pH range in our measurements is 5.5 – 5.8 and is thus compatible with a negative surface charge. For SAMs from undecanethiol zeta potentials between - 30 and - 50 mV have been reported.[42] Also for alkyl SAMs negative diffuse layer potentials have been found in this pH-range, albeit lower than the apparent ones determined here for the alkyl CTA fibers.[43, 46] The potentials for Teflon surfaces were generally lower and range from - 20 to - 30 mV (at 1 mM and pH 5).[42] In another study based on direct force measurements between a silica colloidal probe (RMS roughness: 10 – 15 nm) against Teflon AF, diffuse layer potentials have been reported: with ψ_0 = - 50 to - 40 mV for 0.1 mM and around - 15 mV for 1 mM of aqueous KCl solutions at approximately the same pH. These agree reasonably well with the apparent diffuse layer potentials obtained here.[44]

A model by Lützenkirchen et al. based on sum frequency vibrational spectroscopy and molecular dynamics simulations reasonably reproduces the results of reference [47] and states that the surface charge density at the location of the first water layer for Teflon is 1.4 mC/m^2.[48] This result is in very good agreement with the results for fibers from the fluorinated CTA reported here.

Conclusion

Direct force measurements between electrospun fibers from two different types of 1,3,5-cyclohexanetrisamides (CTA) allowed to determine the diffuse layer properties of these fibers in electrolyte solutions. We selected two CTAs featuring either alkyl or fluorinated substituents on their periphery. Despite the absence of ionizable groups we found a negative surface charge, which originates most likely from the hydrophobic character of both CTAs, leading to the adsorption of

hydroxide ions in aqueous media. The direct force measurements reveal lower apparent surface charge densities for fibers from the fluorinated CTA (approx. 0.5 – 4 mC/m^2) as compared to fibers from its aliphatic counterpart (approx. 4 – 14 mC/m^2). A comparable difference has also been observed for fluorinated and alkyl SAMs in previous studies.

This study demonstrates that the adsorption of ions is also highly relevant for the effective surface charge of fibers. While this effect has been known and studied for flat surfaces (e.g. Refs [42, 43, 46]) it has to the best of our knowledge not been studied so far for fibers. By measuring interaction forces between fibers in the crossed-cylinder geometry and symmetrical fiber combinations many uncertainties of streaming potential measurements, especially for fibrous systems can be avoided. As many fibrous materials are exposed to electrolyte solutions we believe that determining surface charge properties by direct force measurements of single fibers should be especially useful in understanding adsorption phenomena. This issue might be for example of fundamental interest concerning the adsorption of water contaminants to microplastics on fibers. Direct force measurements between fibers might not only provide important insights in the underlying interaction forces for fiber systems, as it has been the case for colloidal interactions but provide also the basis for an optimization of fibers towards specific applications.

Experimental Section

Synthesis of 1,3,5-Cyclohexanetricarboxamides: NMR data were recorded on a Bruker Avance 300 spectrometer at 300.1 MHz at room temperature. Mass spectrometry was conducted on a Finnigan MAT 8500 GC/MS. Thermogravimetric analysis was performed with a Mettler SDTA 851 TGA at 10 K min^{-1}. Phase-transition temperatures were determined using a Perkin–Elmer Diamond DSC with a heating rate of 10 K min^{-1} under N_2. XRD measurements were carried out in the range θ=0.5–15° from room temperature to 250°C on a Huber Guinier diffractometer 600 equipped with a Huber germanium monochromator 611 to get Cu$K_{\alpha 1}$ radiation (λ=154.05 pm).

The synthesis and characterization of N,N',N''-tris(decyl)-cis,cis-1,3,5-cyclohexanetricarboxamide (alkyl CTA) is described in detail elsewhere.[31]

N,N',N''-tris(tridecafluoroheptyl)-cis,cis-1,3,5-cyclohexanetricarboxamide was prepared in a two-step synthesis. In a first step, cis,cis-1,3,5-cyclohexanetricarboxylic acid chloride were obtained by

adding 2.66 g of oxalyl chloride dropwise at 0 °C under nitrogen to a suspension consisting of 20 mL of anhydrous dichloromethane, 1 mL of dimethylformamide, and 0,73 g of cis,cis-1,3,5-cyclohexanetricarboxylic acid. The reaction mixture was stirred for 12 h at room temperature and 1 h at 50 °C. After cooling to room temperature the remaining oxalyl chloride and the solvents were evaporated. The obtained solid was used without further purification. In a second step, 3.9 g of tridecafluoroheptane-1-amine was added at 0 °C under inert gas to a mixture consisting of 40 mL of anhydrous tetrahydrofurane (THF), 0.9 mL of pyridine, and 0.91 g of cyclohexane-1,3,5-tricarboxylic acid chloride. The reaction mixture was allowed to warm to room temperature and was subsequently stirred for 24 h at 60 °C. After cooling to room temperature the solution was precipitated in ice water. The precipitate was filtered off, dried under vacuum and purified by recrystallization several times from an isopropanol/THF mixture and THF, respectively. 2.6 g (66%) of the fluorinated CTA was obtained as white solid.

^{1}H-NMR ($CF_3COOD/CDCl_3$ 5:1): δ = 1.72-1.84 (m, 3H), 2.23-2.27 (m, 3H), 2.63 (t, 3H), 4.04 (t, 6H) ppm. MS: 1209 (M+ 11); 1191 (45); 863 (55); 836 (100); 485 (38); 457 (70); 447 (19); 432 (34); 411 (12); 377 (12); 110 (30); 81 (39) m/z (%).

Melt-Electrospinning: For electrospinning, a custom-made setup was used as described previously in detail.[23, 26] The corresponding CTAs were placed into a glass syringe and heated at 300 °C for 3 min. After the annealing step, a voltage of U = -30 kV over the distance of 6 cm and a flow rate of 500 µL/h was applied. The fibers were collected with an aluminum foil. SEM samples were carbon-coated utilizing a MED 010 coating machine from Baltzer. SEM imaging of freshly electrospun CTA fibers was performed with a Zeiss LEO 1530 FESEM instrument (Zeiss, Jena, Germany) at 3 kV.

Cantilever and Substrate Preparation: Using an AFM (MFP-3D, Asylum Research, Santa Barbara, California), uncoated and tipless cantilevers (CSC37, µmasch, Sofia, Bulgaria) were calibrated in air according to the thermal noise method.[32] Cantilevers with spring constants ranging from 0.262 to 0.317 N/m were treated with oxygen plasma and transferred to a micromanipulation setup (DC-3 KS, Märzhäuser, Wetzlar, Germany). A µm-sized droplet of a UV-curable glue (Norland Optical Adhesives No. 63, Norland Products, Cranbury, New Jersey) was placed at the free end of each cantilever using an etched tungsten wire and under optical control (Axio Examiner.D1, Zeiss, Jena, Germany). Due to the glue's limited spread (below 10 % of the cantilever length) and its significantly smaller Young's modulus (< 2 GPa) compared to the silicon cantilever material (169 GPa), we assumed the shift in the cantilever spring constant negligible. Employing a different tungsten wire,

fragments of fractured melt-electrospun CTA fibers with diameters from 4.4 to 8 µm were positioned in the spreaded glue droplet. Thereby special care was taken to prevent any fiber rotation that could contaminate the fiber surface. The silica CP cantilever was prepared as reported previously.[49] The flawlessness of the preparation procedure was verified by SEM imaging (Zeiss LEO 1530 FESEM, Zeiss, Jena, Germany). Accordingly, we glued fibers of both CTAs to the surface of a glass disk that is forming the bottom of the fluid cell in the force measurements.

AFM Imaging: The surface morphology of immobilized fiber segments was investigated by AFM imaging (Dimension Icon, Bruker, Billerica, Massachusetts) utilizing an OTESPA-R3 (Bruker, Billerica, Massachusetts).

Force Measurements: For the measurements, we equipped the combined setup of the AFM (MFP-3D, Asylum Research, Santa Barbara, California) and an inverted optical microscope (Axio Observer Z1, Zeiss, Jena, Germany) with a fiber probe cantilever and optically aligned the fiber probe ("top fiber") and the fiber immobilized on the substrate ("bottom fiber") in crossed-cylinder geometry perpendicular to each other. All measurements were performed in solutions (0.1, 0.5, 1 and 5 mM) of NaCl (Bernd Kraft GmbH, Duisburg, Germany) in Milli-Q water of pH 5.5 – 5.8. For every symmetric combination of top and bottom fibers we recorded 30 force-distance (F-D) curves at 6 different spots along the long axis of the bottom fiber. In each F-D curve, the cantilever velocity was 500 nm/s and the force setpoints were between 10 and 25 nN. In this force regime, torsional cantilever movements upon fiber-fiber contact can be excluded. We interpreted the constant compliance regime as the fibers in contact defining the point of zero separation. In total, we analyzed the combinations of 2 top and 5 bottom fibers for the aliphatic compound (>7000 F-D curves) and 2 top and 4 bottom fibers for the fluorinated compound (>5000 F-D curves).

The data was evaluated using a custom-written program in FORTRAN and IGOR Pro (WaveMetrics, Inc., Lake Oswego, Oregon).[29] Fitting each F-D curve to the DLVO-theory yielded the apparent surface potential and, additionally, the Debye length as internal reference.

Acknowledgements

This work received financial support from the German Research Foundation (Deutsche Forschungsgemeinschaft) within the SFB 840 (projects B8 and C4, respectively). BRN acknowledges

the support of the Elite Network of Bavaria. The authors thank Carmen Kunert for her support with the SEM images and Dr. Klaus Kreger for his help with the manuscript.

Supporting Information

CTA Phase Behavior

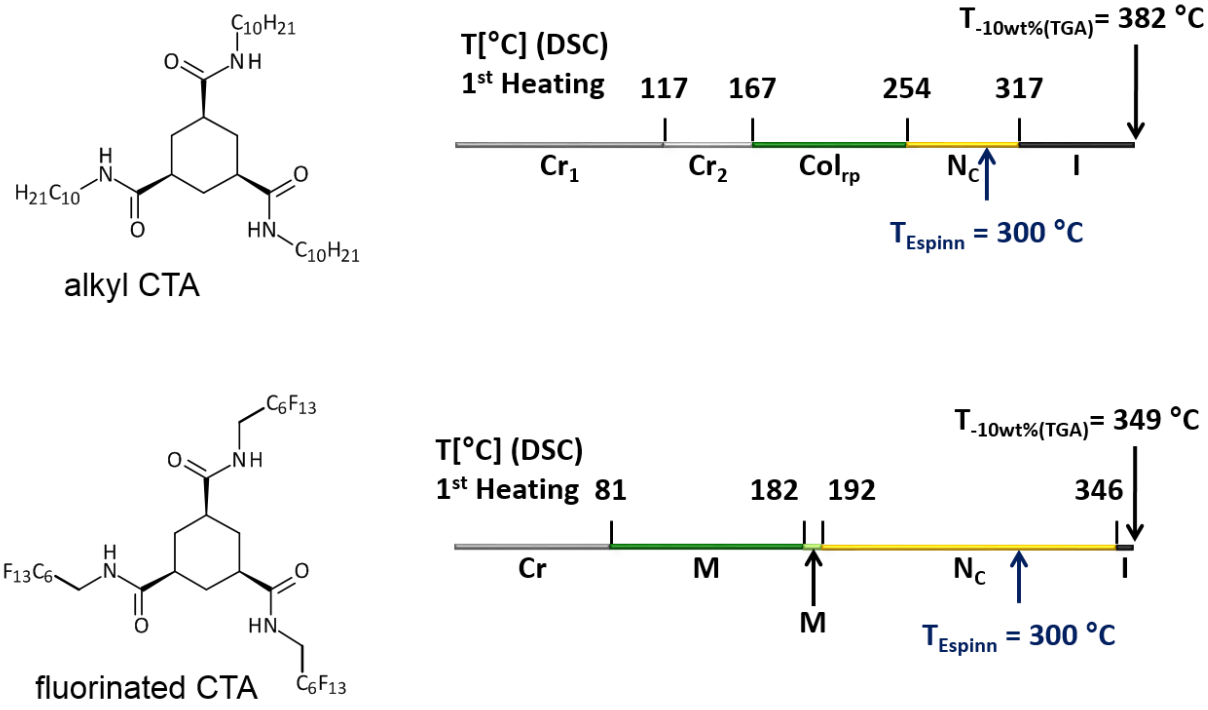

Figure SI 2| Schematic illustration of the phase behavior of the alkyl CTA and the fluorinated CTA as determined by differential scanning calorimetry (1st heating scan, 10 K/min, under N_2). A combination of DSC, X-ray powder diffraction and polarization microscopy were employed to assign the type of phase. The temperature at which a 10 wt% weight loss of the compounds were detected by means of thermogravimetric analysis and at which electrospinning was performed is indicated (Cr: crystalline, $Col_{rp:}$ columnar rectangular plastic, Nc, columnar nematic, I: isotropic, M: unidentified mesophase, N: nematic).

Salt Concentration

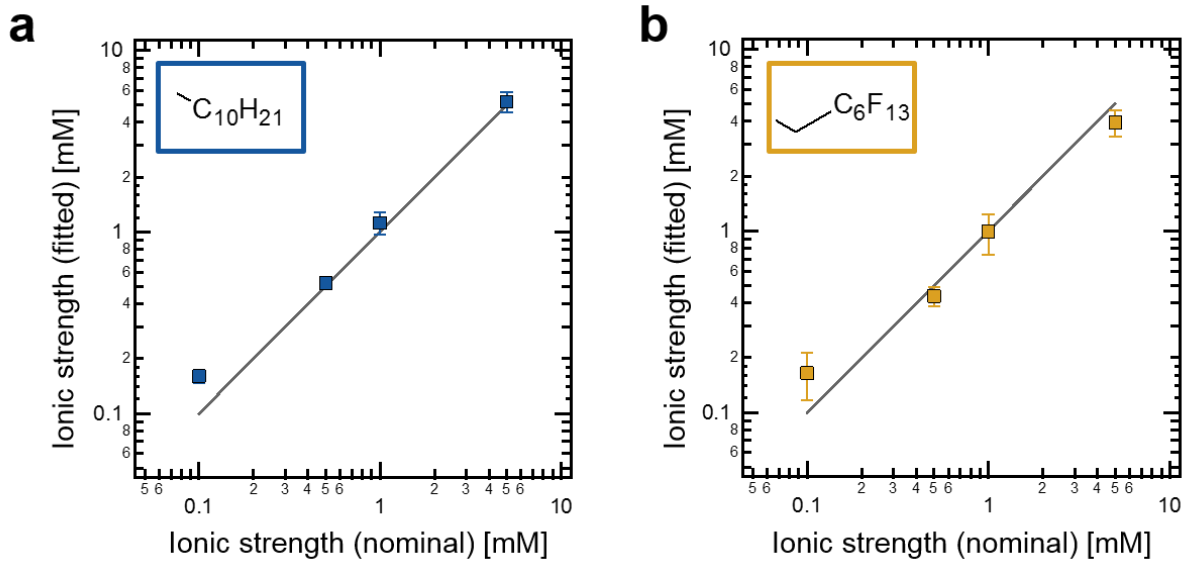

Figure SI 3| Fitted ionic strength as a function of the nominal ionic strength for the alkyl (a) and the fluorinated CTA (b). The gray line's slope is 1.

Figure SI 3 relates the nominal electrolyte concentrations to the ones derived from the Debye length as fitting parameter. The accordance is very good for both fiber types. The deviations at 0.1 mM ionic strength can be attributed to residual ions, e.g. from the dissolution of CO_2.[37]

Determination of the InvOLS

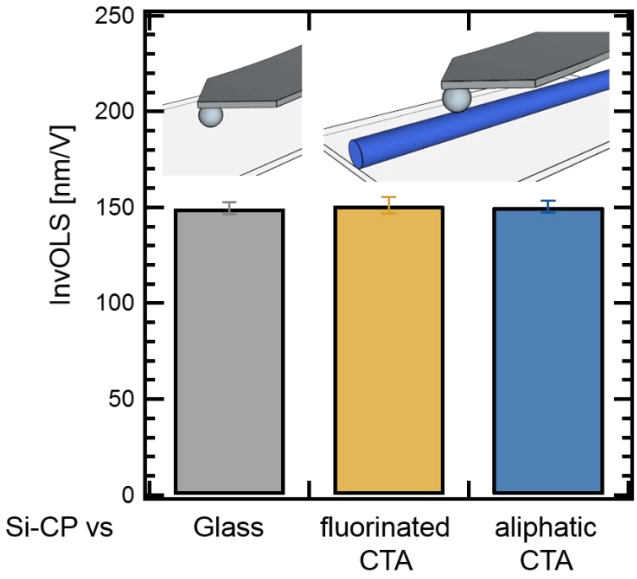

Figure SI 4| Inverse optical lever sensitivity (*InvOLS*) as determined for a cantilever decorated with a silica colloidal probe (SiCP) from three different approaches: SiCP vs glass substrate (gray), SiCP vs fluorinated CTA fiber (yellow) and SiCP vs aliphatic CTA fiber (blue). All three approaches give identical results for the *InvOLS* within experimental errors in the applied force regime.

We verified the absence of mechanical deformations in the applied force regime by the experiments depicted in Figure SI 4. Approaching a hard silica colloidal probe (SiCP) to the ("undeformable") glass substrate yields the pure cantilever deformation upon piezo extension in the constant compliance regime. From such an experiment, the $InvOLS$ is typically derived. Repeating the same experiment on a fluorinated or aliphatic CTA fiber, respectively, yields identical values for the $InvOLS$ within experimental errors. This consensus confirms the lack of mechanical deformation of the fibers in the applied force regime, i.e. in that range, the fibers can be assumed infinitely hard. Therefore, one can use the constant compliance regime in a fiber-fiber experiment to unambiguously deduce the $InvOLS$.

Effective Spring Constant k_{eff}

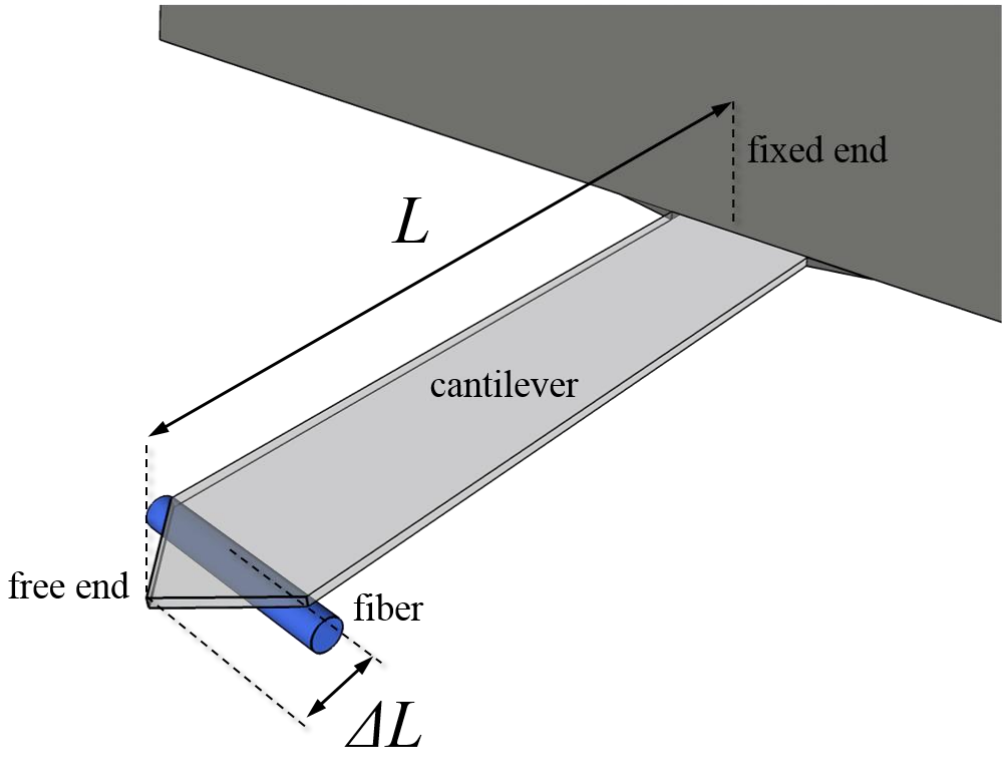

Figure SI 5| Scheme of a cantilever with a fiber attached. The total length $\boldsymbol{L}$ of the cantilever and the difference between the free end and the position where the fiber segment is situated $\boldsymbol{\Delta L}$ illustrate *Equation 18* which is used to calculate the effective spring constant $\boldsymbol{k_{eff}}$.

References

1. Binnig G, Quate CF, Gerber C. Atomic force microscope. *Phys Rev Lett* 1986, **56**(9)**:** 930-933.

2. Butt HJ, Cappella B, Kappl M. Force measurements with the atomic force microscope: Technique, interpretation and applications. *Surf Sci Rep* 2005, **59**(1-6)**:** 1-152.

3. Ducker WA, Senden TJ, Pashley RM. Measurement of forces in liquids using a force microscope. *Langmuir* 1992, **8**(7)**:** 1831-1836.

4. Erath J, Schmidt S, Fery A. Characterization of adhesion phenomena and contact of surfaces by soft colloidal probe AFM. *Soft Matter* 2010, **6**(7)**:** 1432-1437.

5. Neubauer MP, Poehlmann M, Fery A. Microcapsule mechanics: From stability to function. *Advances in Colloid and Interface Science* 2014, **207:** 65-80.

6. Butt HJ, Berger R, Bonaccurso E, Chen Y, Wang J. Impact of atomic force microscopy on interface and colloid science. *Adv Colloid Interfac* 2007, **133**(2)**:** 91-104.

7. Ducker WA, Senden TJ, Pashley RM. Direct measurement of colloidal forces using an atomic force microscope. *Nature* 1991, **353**(6341)**:** 239-241.

8. Butt HJ. Measuring electrostatic, vanderWaals, and hydration forces in electrolyte-solutions with an atomic force microscope. *Biophys J* 1991, **60**(6)**:** 1438-1444.

9. Derjaguin B. Untersuchungen über die Reibung und Adhäsion, IV. *Kolloid-Zeitschrift* 1934, **69**(2)**:** 155-164.

10. Israelachvili JN, Adams GE. Measurement of forces between 2 mica surfaces in aqueous-electrolyte solutions in range 0-100 nm. *Journal of the Chemical Society-Faraday Transactions I* 1978, **74:** 975-1001.

11. Israelachvili JN. Intermolecular and surface forces. 3rd ed. Amsterdam: Elsevier; 2011.

12. Meagher L, Franks GV, Gee ML, Scales PJ. Interaction forces between α-alumina fibres in aqueous electrolyte measured with an atomic force microscope. *Colloids and Surfaces A: Physicochemical and Engineering Aspects* 1999, **146**(1–3)**:** 123-137.

13. Muir I, Meagher L, Gee M. Interaction Forces between α-Alumina Fibers with Coadsorbed Polyelectrolyte and Surfactant. *Langmuir* 2001, **17**(16)**:** 4932-4939.

14. Max E, Hafner W, Bartels FW, Sugiharto A, Wood C, Fery A. A novel AFM based method for force measurements between individual hair strands. *Ultramicroscopy* 2010, **110**(4)**:** 320-324.

15. Mizuno H, Luengo GS, Rutland MW. Interactions between Crossed Hair Fibers at the Nanoscale. *Langmuir* 2010, **26**(24)**:** 18909-18915.

16. Mizuno H, Luengo GS, Rutland MW. New Insight on the Friction of Natural Fibers. Effect of Sliding Angle and Anisotropic Surface Topography. *Langmuir* 2013, **29**(19)**:** 5857-5862.

17. Mizuno H, Kjellin M, Nordgren N, Pettersson T, Wallqvist V, Fielden M*, et al.* Friction measurement between polyester fibres using the fibre probe SPM. *Aust J Chem* 2006, **59**(6)**:** 390-393.

18. Huang F, Li KC, Kulachenko A. Measurement of interfiber friction force for pulp fibers by atomic force microscopy. *J Mater Sci* 2009, **44**(14)**:** 3770-3776.

19. Stachewicz U, Hang F, Barber AH. Adhesion Anisotropy between Contacting Electrospun Fibers. *Langmuir* 2014, **30**(23)**:** 6819-6825.

20. Kluge D, Abraham F, Schmidt S, Schmidt H-W, Fery A. Nanomechanical Properties of Supramolecular Self-Assembled Whiskers Determined by AFM Force Mapping. *Langmuir* 2010, **26**(5)**:** 3020-3023.

21. Kluge D, Singer JC, Neubauer JW, Abraham F, Schmidt HW, Fery A. Influence of the Molecular Structure and Morphology of Self-Assembled 1,3,5-Benzenetrisamide Nanofibers on their Mechanical Properties. *Small* 2012, **8**(16)**:** 2563-2570.

22. Misslitz H, Kreger K, Schmidt HW. Supramolecular Nanofiber Webs in Nonwoven Scaffolds as Potential Filter Media. *Small* 2013, **9**(12)**:** 2053-2058.

23. Singer JC, Giesa R, Schmidt H-W. Shaping self-assembling small molecules into fibres by melt electrospinning. *Soft Matter* 2012.

24. Greiner A, Wendorff JH. Electrospinning: A fascinating method for the preparation of ultrathin fibers. *Angew Chem-Int Edit* 2007, **46**(30)**:** 5670-5703.

25. Agarwal S, Greiner A, Wendorff JH. Functional materials by electrospinning of polymers. *Prog Polym Sci* 2013, **38**(6)**:** 963-991.

26. Singer JC, Ringk A, Giesa R, Schmidt H-W. Melt Electrospinning of Small Molecules. *Macromolecular Materials and Engineering* 2015, **300**(3)**:** 259-276.

27. Kluge D, Singer JC, Neugirg BR, Neubauer JW, Schmidt HW, Fery A. Top-down meets bottom-up: A comparison of the mechanical properties of melt electrospun and self-assembled 1,3,5-benzenetrisamide fibers. *Polymer* 2012, **53**(25)**:** 5754-5759.

28. Singer JC, Giesa R, Schmidt H-W. Shaping self-assembling small molecules into fibres by melt electrospinning. *Soft Matter* 2012, **8**(39)**:** 9972-9976.

29. Pericet-Camara R, Papastavrou G, Behrens SH, Borkovec M. Interaction between charged surfaces on the Poisson-Boltzmann level: The constant regulation approximation. *Journal of Physical Chemistry B* 2004, **108**(50)**:** 19467-19475.

30. Tomatsu I, Fitie CFC, Byelov D, de Jeu WH, Magusin P, Wubbenhorst M*, et al.* Thermotropic Phase Behavior of Trialkyl Cyclohexanetriamides. *Journal of Physical Chemistry B* 2009, **113**(43)**:** 14158-14164.

31. Timme A, Kress R, Albuquerque RQ, Schmidt HW. Phase Behavior and Mesophase Structures of 1,3,5-Benzene- and 1,3,5-Cyclohexanetricarboxamides: Towards an Understanding of the Losing Order at the Transition into the Isotropic Phase. *Chem-Eur J* 2012, **18**(27)**:** 8329-8339.

32. Hutter JL, Bechhoefer J. Calibration of atomic-force microscope tips. *Rev Sci Instrum* 1993, **64**(7)**:** 1868-1873.

33. Sader JE, Larson I, Mulvaney P, White LR. Method for the calibration of atomic-force microscope cantilevers. *Rev Sci Instrum* 1995, **66**(7)**:** 3789-3798.

34. Barten D, Kleijn JM, Duval J, Lyklema J, Cohen Stuart MA. Double Layer of a Gold Electrode Probed by AFM Force Measurements. *Langmuir* 2003, **19**(4)**:** 1133-1139.

35. Rentsch S, Pericet-Camara R, Papastavrou G, Borkovec M. Probing the validity of the Derjaguin approximation for heterogeneous colloidal particles. *Phys Chem Chem Phys* 2006, **8**(21)**:** 2531-2538.

36. Valtiner M, Banquy X, Kristiansen K, Greene GW, Israelachvili JN. The Electrochemical Surface Forces Apparatus: The Effect of Surface Roughness, Electrostatic Surface Potentials, and Anodic Oxide Growth on Interaction Forces, and Friction between Dissimilar Surfaces in Aqueous Solutions. *Langmuir* 2012, **28**(36)**:** 13080-13093.

37. Kirwan LJ, Maroni P, Behrens SH, Papastavrou G, Borkovec M. Interaction and Structure of Surfaces Coated by Poly(vinyl amines) of Different Line Charge Densities. *The Journal of Physical Chemistry B* 2008, **112**(46)**:** 14609-14619.

38. Kuznetsov V, Papastavrou G. Ion Adsorption on Modified Electrodes as Determined by Direct Force Measurements under Potentiostatic Control. *J Phys Chem C* 2014, **118**(5)**:** 2673-2685.

39. Gu Y. The Electrical Double-Layer Interaction between a Spherical Particle and a Cylinder. *J Colloid Interface Sci* 2000, **231**(1)**:** 199-203.

40. Li K, Chen Y. Evaluation of DLVO interaction between a sphere and a cylinder. *Colloids and Surfaces A: Physicochemical and Engineering Aspects* 2012, **415:** 218-229.

41. Montgomery SW, Franchek MA, Goldschmidt VW. Analytical Dispersion Force Calculations for Nontraditional Geometries. *J Colloid Interface Sci* 2000, **227**(2)**:** 567-584.

42. Zimmermann R, Freudenberg U, Schweiß R, Küttner D, Werner C. Hydroxide and hydronium ion adsorption — A survey. *Current Opinion in Colloid & Interface Science* 2010, **15**(3)**:** 196-202.

43. Maroni P, Montes Ruiz-Cabello FJ, Tiraferri A. Studying the role of surface chemistry on polyelectrolyte adsorption using gold-thiol self-assembled monolayer with optical reflectivity. *Soft Matter* 2014, **10**(46)**:** 9220-9225.

44. Drechsler A, Petong N, Zhang JF, Kwok DY, Grundke K. Force measurements between Teflon AF and colloidal silica particles in electrolyte solutions. *Colloid Surf A-Physicochem Eng Asp* 2004, **250**(1-3)**:** 357-366.

45. Kudin KN, Car R. Why Are Water−Hydrophobic Interfaces Charged? *J Am Chem Soc* 2008, **130**(12)**:** 3915-3919.

46. Rentsch S, Siegenthaler H, Papastavrou G. Diffuse Layer Properties of Thiol-Modified Gold Electrodes Probed by Direct Force Measurements. *Langmuir* 2007, **23**(17)**:** 9083-9091.

47. Zimmermann R, Dukhin S, Werner C. Electrokinetic Measurements Reveal Interfacial Charge at Polymer Films Caused by Simple Electrolyte Ions. *The Journal of Physical Chemistry B* 2001, **105**(36)**:** 8544-8549.

48. Lutzenkirchen J, Preocanin T, Kallay N. A macroscopic water structure based model for describing charging phenomena at inert hydrophobic surfaces in aqueous electrolyte solutions. *Phys Chem Chem Phys* 2008, **10**(32)**:** 4946-4955.

49. Helfricht N, Klug M, Mark A, Kuznetsov V, Blum C, Scheibel T*, et al.* Surface properties of spider silk particles in solution. *Biomaterials Science* 2013, **1**(11)**:** 1166-1171.

Perspectives

To outline future perspectives of comprehensive AFM-based fiber characterization, it is illustrative to stick to the picture from Figure 2 where advanced AFM techniques nurture the ground for flourishing knowledge about fiber systems. The principal opportunities in the field (and according to the picture) are on the one hand to transfer the demonstrated approaches to other fiber systems (i.e. to grow more flowers); and on the other hand, the advancement of the techniques themselves as an exciting methodical route to pursue (which further cultivates the ground).

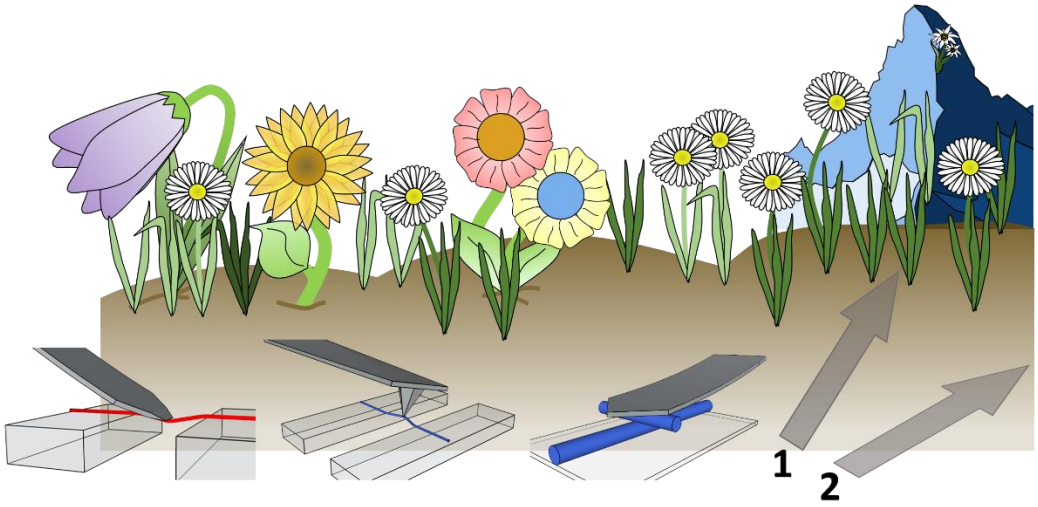

Figure 32| Illustration of perspective future advances in the field of AFM-based (nano-)fiber characterization. The generic nature of the methods presented in this thesis allows for characterizing almost every fiber system (route 1). The AFM is a versatile tool that experiences continued further developments hence facilitating exiting methodical advances (route 2) for improved and extended fiber characterization.

Concerning the first route, arguably one of the biggest advantages of all approaches presented here is that they are truly generic. The diverse spectrum of materials investigated in this thesis (polymer, protein, small organic molecules/supramolecular structures) already demonstrates this high adaptability. Yet beyond those materials, the literature gives many examples where similar techniques have been applied to other fiber systems (see II.3 for mechanical testing and III.4 for

interaction measurements). As there is continued and increasing interest in the development of fiber-based materials exploiting their electronical, mechanical or biological properties, the characterization of their fundamental building components - the individual (nano-)fibers - will stay a major focus in those fields of research and industry. The ongoing expansion of the material library and fiber spinning techniques will continuously demand for detailed characterizations of new fibrillar compounds. The AFM-based platform for probing the fibers' deformations and interactions is hence an attractive cornerstone in rational material and morphology design.

Beyond simple testing of (nano-)fibers from different materials, the AFM-based setup is highly variable and allows for further methodical development with respect to the specific questions at hand (route 2). Regarding interaction measurements, filtration or flow-through processes could be investigated on a fundamental level. Particle interactions with filters and particle specific filtration, reversible (stimuli-responsive) adhesion, or fiber cohesion (e.g. in a nonwoven) could be studied directly and on a single interaction-pair level. Considering the field of tissue engineering, the interactions of cells with different (fibrillar) substrates are of central importance and could be studied attaching either cell or fiber to a cantilever. Another step could involve fluid force microscopy,[1] where measurements with cells are possible on the one hand but on the other hand also small, nanoscale fibers and particles could be attached to a cantilever reversibly. This would, for instance, facilitate direct interaction measurements of nanoscopic fibers.

Furthermore, the AFM is a tool that is capable of combining mechanical or interaction measurements with the investigation of other observables or in dependence of environmental conditions. In the past, electrical measurements have been performed during mechanical deformations,[2-4] or the influence of environmental conditions (temperature, surrounding medium) on collagen,[5, 6] polymers[7] or hair[8] has been studied. In that regard, especially the spider silk system is not yet understood and questions for e.g. the origin of supercontraction remain to be answered conclusively. Advances in AFM as the development of fast and dynamic mechanical analysis (e.g. peak force QNM[9]) furthermore open up opportunities for future studies. For instance, the velocity of changes in the respective material in response to a stimulus could be considered.

In conclusion, AFM-based (nano-)fiber characterization will continue to provide unique insights into the fundamental mechanical and interaction mechanisms of almost arbitrary fibrillary systems. The variability of the presented approaches renders them a valuable tool to unravel even complex, stimuli-triggered behavior.

References

1. Nanosurf. FluidFM - A unique new tool for single cell biology and beyon. 2013 [cited 2016 12.09.2016]Available from: https://www.nanosurf.com/downloads/fluidfm-brochure.pdf

2. Tombler TW, Zhou CW, Alexseyev L, Kong J, Dai HJ, Lei L*, et al.* Reversible electromechanical characteristics of carbon nanotubes under local-probe manipulation. *Nature* 2000, **405**(6788)**:** 769-772.

3. Minot ED, Yaish Y, Sazonova V, Park JY, Brink M, McEuen PL. Tuning carbon nanotube band gaps with strain. *Phys Rev Lett* 2003, **90**(15)**:** 156401.

4. McCarthy EK, Bellew AT, Sader JE, Boland JJ. Poisson's ratio of individual metal nanowires. *Nat Commun* 2014, **5:** 4336.

5. Yang L, Van der Werf KO, Fitie CFC, Bennink ML, Dijkstra PJ, Feijen J. Mechanical properties of native and cross-linked type I collagen fibrils. *Biophys J* 2008, **94**(6)**:** 2204-2211.

6. Yang L, Fitié CFC, van der Werf KO, Bennink ML, Dijkstra PJ, Feijen J. Mechanical properties of single electrospun collagen type I fibers. *Biomaterials* 2008, **29**(8)**:** 955-962.

7. Wang W, Barber AH. Measurement of size-dependent glass transition temperature in electrospun polymer fibers using AFM nanomechanical testing. *J Polym Sci Pt B-Polym Phys* 2012, **50**(8)**:** 546-551.

8. Max E, Hafner W, Bartels FW, Sugiharto A, Wood C, Fery A. A novel AFM based method for force measurements between individual hair strands. *Ultramicroscopy* 2010, **110**(4)**:** 320-324.

9. Bruker. Quantitative Mechanical Property Mapping at the Nanoscale with Peak Force QNM. 2012.

Danksagung

An diesem Punkt, an dem der Ernst des Lebens etwas ernster wird und der heimelig-grüne Bayreuther Campus einen alten Hasen ausspuckt, nur um ihn – mit etwas grün hinter den Ohren - wieder zum Frischling werden zu lassen, ist es höchste Zeit „Danke“ zu sagen.

Danke, Prof. Andreas Fery! Danke für ein nahrhaftes Gehege in dem ich niemals die Gitter gespürt habe und immer mehr mit Zuckerbrot als mit Peitsche zu all dem getrieben wurde, was in dieser Arbeit steht. Es ist nicht selbstverständlich, einen Chef zu haben, für den man gerne arbeitet und bei dem man spürt, dass auch er für einen arbeitet. Vielen Dank für diese Erfahrung!

Danke, Prof. Georg Papastavrou, Prof. Hans-Werner Schmidt, Prof. Andreas Greiner und Prof. Thomas Scheibel! Danke für die Möglichkeit, facettenreiche Einblicke in Ihre Wissenschaft erhalten zu haben und diese Wissenschaft ein µ weit mitgestalten zu dürfen.

Danke, Daniel Kluge, Gregor Lang, Nicolas Helfricht, Matthias Burgard, Klaus Kreger, Sean Koebley und Prof. Hannes Schniepp! Danke für Zusammenarbeit, die nicht nur auf dem Papier bestand, sondern deren Früchte auch digital verfügbar sind.

Danke, Inna Dewald, Maximilian Seuss und Johann Erath. Danke für das Korrekturlesen meiner geistigen Ergüsse.

Danke, PCII, egal ob in Bayreuth oder in Dresden!

Danke, Stammtisch, Kameraden und Schuljungen! Die viele Freizeit während der Promotion macht nur genutzt Spaß!

Danke, liebe Familie! Danke für die Couch, die immer frei und nicht nur ein Möbelstück ist!

Danke, liebste Nicky! Danke für Nähe in der Ferne, für Höhen ganz oben und für viel Geduld und soliden Blödsinn. :*

Erklärung

Hiermit erkläre ich an Eides statt, dass ich die vorliegende Arbeit selbständig und nur unter Verwendung der angegebenen Quellen und Hilfsmittel angefertigt habe.

Weiterhin erkläre ich, dass ich weder an der Universität Bayreuth noch an einer anderen Universität versucht habe, eine Dissertation einzureichen oder eine Promotionsprüfung abzulegen.

Ich erkläre, dass ich zu keinem Zeitpunkt die Hilfe eines gewerblichen Promotionsberaters oder -vermittlers in Anspruch genommen habe und dies auch in Zukunft nicht tun werde.

Schließlich erkläre ich mein Einverständnis, dass die elektronische Fassung der Dissertation unter Wahrung meiner Urheberrechte und des Datenschutzes einer gesonderten Überprüfung hinsichtlich der eigenständigen Anfertigung der Dissertation unterzogen werden kann.

Bayreuth,

Benedikt Neugirg